

Investigation of dielectric properties of rocks and minerals for GPR data interpretation

by

Sohely Pervin

A thesis submitted in partial fulfillment of the requirements for the degree of

Master of Science

in

Geophysics

Department of Physics  
University of Alberta

© Sohely Pervin, 2015

## **Abstract**

At radar frequencies, the propagation speeds and attenuations of electromagnetic (EM) waves are controlled by the complex dielectric permittivity. Consequently, the real and imaginary components as well as their variation with frequency are important parameters necessary for properly interpreting Ground Penetrating Radar (GPR) data. Such data is used to detect objects or to infer the geological structure, and it does this primarily by interpreting the times and amplitudes of radar reflections in the soils and rocks near the earth's surface. This study is motivated by the use of GPR to map weak and unsafe layers in underground potash mines in Saskatchewan. Consequently, knowledge of dielectric permittivity of the evaporate minerals and their contaminants is necessary to interpret GPR data more effectively particularly with regards to mine safety. In this study, we measured the dielectric permittivity of a number of minerals associated with the potash deposits over a frequency range of 10 MHz to 3 GHz using a commercially available material analyzer. Measurements were carried out on both synthetic and real samples. A cold compression technique in which mixed mineral powders were subject to pressures as high as 300 MPa was used to prepare the samples. The results of these measurements were then applied to predict the strength of GPR reflections that might be encountered in a real situation.

*Dedicated To My Parents*

## **Acknowledgements**

At first I would like to thank my supervisor Dr. Douglas R. Schmitt. Without his help this it was not possible to complete writing up this thesis. He guided me as a mentor starting the research works I have done in the lab to writing up the thesis. I would also like to thank Randolph Koffman who works as a research professional in the rock physics lab at the U of A. He helped me a lot during all the experimental measurements I have done.

I must also thank greatly Dr. Sanaa Aqil who carried out postdoctoral research with Dr. Schmitt. She was primarily responsible for setting up the dielectric permittivity recording system and for developing initially the cold compression technique. My work would have been impossible without her input.

I would also thank my husband Md. Nasir Uddin who was always beside me in different difficult situation and encourage to recover that. A very special thanks to my parents and my family for their kind support, love, sacrifice and guidance.

All the devotion and admiration to Almighty who has enabled me to complete this thesis in time.

## Table of Contents

CHAPTER 1.	INTRODUCTION .....	22
1.1	Background .....	22
1.2	Motivation .....	26
1.3	Chapter Description.....	27
CHAPTER 2.	BACKGROUND .....	29
2.1	Introduction.....	29
2.2	Dielectric Materials .....	29
2.3	Maxwell's Equations .....	32
2.4	Electromagnetic Wave propagation .....	34
2.5	Electromagnetic Wave propagation .....	35
2.5.1	Magnetic Permeability .....	35
2.5.2	Electrical conductivity .....	37
2.5.3	Dielectric permittivity .....	37
2.6	Dielectric Measurement Techniques .....	41
2.6.1	Time domain methods.....	41
2.6.2	Standing wave methods .....	42
2.6.3	Frequency Domain Methods.....	42
2.6.4	Impedance Methods .....	43

2.6.5	Current-Voltage IV methods.....	43
2.7	Dispersion.....	46
2.7.1	Orientation or Dipolar polarization.....	47
2.7.2	Electronic and atomic polarization .....	49
2.7.3	Ionic Polarization .....	50
2.7.4	Response of Different Polarization to Applied Field Frequency.....	50
2.7.5	Interfacial or space charge polarization .....	51
2.8	Dielectric Relaxation.....	52
2.9	Debye Relation .....	53
2.10	Cole-Cole Diagram .....	55
2.11	Debye and Cole-Cole diagrams for water from experiments.....	56
2.12	Mixing Theories .....	59
2.13	Conclusions .....	67
CHAPTER 3.	METHODOLOGY .....	68
3.1	Measurement System .....	68
3.2	RF I-V Technique.....	70
3.2.1	Calibration.....	73
3.2.2	Advantages and Limitations of the RF IV Method.....	76
3.3	Cold Compression Technique .....	76
3.3.1	Advantages and Limitations of the Cold Compression Technique .....	79

3.4	Material Characterization .....	79
3.4.1	Scanning Electron Microscope (SEM) .....	80
3.4.2	Helium Pycnometer .....	81
3.4.3	Mercury Porosimeter .....	82
3.4.4	X-ray Diffraction (XRD) .....	84
3.4.5	X-ray Fluorescence (XRF) Elemental Analysis .....	84
3.5	Summary .....	85
CHAPTER 4.	MEASUREMENTS ON MINERALS AND SYNTHETIC SAMPLES .....	86
4.1	Introduction .....	86
4.2	Single Crystal Measurements .....	86
4.3	Measurement on cold compressed halite and sylvite samples .....	91
4.4	Salt With Glass Beads .....	95
4.5	Mixing Model .....	98
4.5.1	Inclusion of lower permittivity than the matrix .....	98
4.5.2	Inclusion of higher permittivity than the matrix .....	102
4.5.3	Inclusion of permittivity comparable to the matrix .....	105
4.5.4	Comparison of porous salts with theory .....	106
4.6	Summary .....	113
CHAPTER 5.	APPLICATION TO ROCK CORES .....	114
5.1	Introduction .....	114

5.2	Background .....	114
5.2.1	Geology and Geophysical Logs at Rocanville.....	117
5.3	Core Materials Studied.....	118
5.3.1	Heterogeneity in a single sample .....	119
5.3.2	Variations with depth.....	127
5.3.3	Sample 1: Depth (1216.65-1217.27) meter.....	131
5.3.4	Sample 2: Depth (1223.67-1224.30) meter.....	133
5.3.5	Sample 3: Depth (1230.28-1230.49) meter.....	134
5.3.6	Sample 4: Depth (1246.25-1247.00) meter.....	135
5.3.7	Sample 5: Depth (1255.63-1256.31) meter.....	138
5.3.8	Sample 6: Depth (1266.34-1266.71) meter.....	140
5.3.9	Sample 7: Depth (1271.86-1272.49) meter.....	142
5.3.10	Sample 8: Depth (1284.33 - 1284.89) meter.....	144
5.3.11	Relatively conductive zone (e.g clay or clayey evaporite) .....	146
5.3.12	Brine inclusions effect .....	147
5.4	Reflection modelling.....	148
5.5	Summary .....	153
CHAPTER 6.	CONCLUSION .....	154
6.1	Summary of Work Completed .....	154
6.2	Recommendation for Future Work .....	156



<b>References</b> .....	158
Appendix A .....	171
Appendix B .....	185

## List of Figures

Figure 2-1 Parallel plate capacitor using DC circuit.....	30
Figure 2-2 Parallel plate capacitor using AC circuit.....	31
Figure 2-3 Reflected and transmitted signals for transverse electromagnetic wave (TEM).....	35
Figure 2-4 Loss tangent vector diagram. ....	38
Figure 2-5 Essential components of an IV measurement system that includes an AC voltage source, a voltmeter to provide $V(t)$ shown in red in right graph and an ammeter to provide $I(t)$ shown in green in right graph. The sample is shown as being mounted in between two parallel plates of capacitor in this example. For a perfect lossless dielectric $dt = 1/4f$ equating to a phase shift angle of $\theta = \pi/2$ . For a lossy case $\theta < \pi/2$ and $dt < 1/4f$ . ....	46
Figure 2-6 Different polarization processes occur at different frequencies causing dielectric dispersion (Ref after (Agilent)).....	47
Figure 2-7 Dipolar rotation in the electric field (Ref after (Agilent)).....	48
Figure 2-8 Electronic polarization of atoms. ....	49
Figure 2-9 Atomic polarization between ions.....	50
Figure 2-10 Change in polarization due to sudden change in applied electric field. ....	53
Figure 2-11 Debye relaxation for water at 30 °C (ref after (Agilent)).....	54
Figure 2-12 Cole-Cole representation of the Debye model of water at 300C. (ref. after (Agilent)). .....	55
Figure 2-13 Debye plots for water from the experimental data.....	57
Figure 2-14 Cole-Cole plot for water from the experimental data (left). Circle fit of the data is also shown (right). ....	58

Figure 3-2 Coaxial probe (left) and a cross section of the sensor. The electric field lines fringe from the end of the sensor into the sample under measurement. ....	70
Figure 3-3 Basic principle of RF I-V technique and vector voltage ratio relationship (ref. after Agilent). ....	71
Figure 3-4 Vector voltage ratio relationship to impedance for E4991A. ....	72
Figure 3-5 Dielectric permittivity of halite and sylvite single crystal to check the accuracy of calibration of the equipment. ....	75
Figure 3-6 Synthetic sample (NaCl and KCl) prepared using cold compressing technique. ....	79
Figure 3-7 Cumulative intrusion versus pressure for a porous NaCl sample (measured porosity 4%) using Hg porosimeter. ....	83
Figure 4-1 Group of single evaporite crystals. A is halite and sylvite, B and C are calcite, D, E, F and G are gypsum and H is dolomite. ....	90
Figure 4-2 The variation of porosity with pressure and the variation of permittivity with porosity of four halite samples (porosity were measured using mercury porosimeter). ....	92
Figure 4-3 Scanning electron micrographs on cold compressed NaCl. a) Original reagent grade NaCl crystals used to make the samples. b) Porous NaCl sample cold compressed at 55 MPa. Porosity indicated by undrained Hg and by open pores as designated by white arrow. ....	93
Figure 4-4 Dielectric permittivity of a) cold compressed KCl and single sylvite (KCl) crystal; b) cold compressed NaCl and single halite (NaCl) crystal. Cold compressed samples showed similar permittivity values as single crystal. ....	94
Figure 4-5 Scanning electron microscopy (SEM) ....	95
Figure 4-6 Scanning Electron microscopy on glass beads mixed with NaCl sample. ....	97

Figure 4-7 Calculated permittivities of the dry porous NaCl as a fraction of air filled pore volume between 0 to 1. Superscripts + and - are upper and lower bounds. ....	101
Figure 4-8 Calculated permittivity of the water saturated NaCl at fraction pore volume between 0 to 1. Permittivities were calculated from nine mixing theories. ....	104
Figure 4-9 Calculated permittivity of Halite-Sylvite mixtures versus fraction volume of sylvite. A comparison of our measurement value with theoretical model .....	106
Figure 4-10 Dielectric permittivity of porous NaCl versus fractional pore volume plots using mixing models and experiments. The black circles with error bars represent experimental values for the eight porous NaCl samples, and the green dashed line is the linear fit. ....	109
Figure 4-11 Dielectric permittivity of porous KCl versus fractional pore volume plots using mixing models and experiments. The black circles with error bars represent the experimental values for the eight porous KCl samples, and the green dashed line is the linear fit. ....	110
Figure 5-1 Potash mining belt (Reproduced with permission from NorthRim) .....	116
Figure 5-2 Resistivity of different depths in Rocanville Potash mine .....	118
Figure 5-3 A piece of core sample in the depth range of 1238.678-1239.37 meter .....	119
Figure 5-4 Real and imaginary permittivity versus frequency for raw potash samples .....	123
Figure 5-5 Real and imaginary permittivity versus frequency for compressed potash samples .....	124
Figure 5-6 (a) represents dielectric values placing each of the 14 pieces of the core directly on the sensor. The core was taken from depth (1238.68-1239.31 meter, (b). represents the dielectric values of 14 (compressed) samples. All the permittivity values were averaged out from four measurements. (c, d) represent the standard deviations (S.D.) of the permittivity in the raw and compressed samples respectively. ....	126
Figure 5-7 Compressed samples at the eight different depths of Rocanville potash mine. ....	128

Figure 5-8 The real and imaginary relative permittivity of samples taken from GPR reflection zone. The samples names stand for the depth it was taken from. ....	129
Figure 5-9 Calculated speed wave for the samples taken from GPR reflection zone. The name of the samples stand for the depth it was taken from. At high clay content the velocity becomes a function of frequency. ....	130
Figure 5-10 Scanning Electron Microscope image of a sample taken from (1216.65 - 1217.27) meter depth. ....	132
Figure 5-11 Scanning Electron Microscope image of a sample taken from (1223.67-1224.30) meter depth. ....	134
Figure 5-12 Scanning Electron Microscope image of a sample taken from (1230.28-1230.49) meter depth. ....	136
Figure 5-13 Scanning Electron Microscope image of a sample taken from (1246.25-1247.00) meter depth. ....	137
Figure 5-14 Scanning Electron Microscope image of a sample taken from (1255.63 - 1256.31) meter depth. ....	139
Figure 5-15 Scanning Electron Microscope image of a sample taken from (1266.34 - 1266.71) meter depth. ....	141
Figure 5-16 Scanning Electron Microscope image of a sample taken from (1271.86 - 1272.49) meter depth. ....	143
Figure 5-17 Scanning Electron Microscope image of a sample taken from (1284.33 - 1284.89) meter depth. ....	145
Figure 5-18 Change of reflection coefficient with frequency. ....	150

Figure 5-20 Synthetic GPR trace after convolution of the above mentioned signal with the ricker wavelet. .... 152

## List of Tables

Table 4-1 Average real dielectric permittivity for single crystal evaporate minerals over 10 MHz to 3 GHz.....	87
Table 4-2 Dielectric permittivity and porosity values for synthetic NaCl samples compressed at different pressure. Porosity values using mercury porosimeter.....	91
Table 4-3 Dielectric permittivity of glass beads mixed with KCl and NaCl according to mass percentage. ....	96
Table 4-4 Dielectric permittivity, porosity, grain volume and bulk volume of NaCl and KCl samples. Both the grain volume and bulk volume were calculated using He pycnometer.....	108
Table 4-5 Relative percentage change between the experimental results and mixing theories for NaCl samples. Variance and standard deviation is also shown. Experimental values are taken as reference.....	111
Table 4-6 Relative percentage change between the experimental results and mixing theories for KCl samples. Variance and standard deviation is also shown. Experimental values are taken as reference.....	112
Table 5-1 Dielectric permittivity of different samples using raw potash measurement and cold compressed technique .....	122
Table 5-2 Dielectric permittivity (real and imaginary) and velocity in different depth ranges. Data reported as mean $\pm$ standard deviation. The measurement frequency was 10 MHz to 3 GHz .....	128
Table 5-3 The mineralogy of a sample taken from the depth range (1216.65 - 1217.27) meter.	131
Table 5-4 The mineralogy of a sample taken from the depth range (1223.67 - 1224.30) meter. ....	133

Table 5-5 The mineralogy of a sample taken from the depth range (1230.28 - 1230.49) meter.	135
Table 5-6 The mineralogy of a sample taken from the depth range (1246.25 - 1247.00) meter.	135
Table 5-7 The mineralogy of a sample taken from the depth range (1255.63 - 1256.31) meter.	138
Table 5-8 The mineralogy of a sample taken from the depth range (1266.34 - 1266.71) meter.	140
Table 5-9 The mineralogy of a sample taken from the depth range (1271.86 - 1272.49) meter.	142
Table 5-10 The mineralogy of a sample taken from the depth range (1284.33 - 1284.89) meter.	144
Table 5-11 Resistivities of GPR reflection zones.	147
Table 5-12 Reflection coefficients and time.	149



## List of Symbols

$\varepsilon$	Dielectric permittivity
$\varepsilon_r$	Relative permittivity
$\varepsilon_0$	Free space permittivity
$\varepsilon'$	Real dielectric permittivity or dielectric storage
$\varepsilon''$	Imaginary dielectric permittivity or dielectric loss
$\varepsilon^*$	Complex dielectric permittivity
$\varepsilon^{eff}$	Relative equivalent dielectric permittivity
$\sigma$	Conductivity
$\sigma^{eff}$	Effective conductivity
$\omega$	Angular frequency
$C$	Capacitance with dielectric material between plates
$C_0$	Capacitance without dielectric material between plates
$A$	Area of the capacitor plates
$d$	Distance between plates
$V$	Voltage
$I_c$	Charging current
$I_l$	Loss current
$G$	Conductance
$f$	Frequency
$D_f$	Electric displacement (electric flux density)
$E$	Electric field
$D$	Electric displacement vector

$H$	Magnetic field intensity
$q$	Electric charge density
$J$	Electric current density vector
$\mu$	Magnetic permeability
$\mu_0$	Magnetic permeability of free space
$\mu_r$	Relative magnetic permeability
$\mu'$	Total induced magnetization
$\mu''$	Magnetic hysteresis loss
$K$	Dielectric constant
$n$	Refractive index
$Z_0$	Intrinsic wave impedance
$c$	Speed of light
$k$	Volume magnetic susceptibility
$\tan\delta$	Ratio of the imaginary part of the dielectric constant to the real part.
$D$	Dissipation factor
$Q$	Quality factor
$v$	Propagation phase velocity of an EM wave in any media
$P$	Power dissipation
$Z$	Intrinsic electromagnetic impedance of a material
$R$	Plane wave reflection co-efficient
$A$	Absorption coefficient
$f_c$	Relaxation frequency
$\tau$	Relaxation time

$f_c$	Relaxation frequency
$\alpha$	Angle between the real axis and the high frequency intercept line
$\varepsilon_1$	Complex dielectric permittivity of the background
$\varepsilon_2$	Complex dielectric permittivity of the inclusions
$f_1$	Fractional volume of the background
$f_2$	Fractional volume of the inclusions
Q	Quality factor
$Z_r$	Roll-off impedance
$P_1$	Initial pressure of the gas
$P_2$	Final pressures of the gas
$V_1$	Initial volume
$V_2$	Final volume
$V_r$	Volume of the reference cell
$V_s$	Volume of the cell containing the sample
$V_g$	Volume of the solid portion of the sample
$\phi$	Porosity
$V_b$	Bulk volume
$D$	Diameter of pore throat
$P$	Applied pressure
$\gamma$	Surface tension of mercury
$\theta$	Contact angle
$KCl$	Sylvite
$NaCl$	Halite

$KMgCl_3 \cdot 6H_2O$  Carnallite

$KAl_2(Si_3Al)O_{10}(OH.F)_2$  Muscovite

$CaMg(CO_3)_2$  Dolomite

$Ca(SO_4)$  Anhydrite

$CaSO \cdot 2H_2O$  Gypsum

$CaCO_3$  Calcite

## List of Acronyms

GPR	Ground Penetrating Radar
EM	Electromagnetic
TDR	Time domain reflectometry
MPa	Mega Pascal
SEM	Scanning Electron Microscopy
XRD	X-Ray diffraction
XRF	X-Ray fluorescence
DC	Direct current
AC	Alternating current
TEM	Transverse electromagnetic
FDR	Frequency domain reflectometry
RF-IV	Radiofrequency - Current Voltage
BHS	Bruggeman-Hanai-Sen
CRIM	Complex refractive index mixture
LLL	Landau, Lifshitz, Looyenga
HS <sup>+</sup>	Hashin-Strickmann upper limit
HS <sup>-</sup>	Hashin-Strickmann lower limit
SNR	Signal-to-noise ratio
IR	Infrared
PCS	Potash Corp. of Saskatchewan

# CHAPTER 1. INTRODUCTION

This work is mainly focused on the dielectric property measurements of geological materials from potash mines in Saskatchewan. It is motivated to support the interpretation of Ground Penetrating Radar (GPR) surveys conducted in the potash mines. In this first chapter, we simply explain the motivations for the work and provide a brief outline of the contents of the following chapters.

## 1.1 Background

Dielectric permittivity ( $\epsilon$ ) is an important physical property that is widely used in various realms of science including geophysics, condensed matter physics, biology, forestry, agriculture, engineering and hydrology [Topp *et al.*, 1980]. One of the most important uses of dielectric constant is to quantify water content [Josh *et al.*, 2012]. Measurements of  $\epsilon$  are used as a proxy for water content in soils through empirical relationships [e.g., Malicki *et al.*, 1996; Roth *et al.*, 1992; Topp *et al.*, 1980]. Further, using GPR the structure of the near surface of the Earth may be imaged at radio frequencies ( $\sim 10$  MHz to 1.5 GHz). Water is highly influential on such wave propagation over this frequency range because its relative dielectric permittivity is nearly 80 while that of the minerals forming the rocks ranges from about 3 to 9 and for air for all practical purposes can be taken to be 1 [Weast, 1984]. As such, even small amounts of water within the pore space of a rock can strongly influence the propagation of GPR signals.

Both invasive (time domain reflectometry and cross borehole radar) and non-invasive (ground penetrating radar) electromagnetic techniques are used to estimate water content and porosity [Sakaki *et al.*, 1998; Sen *et al.*, 1981]. This is because the propagation speed of

electromagnetic (EM) radiation through such materials is governed by the bulk or effective dielectric permittivity that depends strongly on water content. Therefore the knowledge of dielectric permittivity is crucial to the accurate interpretation of GPR images. The soil science literature mostly focuses on moisture estimation primarily using time domain reflectometry techniques (TDR); the literature associated with this topic large and relatively mature [Robinson *et al.*, 2003]. In contrast, studies of the relationships between GPR wave propagation and the material physical properties are not as advanced. This is likely due to the broader range of geological topics encountered in GPR studies. As well, actually obtaining reliable values of  $\epsilon$  applicable to lower porosity materials that do not necessarily contain water is difficult.

Non-destructive GPR or geo-radar has wide application in hydrology, sedimentology, geological structure, fractures, glaciers and land mine detection. Moreover, it is a popular technique for imaging the subsurface and is particularly useful in electrically resistive materials such as clean sands, crystalline igneous and metamorphic rock, salt deposits, concrete, and ice [Daniels *et al.*, 1988]. Despite this, a lack of understanding of physical basis may result in the unsuccessful interpretation of GPR data. Different earth materials have different dielectric permittivities, wave speeds, and attenuations which lead to a reflection of the EM waves at the interfaces between these materials. Finding out the reasons causing reflection on GPR image helps us to interpret GPR data more precisely.

The overriding motivation for this work was the need to better understand GPR observations within potash formations in Saskatchewan. Potash is primarily used as an agricultural fertilizer. Potash ore is mainly composed of sylvite ( $KCl$ ) which is an important industrial chemical. The richest sylvite bearing potash contains substantial proportions of other evaporate minerals particularly halite ( $NaCl$ ) and some carnallite ( $KMgCl_3 \cdot 6H_2O$ ). Moreover,

formations adjacent to the best ores contain a wide variety of additional evaporates such as anhydrite, gypsum, calcite, and dolomite depending upon the depositional and burial history.

GPR has been widely used in salt and potash formations [*Annan et al.*, 1988; *Chiba et al.*, 2006; *Gorham et al.*, 2002; *Holser et al.*, 1972; *Igel et al.*, 2006; *Kulenkampff and Yaramanci*, 1993; *Thierbac*, 1974; *Unterberger*, 1978] to provide detailed structural information that helps the development of underground workings for mining, hazardous waste storage, and scientific studies. Moreover GPR is employed in a nearly real time basis to assist the steering of large mining machines. Indeed, excavator operators in potash mines direct their machines by monitoring their position within the ore zone on the basis of known reflections.

In the Saskatchewan potash mines, high quality ore zones are often bounded by thin ‘shale’ layers that are principally contaminated with anhydrite and calcite. The proximity of the actual mine workings to such ‘shales’ is quite important must be considered during mining as these layers act as weak zones that can easily part and cause roof failures. A photograph of such a weak ‘shale’ layer is shown in Fig. 1-1.

Ground penetrating radars (GPR) attached to mining machines are often used to track these shale layers so that the mine works will stay sufficiently away from them. As such, in order to best interpret the underground observations it is important to understand the reflections seen; but to do this fully requires appropriate knowledge of the physical properties of the constituent evaporate minerals.





**Figure 1-1 Different layers in a Potash mine. The grey colored layers are showing the presence of shale.**

Unfortunately, with regards to the evaporite minerals predominant in the potash mines there is still a paucity of measurements. Further, few of the existing compilations provide information on the dispersion of  $\varepsilon$  with frequency. Consequently, the work in this thesis is motivated by the need to better understand GPR images in underground potash mines in support of underground operations. A novel aspect of this study is the measurement of  $\varepsilon$  on samples that are specially prepared by cold pressing of powders at pressures up to 300 MPa. The values measured on these polycrystalline samples are compared to those on high quality single crystals, with the intention to prove that this method can be applied to more complex mixtures in the future.

## 1.2 Motivation

The over-riding motivation for this work is to obtain better information on the dielectric properties of potash ore and the surrounding geological formations. These results will serve the critical needs related to the safety of underground potash mines. As well, the work may have spin-off benefits for the characterization of such potash ores.

Leading from this motivation, the main objectives of this thesis focus on technical issues that will assist in helping to better understand field GPR observations in potash mines. This entails the following questions we seek to address:

- What are the dielectric properties of the geological materials associated with potash mining?
- How can we make measurements of such materials?
- Can these observed material properties be described theoretically?
- How can we apply these results with a particular focus on understanding the reflectivity of radar frequency waves in such geological formations?

## 1.3 Chapter Description

In this thesis I present dielectric measurements on rock minerals from the potash mines. Dielectric measurements were done on single crystals, on cold-compressed synthetic samples of the minerals associated with the potash deposits, and on natural and cold compressed potash samples. This thesis has been organized into 6 chapters. In this chapter 1, the importance of dielectric measurements and the motivation of this work were briefly discussed.

In chapter 2, I review the related theoretical background. This chapter provides descriptions of dielectrics, Electromagnetic Wave (EM) propagation, and the techniques used to measure dielectric properties. This chapter concludes with a review of the various effective medium mixing theories that can be applied to predict the bulk dielectric properties given the relative proportions of the chemical constituents.

Chapter 3 provides a detailed overview of the experimental set up and the laboratory procedures that I used for the measurements. A key part of this chapter focuses on issues related to sample preparation; and the strategy of cold-compressing pellets of fine powders under high pressures is described. The concluding sections of this chapter describe the different techniques utilized to properly characterize the samples. Chapter 4 includes the results of the dielectric measurements on high quality single crystals, followed by those on the various cold compressed synthetic samples. This chapter concludes with a comparison of the observations to the mixing theory models.

Chapter 5 is mainly focused on the measurements samples taken from an actual potash core. The chapter begins with a brief review of the geology of the region. Dielectric measurements on cold-compressed samples taken from various depths along the core are then described. These samples were carefully characterized using Scanning Electron Microscopy

(SEM) to understand the material structure, X-Ray diffraction (XRD) to know the mineralogical constituents, and X-Ray fluorescence (XRF) to gain some understanding of the overall chemical composition and mineralogy. Finally, these laboratory measurements were then employed to create a synthetic GPR traces.

The concluding Chapter 6 reviews the results of the measurements and judges the quality of the sample preparation methodologies. This chapter ends with a discussion of directions for future work. Moreover, appendix A contains Cole-Cole plots for different samples and appendix B reports MATLAB codes for mixing theories and reflection modeling.

## CHAPTER 2. BACKGROUND

### 2.1 Introduction

Having a clear idea about the physics of electromagnetic wave (EM) propagation is necessary for the proper interpretation of ground penetrating radar (GPR) data. Such data includes information on both the speeds of wave propagation as well as the relative differences (through the strength of GPR reflections) of the dielectric properties between different layers. In this Chapter, I discuss basic electromagnetic wave propagation theory. This is followed by a review of effective medium mixing theory that may be used to help interpret the observations.

### 2.2 Dielectric Materials

Most earth materials are considered to be dielectrics. A material is generally considered to be a dielectric if it satisfies the condition  $\frac{\sigma}{\omega\epsilon} < 0.01$ , where  $\sigma$  is electrical conductivity (Siemens/m),  $\omega$  is angular frequency (rads/s), and  $\epsilon$  is the dielectric permittivity (F/m) [Baker *et al.*, 2007]. If material stores energy in presence of an external electric field the material is called as dielectric and the storage capacity of that material is named as dielectric permittivity.

Most readers will have seen dielectrics introduced in basic Physics discussions of the parallel plate capacitor. If a charge is applied to two parallel plates the resulting device is known as parallel plate capacitor. Fig. 2-1 shows the arrangement where a DC voltage is placed across a parallel plate capacitor inducing positive and negative charges on the two plates. If a dielectric material is placed between the plates, the capacitor can store more charge than if there is no material (a vacuum). The capacitance of the parallel plate capacitor is enhanced due to the

insertion of the dielectric materials. Moreover, an electric field opposing the field of the charged plates is produced which results the reduction of the effective electric field. The capacitance of the parallel plate capacitor is inversely related to the electric field between the plates.

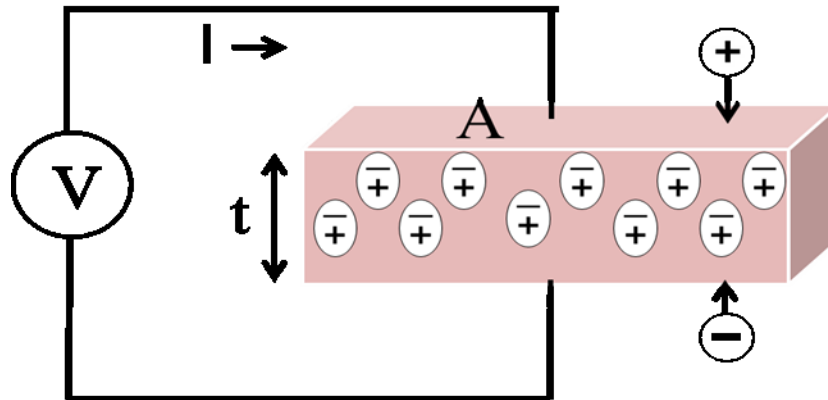


**Figure 2-1 Parallel plate capacitor using DC circuit**

From Fig. 2-1, we can write

$$C_0 = \frac{A}{d} \quad \text{Eq. ( 2-1)}$$

$$C = C_0 \kappa' \quad \text{Eq. ( 2-2)}$$

$$\kappa' = \epsilon' = \frac{C_0}{C} \quad \text{Eq. ( 2-3)}$$

In Eq. (2-1 to 2-3),  $C$  and  $C_0$  are the capacitance with and without dielectric,  $\kappa' = \epsilon'$  represents the real dielectric permittivity or sometimes dielectric constant (when imaginary part of permittivity is very low compared to real part),  $A$  is the area of the capacitor plates and  $d$  is the distance between them. From Eq. (2-3), we can find that the capacitance of a dielectric material is related to the dielectric constant.

Fig. 2-2 shows parallel plate capacitor arrangement in an alternating current (AC) case where an AC sinusoidal voltage source  $V$  is placed across the capacitor. The resulting current in

this case will be made up of two type of current, one of them are charging current ( $I_c$ ) and the other one is loss current ( $I_l$ ). Both the currents are related to the dielectric constant which can be expressed as follows:

$$I = I_c + I_l = V(j\omega C_0 \kappa' + G) \quad \text{Eq. ( 2-4)}$$

where  $G = 1/R$

If  $G = \omega C_0 \kappa''$  then

$$I = V(j\omega C_0)(\kappa' - j\kappa'') = V(j\omega C_0)\kappa \quad \text{Eq. ( 2-5)}$$

Where,  $\omega = 2\pi f$ ,  $R$  = resistance and  $G$  is conductance of the parallel plate capacitor which indicates the losses in the material.

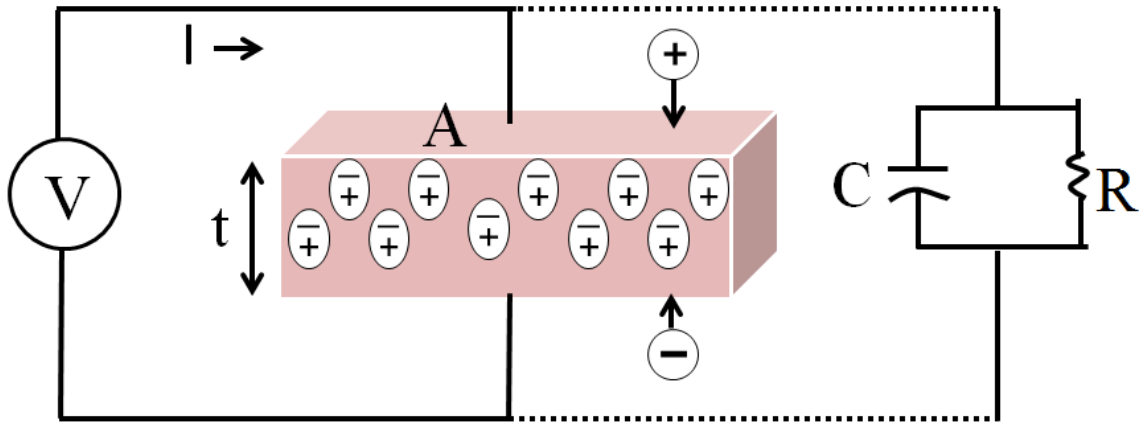


**Figure 2-2 Parallel plate capacitor using AC circuit**

The complex dielectric constant  $K$  consists of a real part  $K'$  which represents the storage and an imaginary part  $K''$  which represents the loss. The following notations are used for the complex dielectric constant interchangeably

$$K = K^* = \varepsilon = \varepsilon' \quad \text{Eq. ( 2-6)}$$

According to electromagnetic theory, the electric displacement (electric flux density)  $D_f$  is described by the following equation

$$\mathbf{D}_f = \varepsilon \mathbf{E} \quad \text{Eq. ( 2-7)}$$

where  $\varepsilon = \varepsilon^* = \varepsilon_0 \varepsilon_r$  is the absolute permittivity (or permittivity),

Here  $\varepsilon_r$  represents the relative permittivity,  $\varepsilon_0 = \frac{1}{36\pi} \times 10^{-9}$  F/m is the free space permittivity and  $\mathbf{E}$  is the electric field.

## 2.3 Maxwell's Equations

Better understanding of GPR behavior depends on the understanding of Maxwell's equations as they describe the relationship between material electromagnetic properties and EM wave propagation as follows:

$$\nabla \times \mathbf{E} = -\frac{\partial \mathbf{B}}{\partial t} \quad \text{Eq. ( 2-8a)}$$

$$\nabla \times \mathbf{H} = \mathbf{J} + \frac{\partial \mathbf{D}}{\partial t} \quad \text{Eq. (2.8b)}$$

$$\nabla \cdot \mathbf{D} = \rho \quad \text{Eq. (2.8c)}$$

$$\nabla \cdot \mathbf{B} = 0 \quad \text{Eq. (2.8d)}$$

where  $\mathbf{E}$  is the electric field strength vector,  $\mathbf{B}$  is the magnetic flux density vector,  $\mathbf{D}$  is the electric displacement vector,  $\mathbf{H}$  is the magnetic field intensity,  $\rho$  is the electric charge density, and  $\mathbf{J}$  is the electric current density vector. A good reference to understand the different notations can be found in Schey [*Schey and Schey*, 2005].

From Maxwell's equations we know electric currents generate magnetic fields and vice versa. In order to understand GPR wave propagation (as discussed later in the EM wave



Propagation section), it is imperative that the electric and magnetic physical properties are understood.

GPR wave propagation primarily depends on the relative permittivity ( $\epsilon_r$ ), the magnetic permeability ( $\mu$ ), and the electrical conductivity ( $\sigma$ ). The relationship between relative permittivity and magnetic permeability to the dielectric constant and refractive index are as follows [Griffiths, 2012].

$$K = \epsilon_r \quad \text{Eq. ( 2-9)}$$

$$n = \sqrt{\frac{\epsilon\mu}{\epsilon_0\mu_0}} = \sqrt{\epsilon_r\mu_r} \quad \text{Eq. ( 2-10)}$$

where:

$K$  =dielectric constant which is dimensionless

$n$  = refractive index which is dimensionless

$\epsilon$  = permittivity (Farads per meter, F/m)

$\epsilon_0$  = permittivity of free space ( $8.854 \times 10^{-12}$  F/m)

$\epsilon_r$  = relative permittivity (dimensionless)

$\mu$  = magnetic permeability (henries per meter, H/m)

$\mu_0$  = magnetic permeability of free space ( $4\pi \times 10^{-7}$  H/m)

$\mu_r$  = relative magnetic permeability , dimensionless.

Now we will discuss about the important parameters and their importance in electromagnetic wave propagation or GPR wave propagation.

## 2.4 Electromagnetic Wave propagation

It is essential to know the basics of electromagnetic (EM) wave propagation through materials. Both electric and magnetic field appear together in a time-varying case is sinusoidal in nature. This EM wave can propagate through free space at the speed of light or through materials at slower speed.

A transverse electromagnetic wave (TEM) travels in free space consists of alternating and in phase vector electric  $\mathbf{E}$  (V/m) and magnetic  $\mathbf{H}$  (A/m) fields that are both perpendicular to each other and to the propagation direction. The wave moves at the speed of light  $c = 299792458$  m/s [Mohr *et al.*, 2008] in vacuum. The ratio of the magnitudes  $\frac{|E|}{|H|}$  has real value equal to the intrinsic wave impedance  $Z_0$  (in  $\Omega$ ).

$$Z_0 = \frac{|E|}{|H|} = c\mu_0 = \sqrt{\frac{\mu_0}{\epsilon_0}} \quad \text{Eq. ( 2-11)}$$

where  $\epsilon_0$  ( $8.854\ 187\ 817 \times 10^{-12}$  Farad  $\text{m}^{-1}$ ) and  $\mu_0$  ( $4\pi \times 10^{-7}$  Henry  $\text{m}^{-1}$ ) are the electrical permittivity and the magnetic permeability of free space with  $c = \frac{1}{\sqrt{\mu_0 \epsilon_0}}$  respectively.

Electromagnetic waves of various wavelengths exist. The wavelength of a signal is inversely proportional to its frequency  $f$  ( $\lambda = c/f$ ) which means that the wavelength decreases with an increase in frequency and vice-versa. We will refer to the wavelength in free space as  $\lambda_o$ .

Let us consider the optical view of dielectric behavior. Here we assume a flat slab of material in space. When a TEM wave is incident on its surface both reflected and transmitted waves are created (Fig. 2-3). In this case, the reflected wave is a consequence of the mismatch in the impedances between free space  $Z_o$  and the material  $Z$  ( $<Z_o$ ). A second portion of the remaining wave energy is transmitted through the material. Since the wave velocity  $V$  in the slab

is slower than the speed of light  $c$  in free space, the wavelength of the transmitted light  $\lambda_d$  is shorter than  $\lambda_o$  in free space and we can write the following Equations.

$$Z = \frac{\eta}{\sqrt{\epsilon_r}} \quad \text{Eq. ( 2-12)}$$

$$\eta = Z_0 = \sqrt{\frac{\mu_0}{\epsilon_0}} = 120\pi \Omega \quad \text{Eq. ( 2-13)}$$

$$\lambda_d = \frac{\lambda_o}{\sqrt{\epsilon_r}} \quad \text{Eq. ( 2-14)}$$

$$V = \frac{c}{\sqrt{\epsilon_r}} \quad \text{Eq. ( 2-15)}$$

Since the material will always have some loss, there will be attenuation or insertion loss. For simplicity the mismatch on the second border is not considered in Fig. 2-3.

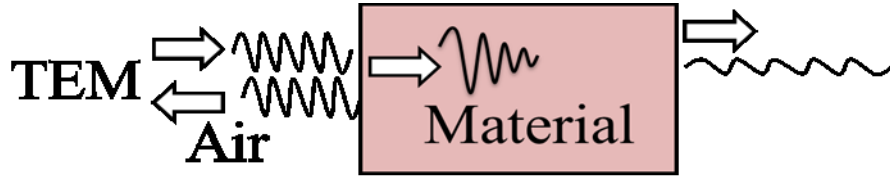


**Figure 2-3 Reflected and transmitted signals for transverse electromagnetic wave (TEM).**

## 2.5 Electromagnetic Wave propagation

A given medium is electromagnetically characterized by three physical properties: the magnetic permeability  $\mu$ , the DC electrical conductivity  $\sigma$ , and the dielectric permittivity  $\epsilon$ . All of these properties are frequency dependent and behave differently with various frequency ranges.

### 2.5.1 Magnetic Permeability

The magnetic permeability  $\mu$  quantifies the capacity of a material to induce a magnetic field  $\mathbf{B}$  within itself when it is inserted into an external magnetic field  $\mathbf{H}$ . That is, when a

material is subjected to an induced magnetic field, magnetic permeability measures the magnetic field energy stored and dissipated in that material [Powers, 1997]. The unit of permeability is the Henry/m (H/m) which is also equivalent to Newtons/Ampere squared (N/A<sup>2</sup>). Permeability  $\mu = \mu_0 \mu^*$  relates the magnetic flux density  $\mathbf{B}$  (in Wb/m<sup>2</sup>) to the magnetic field intensity  $\mathbf{H}$  (in A/m) via  $\mathbf{B} = \mu \mathbf{H}$ . The relative magnetic permeability  $\mu^*$  may also be complex:

$$\mu^* = \mu' - i\mu'' \quad \text{Eq. ( 2-16)}$$

where the real  $\mu'$  and imaginary  $\mu''$  components describe the total induced magnetization (energy storage) and the magnetic hysteresis loss (energy loss), respectively.

In geophysical investigations, it is more common to use the dimensionless volume magnetic susceptibility  $\chi_m = \mu^* - 1$  than the relative magnetic permeability. Some rocks contain magnetic materials such as iron (ferrites), cobalt, nickel, and their alloys having appreciable magnetic properties and it may become necessary to investigate permeability of these rocks with regards to the propagation of EM waves [Mattei *et al.*, 2007; Mattei *et al.*, 2008; Robinson *et al.*, 1994; Van Dam *et al.*, 2002]. However, most rocks, sediments and soils are only weakly diamagnetic or paramagnetic with  $|\chi_m| < 10^{-4}$  and consequently the magnetic permeability of most of minerals studied in this thesis can be ignored. Taking the permeability equal to that of free space ( $\mu_0 = 4\pi \times 10^{-7} \text{ H/m}$ ) suffices for most purposes [Ulaby *et al.*, 2010]. Relative magnetic permeability is expressed by the following equation

$$\mu_r = \frac{\mu}{\mu_0} \quad \text{Eq. ( 2-17)}$$

$$\mu_r \approx 1 \quad \text{Eq. ( 2-18)}$$

### 2.5.2 Electrical conductivity

Electrical conductivity  $\sigma$  describes how much electric current  $I$  exists under an applied voltage  $V$  according to Ohm's Law  $V = I/\sigma$  [Saarenketo, 1998]. The conductivity is described in units of Siemens/m (S/m) or, sometimes in the older literature, Mho/m. The reciprocal of  $\sigma$  is the electrical resistivity given in Ohm-meter ( $\Omega$ -m). Electrical conductivity depends on frequency but its behavior is relatively constant over the typical GPR frequency range of 25-1,500 MHz [Martinez and Brynes, 2001]. Saline ground water and clay surfaces, for example, contribute greatly to the overall conductivity of a given porous material inducing both wave speed dispersion and enhanced attenuation of GPR signals [Cosenza et al., 2003].

### 2.5.3 Dielectric permittivity

Over the GPR frequencies studied here, the dielectric permittivity  $\epsilon^*$  is the most important parameter. It describes the polarization of induced or oriented electric dipoles within a dielectric material. In general, the dielectric permittivity  $\epsilon^*$  is complex and given by

$$\epsilon^* = \epsilon' - i\epsilon'' \quad \text{Eq. ( 2-19)}$$

where  $\epsilon'$  and  $\epsilon''$  are the real and the imaginary components, respectively. The real part  $\epsilon'$ , often referred to as the dielectric constant despite the fact that it usually varies with frequency, describes the ability of the material to store energy by polarization as a result of applying electromagnetic radiation. The imaginary part  $\epsilon''$  describes the energy loss resulting from dielectric hysteresis.

The real and imaginary components are 90° out of phase if we draw the complex dielectric permittivity as a vector representation (Fig. 2-4). Their vector sum forms an angle  $\delta$  with the real axis ( $\epsilon'$ ). The ratio of the energy lost to the energy stored indicates the relative lossiness or loss factor of a material.

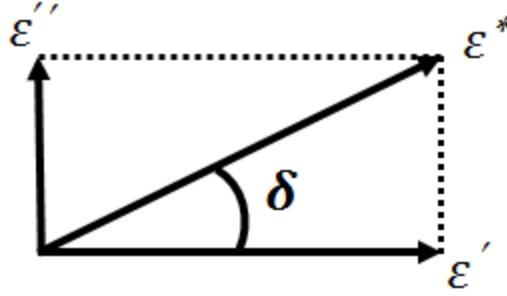


**Figure 2-4 Loss tangent vector diagram.**

From Fig. 2-4 we can write

$$\tan\delta = \frac{\varepsilon''}{\varepsilon'} = D = \frac{1}{Q} \quad \text{Eq. ( 2-20)}$$

$$\tan\delta = \frac{\text{Energy lost per cycle}}{\text{Energy stored per cycle}} \quad \text{Eq. ( 2-21)}$$

Here  $\tan\delta$  is defined as the ratio of the imaginary part of the dielectric constant to the real part which is actually called the loss tangent.  $D$  denotes dissipation factor and  $Q$  is quality factor. The term “quality factor or  $Q$ -factor” is the reciprocal of the loss tangent. For very low loss materials, since  $\tan\delta \approx \delta$ , the loss tangent can be expressed in angle units of milliradians or microradians.

In the microwave region of the electromagnetic spectrum, the loss can be due to the motion of conduction electrons/ions as well as by the dielectric hysteresis lag of dipole rotation behind the rapidly fluctuating electric field. Therefore, the relative equivalent dielectric permittivity  $\varepsilon^{eff}$  can be written as

$$\varepsilon^{eff} = \varepsilon' - i\left[\varepsilon'' + \frac{\sigma}{\omega\varepsilon_0}\right] \quad \text{Eq. ( 2-22)}$$

where  $\omega$  is the angular frequency. This hysteresis yields heating of the material and is the principle of microwave cooking and RF heating. Conversely, we can write the equivalent conductivity

$$\sigma^{eff} = \sigma + i\omega\varepsilon''\varepsilon_0 \quad \text{Eq. ( 2-23)}$$

These imply the dielectric loss increases with frequency while conductivity is an important parameter at low frequencies. As mentioned earlier, the EM wave propagation speed is equal to the speed of light  $c = (\mu_0 \epsilon_0)^{-1/2}$  in free space. Note the velocity of EM wave propagation in Earth's atmosphere near sea level is around 0.3 m/ns but within typical earth materials it is slower and usually between 0.05 and 0.15 m/ns [Baker *et al.*, 2007; Daniels and Engineers, 2004]. This is because the dielectric permittivity of free space is less than the permittivity of any earth materials. More generally, the propagation phase velocity of an EM wave in any media is given by

$$v = \frac{c}{\sqrt{\frac{\epsilon'}{2} [1 + (1 + \tan^2 \delta)^{1/2}]}} \quad \text{Eq. ( 2-24)}$$

where the loss tangent  $\tan \delta$  is:

$$\tan \delta = \frac{\sigma^{eff}}{\omega \epsilon' \epsilon_0} = \frac{\sigma + \omega \epsilon'' \epsilon_0}{\omega \epsilon' \epsilon_0} \quad \text{Eq. ( 2-25)}$$

In a non-attenuating material,  $\tan \delta = 0$  and the simplified Eq. (2.23) reduces to  $v = \frac{c}{\sqrt{\epsilon'}}$ . The reciprocal of  $\tan \delta$  is equal to the quality factor  $Q$  that is defined as the ratio between the average stored energy per cycle to the energy lost per cycle. A consequence of this loss is that the  $\mathbf{E}$  and  $\mathbf{H}$  fields associated with the propagating wave are also out of phase by angle  $\delta/2$ . Loss may also be described through the attenuation  $\alpha$  (in Neper/m)

$$\alpha = \frac{\omega \sqrt{\mu \epsilon'}}{\sqrt{2}} \left[ \sqrt{1 + \left( \frac{\sigma}{\omega \epsilon'} \right)^2} - 1 \right]^{1/2} \quad \text{Eq. ( 2-26)}$$

The reciprocal of  $\alpha$  is called the skin depth and is defined as the depth at which the input energy reduces by  $1/e$  where  $e$  is the base of the natural logarithm. The power dissipation is

$$P = \sigma^{eff} E^2 \quad \text{Eq. ( 2-27)}$$

Moreover, the intrinsic electromagnetic impedance of a material may be given generally by

$$Z = \sqrt{\frac{\mu}{\epsilon_{eff} \epsilon_0}} = \sqrt{\frac{(\mu' - i\mu'')}{[\epsilon' - i(\epsilon'' + \sigma/\omega \epsilon_0)]}} \frac{\mu_0}{\epsilon_0} = c\mu_0 \sqrt{\frac{(\mu' - i\mu'')}{[\epsilon' - i(\epsilon'' + \sigma/\omega \epsilon_0)]}} \quad \text{Eq. ( 2-28)}$$

The impedances control the reflection and transmission of waves across an interface between two materials (1) and (2) of differing complex impedances  $Z_1$  and  $Z_2$ , respectively. The plane wave reflection co-efficient  $R$  for the wave normally incidence from medium (1) from the Fresnel equations [Hecht, 2002] is simply

$$R = \frac{Z_2 - Z_1}{Z_2 + Z_1} \quad \text{Eq. ( 2-29)}$$

$R$  will generally be complex meaning that the reflected wave's phase is rotated upon reflection by the angle

$$\tan^{-1} \frac{\text{Im}(R)}{\text{Re}(R)} \quad \text{Eq. ( 2-30)}$$

A plane wave of Electric field vector  $\mathbf{E}$  that is transverse to the plane of incidence has a reflection and transmission coefficient that assuming  $\mu_1 = \mu_2$  is given by

$$r_s = \frac{n_1 \cos \theta_1 - n_2 \cos \theta_2}{n_1 \cos \theta_1 + n_2 \cos \theta_2} \quad \text{Eq. ( 2-31)}$$

$$t_s = \frac{2n_1 \cos \theta_1}{n_1 \cos \theta_1 + n_2 \cos \theta_2} \quad \text{Eq. ( 2-32)}$$

where  $n_i = c/v_i$  is the refractive index for material  $i$ .

The normal incidence of electromagnetic wave on a surface results in absorption and reflection coefficients (A, R)

$$A = \frac{2\omega}{c} \text{Im} \sqrt{\epsilon^*} \quad \text{Eq. ( 2-33)}$$

$$R = \left| \frac{\sqrt{\epsilon^*} - 1}{\sqrt{\epsilon^*} + 1} \right|^2 \quad \text{Eq. ( 2-34)}$$



## 2.6 Dielectric Measurement Techniques

Dielectric measurements of various materials are finding increasing application with the advances in new materials. Dielectric measurements involve the measurement of the complex relative permittivity  $\epsilon^*$  of a sample under test for a specific orientation of electric field and frequency and several methods exist [Chen *et al.*, 2004; Clarke *et al.*, 2003; Egorov, 2007; Gregory and Clarke, 2006; Kaatz and Feldman, 2006; Krupka, 2006; Stuchly and Stuchly, 1980; vonHippel and Labounskyl, 1995]. The measurement methods can be categorized into two main groups that are referred to as i) wave methods and ii) impedance methods [Clarke *et al.*, 2003]. The wave methods further divided into two types depending on whether propagating or standing waves are employed. These different approaches are briefly reviewed below.

### 2.6.1 Time domain methods

Time domain reflectometry (TDR) is a popular method to obtain estimates of the water content in a material by essentially measuring the transit time of EM pulse through the material being examined. As the theoretical discussions above reveal, the transmission speed depends on the dielectric properties. The first application of TDR was soil-water measurements [Topp *et al.*, 1980], where travel times in co-axial probes the annulus of which were filled with the saturated soils were measured by fitting tangent lines to collected wave form features. The applications of this method can be found in the literature [Chung and Lin, 2009; Dalton *et al.*, 1984; Dirksen and Dasberg, 1993; Jones and Friedman, 2000; Malicki *et al.*, 1996; Robinson and Friedman, 2003; Whalley, 1993]. However, this method has some limitations. This method only provides one value of travel time and hence a single apparent measure of the dielectric permittivity. Previous studies reported the erroneous permittivity due to the uncertainty in the measurement of travel time for soil water content using TDR [Hook and Livingston, 1996; Pepin *et al.*, 1995; Sun

*et al.*, 2000]. Moreover, methods using TDR are not suitable to determine the frequency dependence of electrical properties of soil or related materials.

### **2.6.2 Standing wave methods**

The dielectric properties of rocks and minerals can be measured in the frequency range of 300 MHz to 2400 MHz using standing wave method [Parkhomenko, 2012]. In this method a movable detector is shifted within a transmission line along a standing wave pattern. The permittivity of the sample is calculated by measuring the input impedance of the coaxial section of a waveguide where the rock samples are inserted, The input impedance is acquired from voltage to standing wave ratio for both circumstances (empty and filled with the sample) and the phase shift caused by the sample in the coaxial section [Hoekstra and Delaney, 1974]. This method requires relatively large sample sizes.

### **2.6.3 Frequency Domain Methods**

In frequency domain reflectometry (FDR) method, the dielectric permittivity is usually calculated from the coefficients of EM wave pulse reflection and transmission measured using a network analyzer [Krupka, 2006]. The amplitude and phase of the reflected waves vary with frequency; and therefore the coefficients are complex numbers that account for the phase and the amplitude of the travelling wave [Clarke *et al.*, 2003]. Network analyzers are devices that normally are used to determine the response of electronic devices at RF and microwave frequencies. These devices are usually called the ‘device under test’ or DUT. This is done so that their applicability in circuits of such frequencies can be properly assessed. Their basic operation relies on sending out an EM pulse of known strength and comparing this with the reflection that comes back along the same transmission line. The reflection co-efficient so determined allows the impedance of the device to be calculated [Agilent, 2003]. The same equipment can be

adapted to measure the impedance of materials although this can be problematic if the impedance of the material differs significantly from that for the instrument itself. The range of frequencies of applicability of such instruments is also narrow.

#### **2.6.4 Impedance Methods**

Permittivity measurements using impedance methods rely on the impedance measurements. The best known device for impedance measurements is Schering bridge which is similar to a Wheatstone bridge [vonHippel, 1954]. The unknown impedance can be obtained from the other bridge elements. However, the bridge method encounters a leakage current at higher frequency (above 1 MHz). Moreover, for the measurement of permittivity, the sample is placed between two plates, but if the thickness of the sample is not uniform that results the non-parallel plates as well as air gaps, might produce erroneous permittivity values. Impedance can also be calculated by measuring the current and voltage across a low value resistor.

#### **2.6.5 Current-Voltage IV methods**

This is perhaps the simplest method and as the ‘IV’ method was traditionally applied at lower frequency ranges. In our study we use a higher frequency RF-IV method developed by Agilent [Agilent, 2005] but further details are delayed till later sections. The essential components of an IV measurement system is shown in Fig. 2-5 in which the material to be tested lies between the two plates of a parallel plate capacitor. This is only for purposes of illustration as the RF-IV system used later uses instead an open ended co-axial configuration. The parallel plate capacitor by itself with no dielectric material within it will have an ideal capacitance simply given by  $C_0 = \frac{\epsilon_0 A}{d}$  where  $A$  is the area of the plates,  $d$  is their separation distance, and  $\epsilon_0$  is the permittivity of free space described earlier. It is important to note that this ideal capacitance  $C_0$

depends only on the geometry of the capacitor; the open ended co-axial capacitor used in the actual measurements will have its own value and this is essentially determined empirically as part of the calibration procedure in order to account for variability (see also [Skierucha *et al.*, 2004]).

If we were considering the simple case of constant direct current (DC) then inserting a dielectric material of permittivity  $\epsilon_r$  gives a capacitance of  $C = \epsilon'_0 C_0$ . Consequently if one can leave the charge  $Q$  constant across the plates then one can, in principle, measure  $\epsilon_r$  by simply seeing how much the voltage across the plates would change once the dielectric is inserted. Since in this case  $Q = C_0 V_0 = \epsilon_r C_0 V_1$ , then simply  $\epsilon_r = V_0/V_1$ .

The situation is somewhat different should the material be subject to an alternating current (AC) field which is the situation we must consider here (see for example [Rawlins, 2000]). Let us first examine the case of a perfect (i.e. lossless with  $\epsilon''_0 = 0$ ). Consider the voltage source providing a continuous harmonic signal at constant circular frequency  $\omega = 2\pi f$  and the voltage across the capacitor is described as  $V(t) = V_0 e^{i\omega t}$ . The charge on the capacitor must, too, then vary at the same frequency according to  $Q = VC$  and as such a current  $I(t)$  must also flow back and forth. The charging, and consequently the current flowing, is at a maximum when the rate of change of the voltage is greatest; and this occurs when  $V(t) = 0$ . When  $V(t)$  reaches its extremum values then its rate of change vanishes indicating that no charging takes place and the current goes to 0. In other words  $V(t)$  ‘lags’  $I(t)$  by a quarter of a cycle described in time as  $dt = 1/4f$  or equivalently as a phase angle  $\theta = 90^\circ = \pi/2$ . As a result for this perfect dielectric  $I(t) = I_0 e^{i(\omega t + \frac{\pi}{2})}$ . This gives a relationship between current and voltage with the capacitor essentially opposing the change of voltage; with the analogy to Ohm’s law for the DC case, we can define the impedance of this capacitor to be  $Z = V_0/I_0$  which has units of Ohms. Further, on

average the capacitor opposes the current flow according to a quantity called the capacitive reactance  $X_c = 1/\omega C$  that for this perfect case is the same as the impedance  $Z$ .

Suppose now that the dielectric is no longer lossless and as such one must in addition to the capacitive reactance  $X_C$  include a resistance  $R$  to describe it via  $\mathbf{Z} = R + iX_C$ ; and the magnitude of the impedance now becomes  $|\mathbf{Z}| = (R^2 + X_C^2)^{1/2}$ . Harmonic current is still generated by application of the voltage  $V(t)$  but now the phase angle  $\theta$  is now less than  $\pi/2$  and is given by any of  $\theta = \arccos(\frac{R}{|\mathbf{Z}|}) = \arcsin(\frac{X_C}{|\mathbf{Z}|}) = \arctan(\frac{X_C}{R})$ . It is worthwhile noting that the loss angle mentioned above is related to the phase angle according to  $\delta = \frac{\pi}{2} - \theta$  (see [vonHippel, 1954]). The current now becomes  $I(t) = I_o e^{i(\omega t + \theta)}$  allowing a complex impedance  $\mathbf{Z} = |\mathbf{Z}| e^{i\theta} = (V_o/I_o) e^{i\theta}$ . Therefore the complex impedance can be determined in an IV measurement by simply determining the maximum values of  $V(t)$  and  $I(t)$  and by finding the time shift  $dt$  between them. This time shift is then converted to the phase delay angle  $\theta = \omega t$ .

We can now define a complex capacitance  $\mathbf{C}(\omega) = C_o[\epsilon_r'(\omega) + i\epsilon_r''(\omega)] = [i\omega\mathbf{Z}(\omega)]$  where again  $C_o$  is the empty cell capacitance that depends on the experimental geometry. Hence determining the complex dielectric permittivity  $\epsilon_r(\omega)$  using the IV method depends on the ability to determine  $\mathbf{Z}(\omega)$  (see Section 9.1 of [Czichos, 2006]).

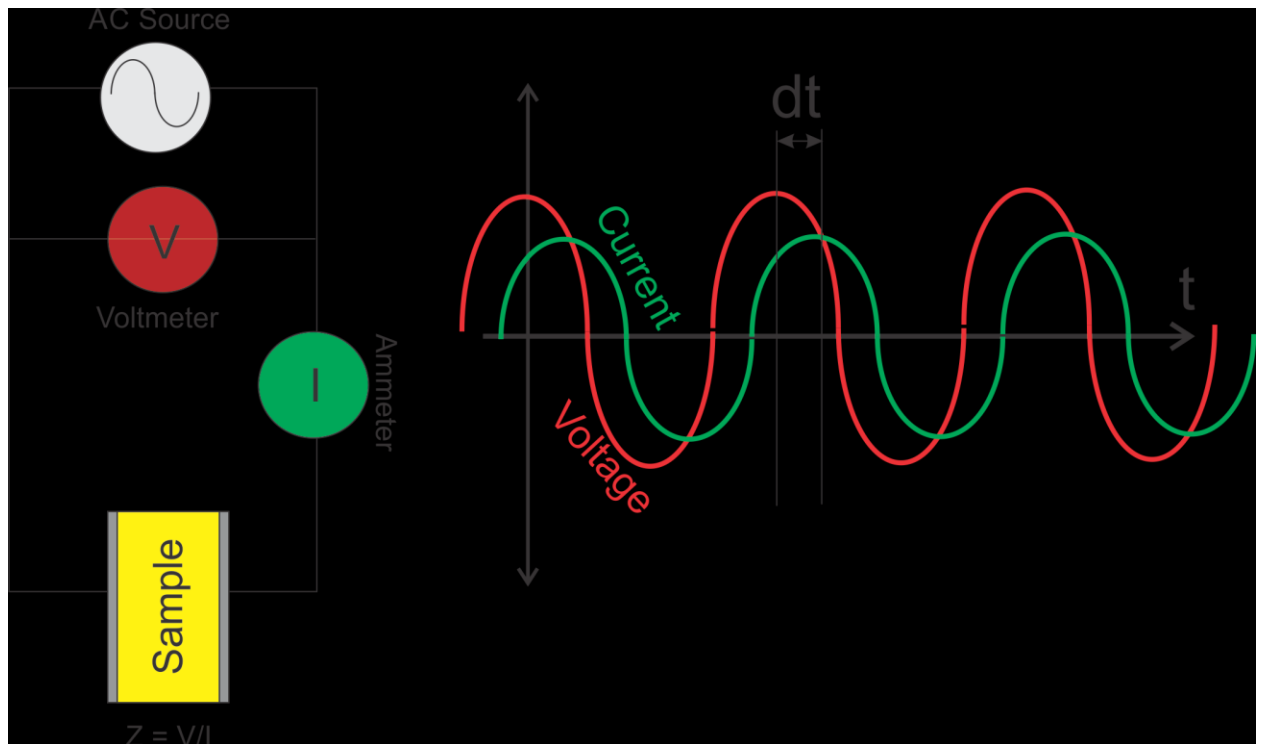


**Figure 2-5 Essential components of an IV measurement system that includes an AC voltage source, a voltmeter to provide  $V(t)$  shown in red in right graph and an ammeter to provide  $I(t)$  shown in green in right graph. The sample is shown as being mounted in between two parallel plates of capacitor in this example. For a perfect lossless dielectric  $dt = 1/4f$  equating to a phase shift angle of  $\theta = \pi/2$ . For a lossy case  $\theta < \pi/2$  and  $dt < 1/4f$ .**

## 2.7 Dispersion

Dispersion refers to the variations in the wave speed and the attenuation with frequency. The propagation of EM radiation in a material result in polarization of its charge carries, which could be either free or bound. There are four polarization mechanisms that can occur depending on the applied frequency (Fig. 2-5). These are electronic, ionic, dipolar and interfacial polarization. The energy loss (or attenuation) occurs when the time scales of the polarization processes is comparable with the frequency of the applied electromagnetic radiation. The timescales of only two of these polarization processes is comparable to the radar frequencies studied here. These are the dipolar and interfacial polarization processes.

Over the range of radar frequencies, all heterogeneous materials and materials that contain permanent dipoles (like water) will experience dispersion. Rocks are mostly made of heterogeneous materials and may contain free water which is perhaps the best known dipolar molecule. Therefore they are expected to show dispersion behavior if water is present. In the absence of water the dispersion is usually minute. The addition of a small amount of saline water however results in strong dispersion especially at the lower frequencies of the GPR (up to 500 MHz).

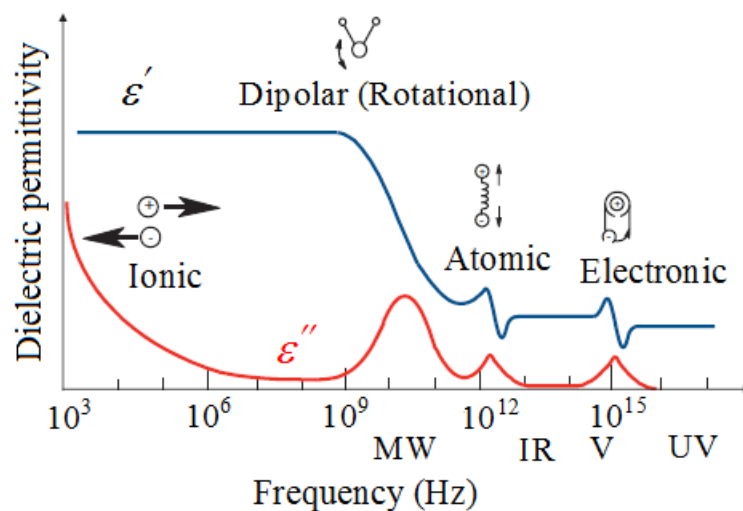


**Figure 2-6 Different polarization processes occur at different frequencies causing dielectric dispersion (Ref after (Agilent)).**

### **2.7.1 Orientation or Dipolar polarization**

Molecules are formed from the combination of various atomic elements each of which will have its own distinctive structure of the cloud of electrons surrounding it. Pure elements, too, can form into crystals that are anisotropic structures and result in the disruption of the electron clouds. An imbalance in the charge distributions will be created due to this rearrangement of electrons with unequal balance between negative and positive charge. Moreover, this imbalance in charge distribution will create a permanent dipole moment. The best

example of such a ‘polar’ molecule is water whose structure that contains two H atoms at the equilibrium angle of  $104.5^\circ$ . Hence, once water is placed in an electrical field, this imbalance places a substantial torque on the molecule forcing it to line up with the electrical field direction.

In absence of an electric field all of the moments of the liquid polar water would be randomly oriented and these random orientations cause the material to be non-polarized. From Fig. 2-7, we can see that the presence of an electric  $E$  creates a torque  $\tau$  on the dipole and the dipole will align along the applied electric field causing dipolar or orientation polarization. The torque will change with the changes in the electric field direction.

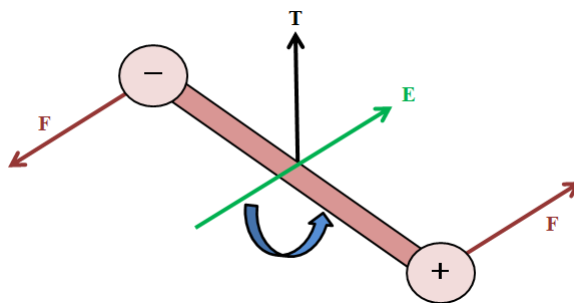


**Figure 2-7 Dipolar rotation in the electric field (Ref after (Agilent)).**

As noted earlier, a propagating EM wave is described in part by a harmonically varying  $E$  field with time. This causes the water molecule to be physically oscillated back and forth with the field variation. However, the molecules cannot do this freely as they collide with one another in the fluid and this causes a ‘friction’ between them that contributes to the loss of energy which heats the material. In relaxation frequency range which occurs mostly in the microwave frequency region, the dipole orientation will create a variation in both  $\epsilon'$  and  $\epsilon''$ . Liquids and gases mainly show this type of polarization.



### 2.7.2 Electronic and atomic polarization

The electronic polarization arises from the realignment of electrons around specific nuclei in presence of an electric field. From Fig. 2-8 we can see that the electron cloud is moved out from the equilibrium trajectory due to the application of an alternating electric field.

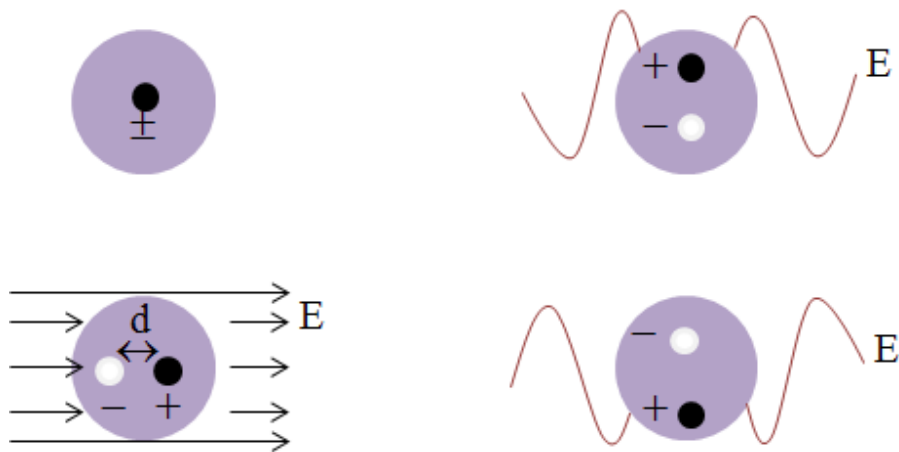


**Figure 2-8 Electronic polarization of atoms.**

The atomic polarization results from the relative displacement of nuclei due to the unequal distribution of charge within the molecule. Alternatively, in presence of an external electric field the adjacent positive and negative ions in an atom are stretched which results into atomic polarization (Fig. 2-9). Though the actual resonance occurs at a much higher frequency, in microwave frequency range these polarizations are dominant over other polarizations for many dry solids.

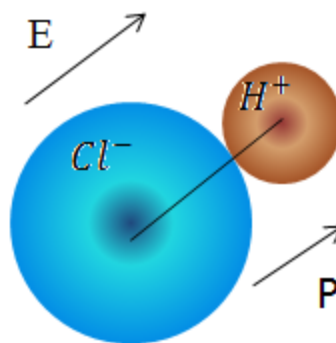


**Figure 2-9 Atomic polarization between ions**

It is important to take the inertia of orbiting electrons into consideration at infrared and visible light range. From Fig. 2-6 we can find that the damping effect of a mechanical spring-mass system and that of atoms containing orbiting electrons are similar except that the resonance frequency the amplitude associated with the oscillation will be smaller. The electronic and atomic polarizations are almost lossless far below resonance frequency and contribute a little to  $\epsilon''$ . The resonant frequency is denoted by a resonant response in  $\epsilon'$  and a peak of maximum absorption in  $\epsilon''$ . Above the resonance these mechanisms have no contribution.

### **2.7.3 Ionic Polarization**

Ionic polarizations are mostly seen in solids having internal dipoles. These dipoles cancel each other out and unable to move under the application of an external electric field. The electric fields slightly displace the ions to induce the net dipoles.

### **2.7.4 Response of Different Polarization to Applied Field Frequency**

The above mentioned polarization mechanisms are functions of the applied field frequency. When the applied field frequency is quite low, all the mechanisms can easily reach to their steady peak value. With increasing frequency it becomes difficult for the polarization

system to reach to the desired peak value. From Fig. 2-6 we can see that when the applied field frequency is  $10^{10}$  to  $10^{12}$  Hz, the dipolar (orientation) polarization becomes unable to reach to its equilibrium value and starts contributing less to the total polarization as frequency increases further. At high electric field frequencies (like infrared and visible light range), electronic and atomic polarization can occur. Each dielectric mechanism has a characteristic cut-off frequency. As the cut-off frequency increases, the slower mechanisms cannot be stimulated and only the faster mechanisms can contribute to  $\epsilon'$ . The dielectric loss  $\epsilon''$  will be peaks at each critical frequency.

#### **2.7.5 *Interfacial or space charge polarization***

The above mentioned polarization mechanisms occur only when charges are locally bound in atoms or molecules. But there is another polarization mechanism where the charge carriers can migrate through the material in presence of an electric field. When the motion of these migrating charges is inhibited it causes a polarization mechanism which is called interfacial or space charge polarization. The motion due to migration can be hindered when charges cannot freely discharge at the electrodes. The interfacial polarization occur when there is a build-up of charges (which can be either free or bound) at the interface. The field distortion caused by the accrual of these charges increases the overall capacitance. Therefore, it will create an increase in  $\epsilon'$  as the effective capacitance of the system increases.

The response of a charge to the nearby charge particles depends on the thickness of the charge layers compared to the particle dimensions. For thin and very small charge layers it will independently respond to the nearby charge particles. The behavior of this type of polarization depends on the frequency range. At low frequencies the charges have sufficient time to gather at the borders of the conducting regions which causes an increase in  $\epsilon'$ . On the contrary, the charges

do not have enough time to gather at higher frequencies. So the polarization is minimal as the charge displacement is small compared to the dimensions of the conducting territory. These frequency effects are known as the Maxwell-Wagner effects.

It is possible to take place some other dielectric mechanisms in this low frequency territory. For example, when the charge layer thickness is the same or larger than the particle dimensions a colloidal suspension exists. Note that colloidal suspension refers to a mixture of particles where colloids (dispersed insoluble particles having the size in the range of 1 to 1000 nanometers) are suspended in a continuous phase of other particles. The response is now dependent on the charge distribution of adjacent particles. Consequently, Maxwell-Wagner effect is no longer applicable [Dyer, 2004].

## 2.8 Dielectric Relaxation

When the applied electric field is removed one might expect the polarization field will also fall zero instantaneously. In real cases, however, it takes some time for the dipoles to return to their random state. The time required for the dipoles to revert to their primary random state is known as relaxation time expressed by  $\tau$ . In other words, relaxation time measures the mobility of molecules in a material.

Fig. 2-10 shows the relaxation time of a dielectric material due to sudden drop in the electric field. All the above mentioned polarization mechanisms can operate until a certain frequency range. After that frequency all the mechanisms will disappear due to any increase in frequency. This frequency is known as relaxation frequency which is represented by  $f_c$ .

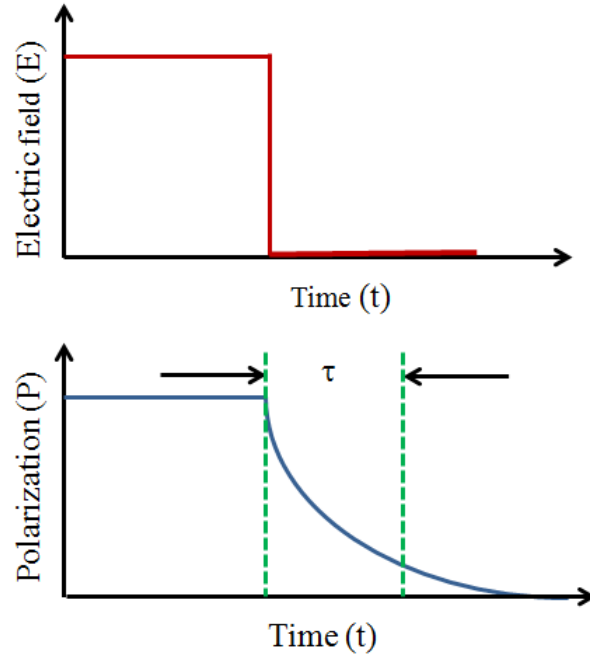


**Figure 2-10 Change in polarization due to sudden change in applied electric field.**

The relaxation frequency ( $f_c$ ) is inversely proportional to relaxation time ( $\tau$ ) as follows

$$\tau = \frac{1}{\omega_c} = \frac{1}{2\pi f_c} \quad \text{Eq. ( 2-35)}$$

Below the relaxation frequency, the dipoles are able to keep pace with the alternating electric field variations. Conversely, above the relaxation frequency the dipoles are not able to track the electric field and as such both the dielectric loss ( $\epsilon''$ ) and the storage ( $\epsilon'$ ) are smaller. Essentially, above the relaxation frequency certain mechanisms are not able to be at all active and they consequently cannot contribute to the overall dielectric permittivity. Therefore, the orientation polarizations disappear.

## 2.9 Debye Relation

Materials having a single relaxation time can be modeled by the Debye relation. Fig. 2-11 shows the dielectric characteristics of water at  $30^\circ\text{C}$  over a certain range of frequencies from 100

MHz to 1 THz. From Fig. 2-11 we can see that dielectric storage ( $\epsilon'$ ) is constant above and below relaxation frequency whereas dielectric loss ( $\epsilon''$ ) is small above and below the relaxation frequency.

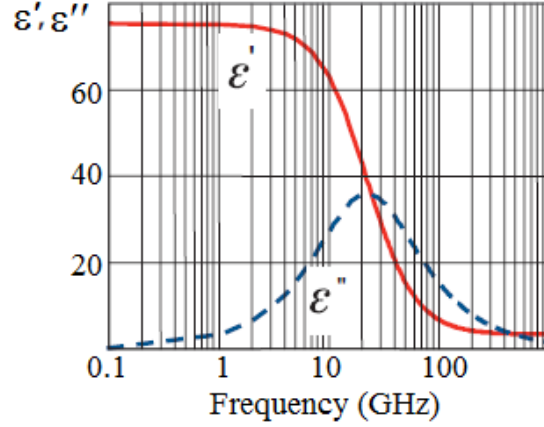


**Figure 2-11 Debye relaxation for water at 30 °C (ref after (Agilent)).**

The Debye theory of complex permittivity gives the permittivity in terms of

$$\epsilon' = \epsilon_{\infty} + \frac{\epsilon_s - \epsilon_{\infty}}{1 + (\omega\tau)^2} \quad \text{Eq. ( 2-36)}$$

and

$$\epsilon'' = (\omega\tau) \frac{\epsilon_s - \epsilon_{\infty}}{1 + (\omega\tau)^2} \quad \text{Eq. ( 2-37)}$$

where,  $\omega = 2\pi f$  ( $f$  is the frequency). For  $\omega = 0$ ,  $\epsilon(0) = \epsilon_s$  and  $\omega = \infty$ ,  $\epsilon(\infty) = \epsilon_{\infty}$

From the Debye relation, it is possible to find out the dependence of permittivity on the applied frequency. It can be seen that  $\epsilon'$  decreases with increasing frequency while  $\epsilon''$  will have a maximum value.  $\epsilon'$  decreases due to the phase lag between the dipole alignment and the electric field.

## 2.10 Cole-Cole Diagram

The Debye relation works if only one pure type of relaxation mechanism exists, but this is rarely the case and a number of different effects can all be active. Instead, the complex permittivity is often displayed using what is called a Cole-Cole diagram. It is one of the better approximations in most of the dielectric cases though Debye relation is also very important. The Cole-Cole diagram is simply a plot of  $\epsilon''$  on the Y-axis and  $\epsilon'$  on the X-axis. Cole-Cole diagram can be expressed by the following equation

$$\epsilon^* - \epsilon_{\infty} = \frac{\epsilon_s - \epsilon_{\infty}}{[1 + (j\omega\tau)^{1-\alpha}]} \quad \text{Eq. ( 2-38)}$$

where  $\epsilon^*$  is the complex dielectric permittivity,  $\alpha$  is the angle between the real axis and the high frequency intercept line drawn to the center of the semi circle.

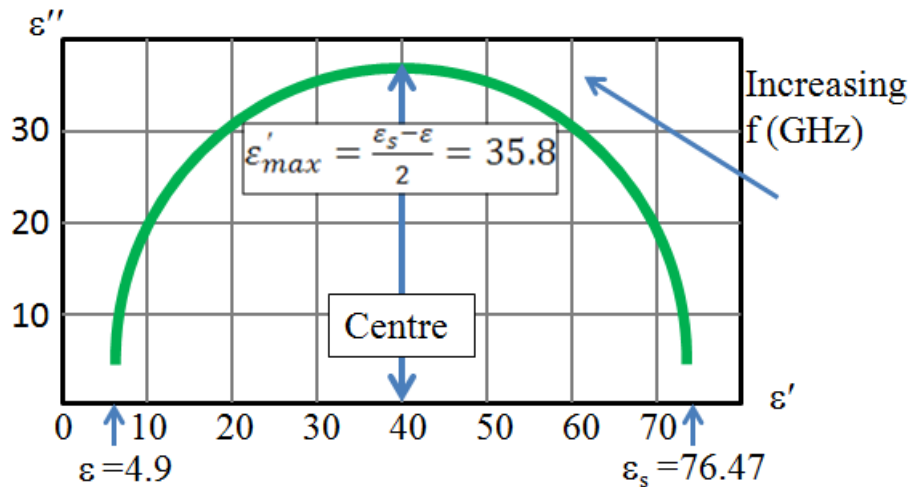


**Figure 2-12 Cole-Cole representation of the Debye model of water at 300C. (ref. after (Agilent)).**

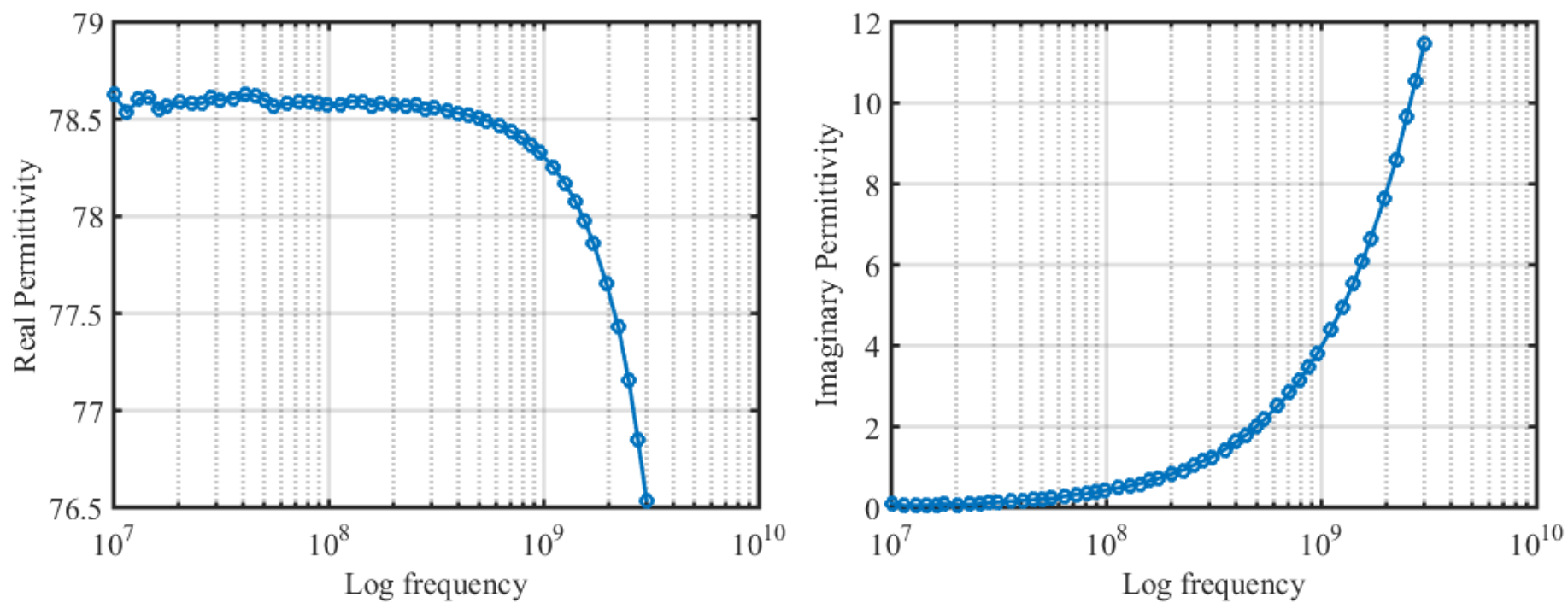
Fig. 2-12 shows the maximum value of  $\epsilon''$  for a dielectric material with a single relaxation frequency. The frequency moves counter clockwise on the curve. If a material has multiple relaxation frequencies which are symmetrically distributed will be a semi-circle. On the other

hand, in case of non-symmetrical distribution it will be an arc. In both cases the center will be lying below the horizontal  $\varepsilon'' = 0$  axis.

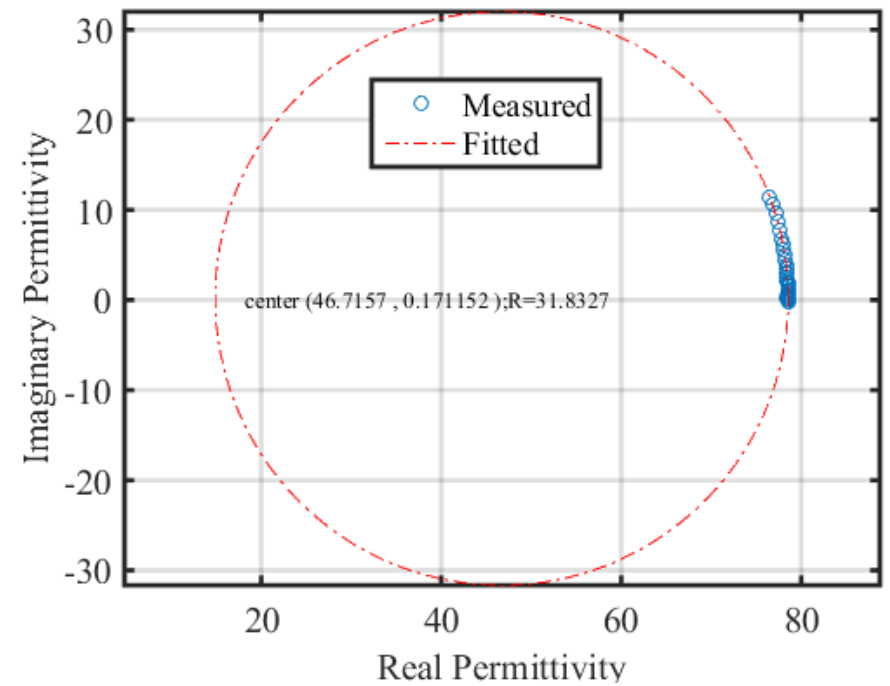
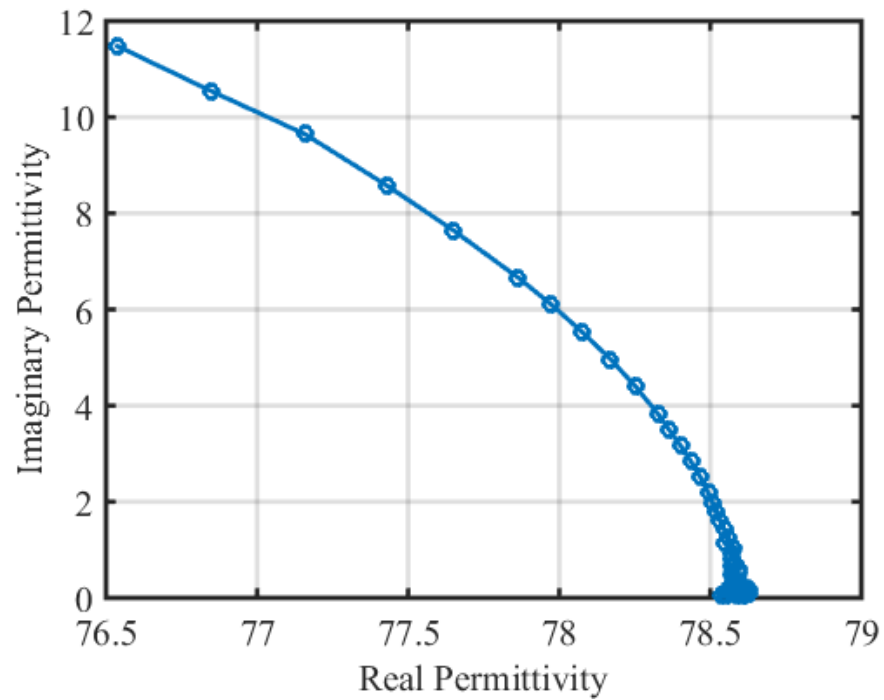
## **2.11 Debye and Cole-Cole diagrams for water from experiments**

Fig. 2-13 shows the Debye plot for water from our experimental data. In this plot real and imaginary permittivities are plotted against frequency. The real permittivity started decreasing at  $\sim 0.5$  GHz. On the other hand the imaginary permittivity started increasing sharply around that of 0.5 GHz. We can compare our measurement result with the Debye approximation in Fig. 2-11. It was not possible for us to figure out the relaxation frequency as our measurement frequency was not high enough like the frequency range used in Fig. 2-11. Fig. 2-14 represents the Cole-Cole plot (left) and a circle fit (right) for water. From the circle fit we can find that the center was not exactly at zero. But an ideal Cole-Cole representation starts from zero. Therefore we can conclude that our experimental data for water was not a perfect Cole-Cole representation.





**Figure 2-13 Debye plots for water from the experimental data**



**Figure 2-14 Cole-Cole plot for water from the experimental data (left). Circle fit of the data is also shown (right).**

## 2.12 Mixing Theories

The theory of the power dissipation of the electromagnetic wave in a medium is straight forward for a single component, homogeneous, isotropic system. However, naturally occurring rocks and minerals are not purely homogeneous systems, but are a mixture of minerals and fluids within the pore spaces. Most rocks are also porous and to some extent saturated with liquids. In addition, rocks are composed of grains with different sizes, shapes, and distributions. The frequency dependent space-charge interactions at the fluid-mineral interfaces, too, influence the observed dielectric properties particularly at low frequencies. All of the mentioned properties of the rock have a measurable effect on the complex dielectric permittivity and therefore complicate the interpretation of the GPR and TDR data. The effect is prominent on the dielectric permittivity measurements of many minerals particularly those for which appropriate single crystals are not available. For this reason, dielectric permittivity of these materials have been measured using mineral powders mixed with air or other well characterized fluids [*Arai and Binner, 1995; Avelin and Sihvola, 2002; Brovelli and Cassiani, 2008; Davies et al., 2005; D. C. Dube, 1970; D. C. Dube and Parshad, 1970; D. C.; Dube et al., 1971; Economos, 1958; Hilhorst et al., 2000; Kingery et al., 1976; Martinez and Byrnes, 2001; Matzler, 1998; Mdarhrj et al., 2008; S Nelson et al., 1989; S. O. Nelson, 1983; 1994; 2001; 2005; S. O.; Nelson and Bartley, 1998; Olhoeft, 1981; Payne, 1973; Reynolds and Hough, 1957; Robinson and Friedman, 2005; Robinson et al., 2003; Rust et al., 1999; Spanoudaki and Pelster, 2001; Widjajakusuma and Biswal, 2003*]. Mixing technique has an advantage over single crystals, assuming the sample's mineral grains are randomly oriented; the dielectric permittivity may be treated as a scalar. However, a major disadvantage of this method is that many such samples are porous and heterogeneous by their nature. Consequently, it is often necessary to measure the permittivity at known density (or

equivalently porosity) and then on the basis of a numerical or theoretical model to extrapolate this value back to vanishing porosity [*S Nelson et al.*, 1989; *Robinson and Friedman*, 2003]. Note porosity is sometimes considered as an additional control to the dielectric properties of advanced components in the electronics industry [*Kata and Shimada*, 1992].

Mixing models attempt to predict permittivity of different mixtures depending on the selected input parameters. Several mixing models have been proposed in the literature to predict dielectric properties of rocks and minerals. These models have been classified into four broad categories: effective medium, empirical or semi-empirical, phenomenological and volumetric [*Knoll*, 1996; *Martinez and Byrnes*, 2001]. Every model has some advantages and disadvantages depending on the assumptions.

In the effective medium approach the dielectric permittivity estimation is based on successive substitutions [*Sen et al.*, 1981]. The Bruggeman-Hanai-Sen (BHS) equation is an example of effective medium theory. This model is robust for the materials with known geometries such as water-saturated materials with non-interacting components. However, the model is not easy to implement and is rarely used in practice.

The empirical or semi-empirical models are based on the mathematical equations (logarithmic or polynomial) that relate dielectric and other measurable properties. These models are easy to implement for complex materials. However, these methods are not suitable for data sets that include the materials with different mineralogies, porosities as well as water saturations [*Dobson et al.*, 1985; *Olhoeft and Strangway*, 1975; *Topp et al.*, 1980; *Wang and Schmugge*, 1980]. Logarithmic and polynomial type theories represent empirical and semi-empirical models.

The phenomenological model is based on the relationship between frequency dependent behavior and characteristic relaxation times. It is not necessary to know the component

properties or geometrical relationship in this model but the model depends on frequency specific parameter. Cole-Cole and Debye models are usually used in the phenomenological approach [Powers, 1997; Wang and Schmugge, 1980].

Another important approach for mixing models is volumetric model in which dielectric properties are estimated from the relationship between the bulk dielectric constant of multiphase mixtures with that of its constituents. Examples of this include the Complex Refractive Index (CRIM) and the Lichtenecker-Rother formula. However, the micro-geometry and the electrochemical interactions between the components are not considered in these types of models [Knoll, 1996; Lichtenecker and Rother, 1931; Roth et al., 1992; Wharton et al., 1980].

In addition, Cosenza et al. classified these into three groups: statistical, numerical and effective medium theory [Cosenza et al., 2003]. In the statistical approach the permittivity is calculated by assuming that the porous medium is a 3-D network of capacitors. In the numerical approach the permittivity estimation is based on the numerical solution of Maxwell's equations at the microstructure level. Both the statistical and numerical techniques require detailed knowledge of the material's microstructure.

The determination of the effective dielectric properties of a mixture has been studied for more than 100 years and consequently a large number of effective medium theories have been proposed [Koledintseva et al., 2009; Sivhola, 2002; van Beck, 1967]. In the effective medium theories the "effective" bulk permittivity is calculated from the individual permittivity of the medium constituents variously weighted by the volume average factor. The basic idea of effective medium theory is to focus on a particular inclusion and it assumes that the inclusion is surrounded by an effective homogeneous medium [Choy, 1999; Myroshnychenko and Brosseau,

2005]. This turns out that there is no correlation between the inclusions in effective medium theories.

Following the lead of many authors we will here attempt to evaluate the effectiveness of a number of different mixing models that are employed in the literature. There are numerous reviews on this topic from various perspectives that may be found (e. g., [A. H. Sihvola, 1989] ). For each we will provide a brief rationale as to how the method was developed and what its major underlying assumptions and limitations might be. It is important to note that most of the mixing models and bounds described here do not contain any detailed information on the material structure and rely solely on knowledge of the constituents permittivities and volume fractions in the mixture.

One of the most popular and widely used formulations for calculating effective permittivity of dilute mixtures is the Maxwell-Garnet (MG) theory which was first formulated for spherical inclusions [Bergman and Stroud, 1992; Sihvola, 1999]. Let us consider a two-phase mixture which consist of two dielectric components; one of them is background that works as a host material, and the other one is inclusion that is embedded as a guest material. The dielectric permittivity and fractional volume of the background material are denoted as  $\varepsilon_1$  and  $f_1$  respectively while  $\varepsilon_2$  and  $f_2$  are the permittivity and fractional volume of the inclusion materials. The Maxwell-Garnet [1904] mixing rule (also called the Clasisus-Mossotti approximation or the average T-matrix approximation [Sen *et al*, 1980] is perhaps the most widely applied in part because of its simplicity for the two-phase mixture can be written as

$$\frac{\varepsilon - \varepsilon_1}{\varepsilon + 2\varepsilon_1} = f_2 \frac{\varepsilon_2 - \varepsilon_1}{2\varepsilon_1 + \varepsilon_2} \quad \text{Eq. ( 2-39)}$$

where  $\varepsilon$  is the effective dielectric permittivity of the mixture. Maxwell-Garnett developed this theory by essentially summing the individual polarizability of individual inclusions generally of

spherical (or ellipsoidal) shape in order to exactly calculate the induced field within the background host material which is then approximately modified to account for the interactions between the inclusions. This is sometimes referred to as a ‘raisin pudding’ model. *Sihvola [1999]* gives a basic yet detailed discussion that goes through the derivation. The Maxwell-Garnet model works well for small concentrations of inclusions in a dielectric host (inclusion volume fraction  $<0.1$ ) [*Spanoudaki and Pelster, 2001*]. The Maxwell-Garnett theory can also be applied to inclusions of any arbitrary ellipsoidal shapes such as spheroids, cylinders and disk through the introduction of depolarization factors. However, any other shapes that are not perfectly ellipsoidal can only be modeled by any closest ellipsoidal shapes, which may provide erroneous results [*Avelin and Sihvola, 2002*]. Robinson and Friedman suggested that the Maxwell-Garnet theory ‘adequately’ described the permittivity of mixtures of glass beads and various fluids particularly for fluids with a large permittivity. The Maxwell-Garnett model, too, can be extended easily to predict the effective dielectric properties of a material with more than two constituents [*Sihvola, 2013*]

It is important to note that one must take great care in deciding which material is inclusion and which is background. It is easily demonstrated by examination of Eq. 2-39 that they are not invertible and the predicted values for the same compositions can be quite different depending upon which role the materials play. This should not be surprising as the Maxwell-Garnett formulation does contain to a degree some information on the structure of the material and how the fields within it are produced. That said, this issue does further suggest that the Maxwell-Garnett model is valid for dilute inclusions.

Bruggeman [1935] proposed a formula which goes by various names such as the symmetric mixing rule or the coherent potential approximation [Sen *et al*, 1980] which is given below

$$f_2 \frac{\varepsilon_1 - \varepsilon}{\varepsilon_1 + 2\varepsilon} + f_1 \frac{\varepsilon_2 - \varepsilon}{\varepsilon_2 + 2\varepsilon} = 0 \quad \text{Eq. ( 2-40)}$$

The main premise of this rule is that there is no one constituent that is considered as either an inclusion or as the background material, the contributions of both are considered equally. As noted by [Sihvola, 2013] one could interpret this model as having the background consist of the homogenized medium itself against which the polarizations may be found. This means there is a fundamental distinction between the Bruggeman and the Maxwell-Garnett models. For denser mixtures or composites Bruggeman theory works better than the Maxwell-Garnett theory.

Power law models are often used to calculate the effective dielectric permittivity, these are essentially weighted averages. For a two-phase mixture, the formula is

$$(\varepsilon)^c = f_1(\varepsilon_2)^c + f_2(\varepsilon_1)^c \quad \text{Eq. ( 2-41)}$$

where  $c$  is a fitting factor ( $1 \geq c \geq -1$ ) [Brovelli and Cassiani, 2008; Guéguen and Palciauskas, 1994] have referred to this as the ‘Lichteneker-Rother’ equation. Various authors have used differing values of  $c$  for a variety of reasons and some examples of power law theories are complex refractive index method (CRIM); Landau, Lifshitz, Looyenga (LLL) equation; and Lichtenecker logarithmic mixture equation. These models are briefly discussed below.

The CRIM formula assumes  $c = 1/2$  and this essentially is equivalent to assuming that the refractive index of the mixture is the arithmetic mean of the constituents refractive indices weighted by their volume fractions. This is also called the Birchak formula [Sihvola, 2013]. This follows from the fact that the refractive index  $n = c/v = c(\varepsilon)^{1/2}$ . For a two-phase mixture, the CRIM equation [Brovelli and Cassiani, 2008] is



$$(\varepsilon)^{1/2} = f_1(\varepsilon_1)^{1/2} + f_2(\varepsilon_2)^{1/2} \quad \text{Eq. ( 2-42)}$$

Probably because of its simplicity, it has been widely applied in Geophysical studies particularly with regards to ground penetrating radar where wave speeds are measured.

Looyenga [1965] developed a model in which  $c = 1/3$ , which is now often referred to as the Landau-Lifschitz-Looyena (LLL) formula and claimed on the basis of comparison to earlier measurements of the dielectric permittivity of a mixture of glass beads and carbon tetrachloride that it was superior to either the Maxwell-Garnett or the Bruggeman models. Looyenga developed his model from first principles by calculating the average dielectric permittivity should a small sphere of permittivity  $\varepsilon_2$  be moved about within a larger sphere of permittivity  $\varepsilon_1$ . The LLL formula then can be written as

$$(\varepsilon)^{1/3} = f_1(\varepsilon_1)^{1/3} + f_2(\varepsilon_2)^{1/3} \quad \text{Eq. ( 2-43)}$$

Lichtenecker and coworker [Lichtenecker and Rother, 1931] developed essentially an empirical expression that would provide an intermediate between the Wiener bounds. Essentially his model is the geometric mean value which can be written

$$\ln(\varepsilon) = f_1 \ln(\varepsilon_1) + f_2 \ln(\varepsilon_2) \quad \text{Eq. ( 2-44)}$$

This empirically derived logarithmic mixing model is also used for fitting experimental data; however previous work [Payne, 1973] revealed that the logarithmic fitting model might work by coincidence. [Reynolds and Hough, 1957] provided a particularly critical review of this model. More recently Zakri *et al.* [1998] claim that there is some situations where it is theoretically justified if the shapes of the inclusions take a beta function distribution.

Sen and coworker [Sen *et al.*, 1981] derived what they refer to as a ‘self-consistent’ formula for a two-phase mixture which is given below

$$\left( \frac{\varepsilon - \varepsilon_2}{\varepsilon_1 - \varepsilon_2} \right) \left( \frac{\varepsilon_1}{\varepsilon} \right)^p = 1 - f_2 \quad \text{Eq. ( 2-45)}$$

where  $p$  is a constant which depends on the geometrical shape of the rock grain. If the rock grain is spherical, then  $p = 1/3$ . Thus the Eq. (2-45) becomes

$$\left(\frac{\varepsilon - \varepsilon_2}{\varepsilon_1 - \varepsilon_2}\right) \left(\frac{\varepsilon_1}{\varepsilon}\right)^{1/3} = 1 - f_2 \quad \text{Eq. ( 2-46)}$$

The derivation of this equation essentially relies on the fact that the pore space network in earth materials remains connected even at very low porosities. As such, they assume that the material can be modelled as mineral grains coated with water and they go forward by assembling the medium from coated grains of arbitrary size. It is important to note that in the same paper Bruggeman [1935] followed by Hanai [1968] developed similar expressions to Eq. 2-46 that start with the Maxwell-Garnett Eq. 2-39.

From different mixing theories we can obtain different effective permittivity values. However, these predictions are limited by some bounds. The mostly used bounds are Wiener and Hashin-Shtrikman. The Wiener bounds are as follows

Weiner upper bound (Wiener<sup>+</sup>)

$$\varepsilon = f_1 \varepsilon_1 + f_2 \varepsilon_2 \quad \text{Eq. ( 2-47)}$$

Weiner lower bound (Wiener<sup>-</sup>)

$$\varepsilon = \frac{f_1 \varepsilon_2 + f_2 \varepsilon_1}{\varepsilon_1 \varepsilon_2} \quad \text{Eq. ( 2-48)}$$

These Wiener bounds correspond to capacitors which are arranged in either parallel or series in a circuit and providing the upper or maximum and lower or minimum bounds [Neelakanta, 1995]. Note Eq. (2-47) is the maximum for both the  $\varepsilon_2 > \varepsilon_1$  and  $\varepsilon_2 < \varepsilon_1$  as well as Eq. (2-48 is) minimum for both cases. It is also useful to make the comparison of the upper (Eq. 2-47) and lower (Eq. 2-48) to the limiting values of  $c = 1$  and  $c = -1$  in the Lichteneker-Rother Eq. 2-41 above.

Hashin-Shtrikman used a variational approach where the upper and lower bounds are shown by the following equations. The Hashin-Shtrikman upper bound (HS<sup>+</sup>)

$$\varepsilon = \varepsilon_2 + \frac{\varepsilon_2 f_1}{\frac{\varepsilon_2}{\varepsilon_1 - \varepsilon_2} + \frac{f_2}{3}} \quad \text{Eq. ( 2-49)}$$

The Hashin-Shtrikman upper bound (HS<sup>-</sup>)

$$\varepsilon = \varepsilon_1 + \frac{\varepsilon_1 f_2}{\frac{\varepsilon_1}{\varepsilon_2 - \varepsilon_1} + \frac{f_1}{3}} \quad \text{Eq. ( 2-50)}$$

We have used all the above mentioned mixing theories to create theoretical models later on in chapter 4. Our rational for using these different models, all of which are popular within the literature whether justified or not, is to see which might best describe our materials such that it could be used in a practical way for predicting dielectric GPR permittivities and wave speeds.

## 2.13 Conclusions

To have an idea about the dielectric measurements we have discussed all the relevant theoretical background of dielectric permittivity and this section also included a review of the pertinent literature. At first we have discussed about dielectric materials, electromagnetic wave propagation and then we have presented different dielectric measurement techniques. At the end of this chapter different mixing theories were presented. We have also presented a literature review regarding to these theories.

## CHAPTER 3. METHODOLOGY

In this chapter we present a detailed discussion of the measurement protocols, the sample preparation techniques, and the advantages and limitations of both measurement system and sample preparation technique.

### 3.1 Measurement System

The measurement system is comprised of an impedance or material analyzer, an open ended coaxial probe, and the associated software necessary to operate the instrument. The impedance analyzer is an *Agilent E4991A* RF impedance or material analyzer in addition with a coaxial probe and software which are included in *Agilent 85070E* dielectric probe kit shown in Fig. 3-1. Moreover, a computer is connected to the equipment to store the measured dielectric data. The coaxial probe in Fig. 3-2 has a 3.5 mm connector which is supported by a 19 mm diameter flange. A cross section of the sensor is shown in Fig. 3-2 (on the right). The flange allows us to perform measurements on smooth and flat surfaced solid samples as well as immersed within liquids and semi-solids. This probe can withstand a wide temperature range from -40 to +200° C. This instrument is designed primarily for measuring the complex dielectric constant from the direct measurement of both current and voltage associated with a given harmonic input of nonmagnetic, isotropic and homogeneous materials over the frequencies ranging from 10 MHz to 3 GHz.

The calibration of the probe is done using three standards that are usually an open circuit, a short circuit, and pure (deionized) water. The dielectric permittivity of water is 80 [*Ellison et al.*, 1996]. Water is often used as a standard because of its well-known dielectric properties. This

instrument provides a measure of the real part of the dielectric permittivity with an uncertainty of about 1% although these uncertainties are higher for the complex components leading to a 5% uncertainty in the quality factor  $Q$  [Agilent, 2005].



**Figure 3-1 Measurement system: Agilent 4991A RF Impedance/Material Analyzer (left), coaxial line sensor (middle), and a magnified picture of the 19 mm diameter sensor (right). Measurements may be obtained over a frequency range of 10 MHz to 3 GHz**

From Fig. 3-2 (right) we can see that the diameter of the outer face of the probe is 19 mm and for accurate measurement there should be no air gaps between the face of the probe and the material surface. Therefore in this experimental setup, the sample is required to be more than 20 mm in diameter with an ‘adequately’ flat surface so that there is no air gap between the sample and the face of the sensor. The manufacturer recommends that the thickness of the sample should be greater than  $20 \text{ mm}/\sqrt{\epsilon^*}$  to avoid edge effects. The calibration can be done from room temperature up to 40° C without significant error due to temperature change [Gregory and Clarke, 2007].

This instrument allows us measurement of the dielectric permittivity under a variety of different sample geometries. However, this open-ended coaxial probe method is practical for the study of earth materials that are difficult to machine into 3 mm thick wafers.

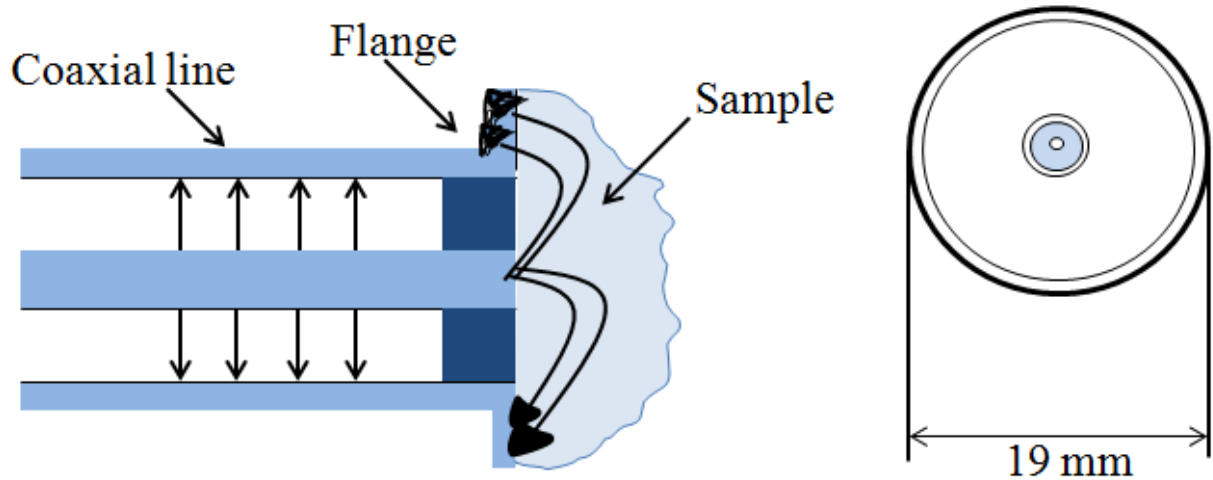


**Figure 3-2 Coaxial probe (left) and a cross section of the sensor. The electric field lines fringe from the end of the sensor into the sample under measurement.**

## 3.2 RF I-V Technique

The basics of the current-voltage measurement technique were provided in Section 2.6.5 and to briefly review this necessitated the determination of the complex impedance  $Z(\omega)$  applying a  $V(t)$  and measuring the resulting  $I(t)$ , which could then be directly related to the real and imaginary parts of the complex dielectric permittivity  $\epsilon_r(\omega)$ . RF I-V method was used as our measurement technique as it provides better impedance measurement capabilities than other existing techniques [Agilent, 2001]. The instrumental setup consists of an impedance matched measurement circuit ( $50\ \Omega$ ) and a precision co-axial test port for operation at higher frequencies. It is composed of two types of basic circuit configurations as shown in Fig. 3-3. Two different types of voltmeter and current meter arrangement provide low impedance and high impedance measurements respectively. The impedance of device under test (DUT) is derived from measured voltage and current values. The current is calculated from the voltage measurement across a known value resistor (R) [Agilent, 2001].

In order to measure a low voltage across the low impedance DUT a low impedance type configuration is used which has a voltmeter adjacent to the DUT for more accurate measurement. While a high impedance type configuration is required to measure a low test current through the high impedance DUT and a current meter is used near the DUT to get more accuracy.

The graph, in Fig. 3-3, shows the relationship of the measured vector voltage ratio to impedance. The solid curves ( $R_x$ ) in the graph apply to resistive DUTs while the broken curves ( $X_x$ ) apply to reactive DUTs. The voltage ratios differ for the reactance and resistance of DUT because the magnitudes of the vector ratios vary depending on the phase angle relationship between the DUT's impedance and the measurement circuit impedance,  $Z_0$ . The resistive DUTs yield greater voltage ratios than the reactive DUTs.

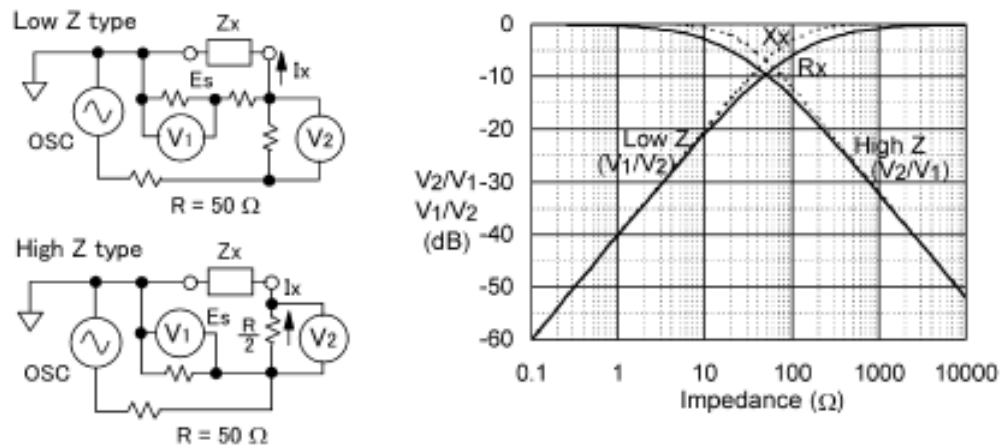


**Figure 3-3 Basic principle of RF I-V technique and vector voltage ratio relationship (ref. after Agilent).**

The detected voltage ratio is proportional to the impedance implies the gradient of vector voltage ratio curve is constant over of the range of impedance. Consequently we obtain constant measurement sensitivity. As the gradient of vector voltage ratio levels off in the high impedance

or low impedance regions the measurement sensitivity deteriorates. However it is possible to selectively install the two types of test heads to complement the two measurements ranges.

The vector voltage relationships can be written as

$$\frac{V_1}{V_2} = \frac{1}{1 + \frac{2R}{Z_x}} = \frac{Z_x}{Z_x + 100}, \text{ for low } z\text{-type} \quad \text{Eq. ( 3-1)}$$

where  $100 = Z_r$  represents the roll-off impedance.

And

$$\frac{V_2}{V_1} = \frac{1}{2Z_x + R} = \frac{25}{Z_x + 25} \text{ for high } Z\text{-type} \quad \text{Eq. ( 3-2)}$$

where  $Z_r = 25$ .

The *RF I-V* circuit can be designed for the roll-off impedance ( $Z_r$ ) value that is properly shifted to wider measurement sensitivity. The Agilent *E4991A* uses the single test head designed in such a way so that it can cover a wide impedance range without any need of exchanging the test heads. Fig. 3-4 represents the vector voltage ratio characteristics of the *E4991A*.

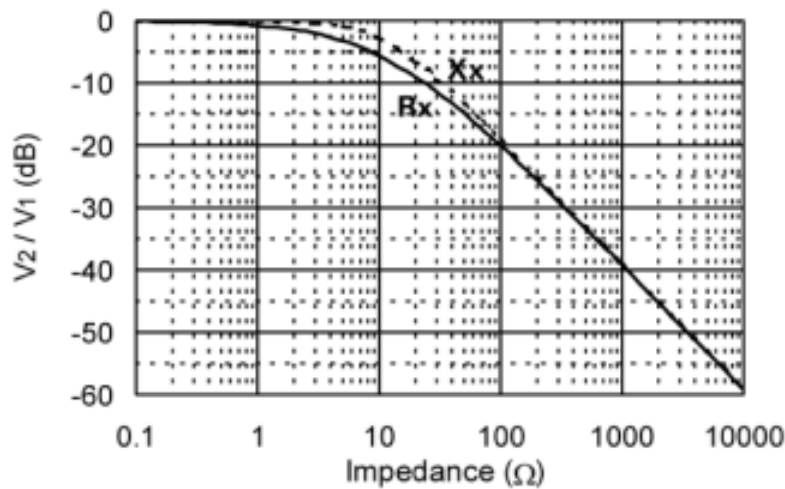


**Figure 3-4 Vector voltage ratio relationship to impedance for E4991A.**



Though it seems the single test head configuration of the *E4991A* sacrifices a little the measurable impedance range when compared to the combined impedance range of the low impedance and high impedance type test heads but in practice, the *E4991A*'s test head does not provide such disadvantages, because the specified measurement range in high frequency region (above 10 MHz) is dominated by the calibration uncertainty [Agilent, 2005]. The advanced design of the *E4991A*'s test head ensures high SNR (signal-to-noise ratio) performance superior to the low and high impedance types of test heads.

### **3.2.1 Calibration**

Outside of factors related to the geometry itself, the accuracy of a measurement system depends mainly on the accuracy of calibration. The calibration of the open ended coaxial probe was performed prior to each set of tests using three standards which are: 1) an open circuit 2) a short circuit, and 3) a reference liquid (de-ionized water). De-ionized water is usually selected because it is readily available, non-toxic and has well known dielectric properties. The instrument includes within its operation known measured values of the complex dielectric constant of water against which the measurement may be compared to provide the calibration.

Further in this study, in order to check the accuracy of the calibration two large high-purity single crystal evaporites (purchased from *Del Mar Photonics*) were measured just after the calibration. These single crystals are halite (*NaCl*) and sylvite (*KCl*). At first we placed these single crystals on the sensor and then took measurements. We repeated the measurement for five times for each of the crystals and then calculated the average of five measurements. They were chosen because of their well characterized dielectric properties [vonHippel, 1954; vonHippel and Labounskyl, 1995; Young and Frederikse, 1973]. These crystals are optically isotropic and

therefore their dielectric permittivities do not depend on crystal orientation. To get accurate dielectric data from these types of crystals it is very important to keep them in a humidity free environment. If we keep it in open places it might absorb moisture and the dielectric data might not be consistent. This turned out to be a problem later in our study as the cover to the desiccator that they normally were stored in was left open to the humid atmosphere. Both the *KCl* and *NaCl* crystal adsorbed water with the loss of their optical clarity and their measured dielectric values making them of no use for checking the calibration. In future, workers must take care to ensure that such crystals are not damaged by exposure to even the small amounts of water in the relatively dry air within our building.

Measures of the real permittivity from 10 MHz to 3 GHz on these large single crystals prior to them being damaged are shown in Fig. 3-5. The dielectric permittivity of halite crystal was measured by *Von Hippel* [1954] who confirm that there exist only a single value of the dielectric permittivity at frequencies between 100 Hz and 25 GHz and with his value being equal 5.90. Lowndes also obtained the same value of the real permittivity (which is  $5.9 \pm 0.02$ ) at frequencies between 100 Hz and 1 MHz [Lowndes, 1966]. We obtained the real part of the permittivity of halite and sylvite single crystals were 5.9 and 4.8, respectively (Fig. 3-5). Repeated measurements at different points on these crystal faces at different times show less than 1% deviation in the measured real permittivity which indicates the consistency of the calibration.

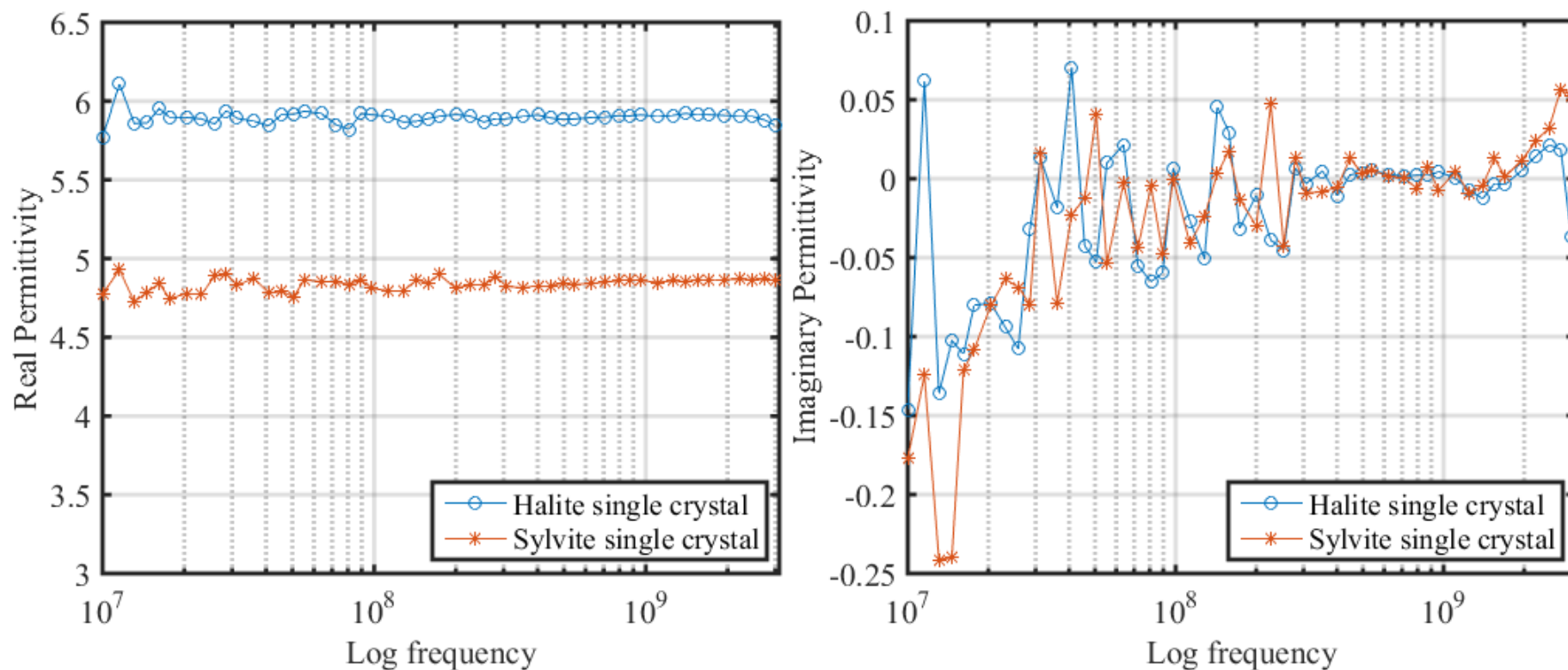


**Figure 3-5 Dielectric permittivity of halite and sylvite single crystal to check the accuracy of calibration of the equipment.**

The imaginary permittivity (Fig. 3-5), on the other hand, was too small to be reliably measured on any of the pure evaporite samples; they fell below the minimum recommended value of our measurements system which was 0.05. According to Von Hippel [vonHippel, 1954], the imaginary permittivity of NaCl crystal is less than 0.003 (at frequency between 100 Hz and 25 GHz). The results, shown in this Fig. 3-5, confirm that the imaginary permittivity is very low but beyond the resolution of the measurement system.

### **3.2.2 *Advantages and Limitations of the RF IV Method***

The coaxial line sensor technique has both advantage and limitations. One of the main advantage of this technique is that it needs a single flat surface of the sample rather than having to machine the sample to fit into a measurement cell [Clarke *et al.*, 2003]. Relatively small samples (of at least 20 mm wide and about 10 mm thick) are required. On the other hand, any air gap between the sensor and the sample is a main source of error in this technique. This can be a problem with real earth materials as they are difficult to machine and polish effectively. Further, even when polished the natural porosity and cracks within such materials will disrupt the proper flow of current in the material. This issue has led us to develop the cold compression technique described below. Moreover, during measurement the cable should be stable otherwise it will create error in the measured dielectric permittivity as well.

## **3.3 Cold Compression Technique**

The problems of attempting to measure the dielectric permittivity of natural samples that contain micro-crack porosity will become increasingly apparent in Chapter 5. Unacceptable results on rock core material led us to use samples reconstituted from powdered materials. In

this section we describe a cold compression technique devised in the laboratory to form such samples for use. A cold compression technique was used to prepare solid samples from mineral powder for several reasons:

- 1) It is not possible to obtain acceptable quality or size single crystals for all minerals.
- 2) Single crystals have crystallographic orientation effects that might give a wide range of dielectric permittivity for each mineral due to their anisotropy.
- 3) The dielectric measurement technique used in our experiment is not suitable for powder. Moreover, it is very sensitive to heterogeneities in the natural sample and to pores and cracks on the surface. In order to provide a homogeneous sample with a flat surface free of cracks cold compression method was designed.

The technique essentially consists of squeezing powder samples at high pressures (up to 300 MPa) for extended periods of time. In this technique, the mineral powder was first ground in a mortar-pestle. The size of the powder particles are less than  $10\ \mu m$ . This powder was then dried in an oven for 2 hours at around  $50^{\circ} C$  to remove all the moisture from the powder. After drying this powder was then poured into flexible plastic tubing the ends of which were then sealed with aluminum cylinders. The ends of these cylinders were polished flat. Hose clamps were tightened around the cylinders in order to hermetically seal the sample. The packing and sealing was carried out as quickly as possible in order to reduce the opportunity for adsorption of water to the surfaces of the powders. The sealed tube was then left heated at about  $60^{\circ} C$  for 2 to 3 hours. This heating was found to improve particle adhesion, and on the basis of experience without this step single unbroken pieces could not be manufactured. In the final preparation step all of the air was removed from the sealed powder by an attached vacuum pump and the sample was vacuumed for at least 1 hour. This pumping helped us removing all the air and this step appears

to have helped to make samples that held together upon decompression. It is likely that any air that remained in the pores prior to pressurization of the sample may force its way out of the sample upon depressurization causing damage.

The assembly was then mounted into a pressure vessel in the Rock Physics laboratory. The sample was then slowly pressurized to the desired peak pressure (~ 150 MPa to 300 MPa) depending on the plasticity of the mineral and then left at this pressure overnight (for at least 14 to 16 hours and sometimes longer). The sample then was depressurized slowly. We depressurized in increments of 10 MPa every 5 minutes, an entire depressurization would usually take more than 2 hours. Experience showed that those samples rapidly depressurized were weak and usually failed upon removal from the assembly.

The samples obtained were one inch in diameter and a few centimeters thick, this depended on the amount of power placed in the assembly. Examples of the synthetic samples are shown in Fig. 3-6. Because the powder of different minerals possess different elastic and creep properties, the same value and duration of pressure produces varying porosity for different mineral powder. For example, pure *KCl* and *NaCl* samples were easily fabricated with nearly no detectable porosity due to their inherent plasticity by applying pressures less than 270 MPa. Calcium carbonate is much more rigid; porosities of 35% could be achieved by elevating the pressure to 270 MPa.

### 3.3.1 *Advantages and Limitations of the Cold Compression Technique*

A great advantage of this process was that as samples were prepared from mineral powder compression, the sample grains would be randomly oriented and due to this dielectric permittivity the sample could be treated as scalar. As a result, the crystal orientation effect can be avoided. However, a prominent limitation of this technique is that even after applying high pressure some mineral samples remain very porous. In addition, this technique is time consuming (typically 18 to 20 hours required to prepare a single sample).



**Figure 3-6 Synthetic sample (NaCl and KCl) prepared using cold compressing technique.**

## 3.4 Material Characterization

A number of additional common experimental methods were employed to further characterize the materials studied. In particular, it is important to have some understanding of the composition and of the structure of the materials. We briefly provide an overview of these techniques here in order that the reader better understand the results in later sections.

### ***3.4.1 Scanning Electron Microscope (SEM)***

The Scanning Electron Microscope (SEM) provides visualization of tiny features of an object. It is similar to conventional optical microscope but light is replaced by electrons (either secondary or back scattered electrons). A very thin beam of electrons (primary electrons) from an electron gun are focused on a small area of a sample kept in the SEM scanner; these electrons interact with atoms in the sample producing various signals (secondary electrons) that can be detected and amplified using electron detector and an image is produced. SEM can produce images submicron resolution. The SEM imaging was done using a Zeiss EVOMA 15™ machine located at the Earth and Atmospheric Science Department at the University of Alberta. SEM assists to examine the grain structure and micro features qualitatively.

Before scanning the samples we need to prepare them for the measurements. The samples (both natural potash and cold compressed) were broken into small pieces as our samples were larger than the instrument could accommodate. The required size for this type of measurement should be less than 1.5 cm in diameter and 1 cm high. In our case the broken pieces were around 0.7 to 0.8 cm in diameter and the thickness were around 0.4 to 0.5 cm. Before scanning the samples were coated with electrically conductive carbon which can prevent electron traps which might make a brighter image. This type of carbon coating is done by thermal evaporation. However, sometimes if the sample is thick enough a small amount of colloidal graphite is printed onto one edge of the samples (used as an adhesive) to bridge the samples to the conductive substrate or the aluminum stubs. The samples are then kept in an oven overnight for thermal evaporation.



### 3.4.2 Helium Pycnometer

The mineral grain volume and hence grain density of the sample can be measured using a helium pycnometer. In this work, a multi-pycnometer (Quantachrome MVP-D160-E™) under helium was used. The pycnometer works based on Boyle's law which states that at a constant temperature, the volume of a given amount of ideal gas is inversely varied with the pressure of the gas. That is,

$$P_1 V_1 = P_2 V_2 \quad \text{Eq. ( 3-3)}$$

where  $P_1$  and  $P_2$  are initial and final pressures of the gas and,  $V_1$ ,  $V_2$  are initial and final volumes. The pycnometer contains two cells: one is as reference while other is for the sample. The idea is to fill the reference cell with helium and measure the pressure  $P_1$  while the volume  $V_1$  of the cell is known. The helium gas is allowed to flow into the other cell where the sample is placed and the pressure  $P_2$  of that cell is measured. The volume  $V_2$  can be calculated from the above Eq. (3-3) Therefore the Equation becomes

$$P_1 V_r = P_2 (V_r + V_s - V_g) \quad \text{Eq. ( 3-4)}$$

or,

$$V_g = V_s - [(P_1 - P_2)/P_2]V_r \quad \text{Eq. ( 3-5)}$$

where  $V_r$  is the volume of the reference cell,  $V_s$  is the volume of the cell containing the sample and  $V_g$  is the volume of the solid portion of the sample. That is,  $V_2$  gives the total volume of the reference cell plus the cell containing the sample minus the grain volume of the sample. Therefore, the porosity  $\phi$  can be obtained using the following Eq.

$$\phi = 1 - \frac{V_g}{V_b} \quad \text{Eq. ( 3-6)}$$

where  $V_b$  is the bulk volume which is the sum of solid sample volume and pore space volume. Using this technique we have calculated the porosities of couple of our samples.

As our samples were not of regular shape it was not possible for us to calculate their bulk volume using the length and diameter of the samples. At first we have used plastic wrapper to wrap up the samples. We wrapped up the samples using a vacuum sealer to make sure that there is no air after wrapping up the samples. Then we inserted the samples into the sample cell of the helium pycnometer and repeated the above mentioned working principle. The volume obtained after the measurements were considered as the bulk volume with plastic wrapper as the helium gas could not penetrate the plastic wrapper. Next, we calculated the bulk volume of the plastic wrapper. By subtracting the bulk volume of the sample with wrapper from the bulk volume of plastic wrapper we have calculated the bulk volume of the sample. Calculating the porosity of irregular shaped sample was a novel application of this technique.

### 3.4.3 *Mercury Porosimeter*

We measured porosity of a limited number of the samples using a mercury injection porosimeter. This Porosimeter ('Micrometrics' AutoPore IV 9510™) characterizes porosity of materials by applying different pressure levels to a sample placed in a Hg bath. A mercury porosimeter measures the pore-throat size distribution and the measurement is based on forcing mercury into small spaces, pore throats within the sample [Giesche, 2006]. Therefore, mercury porosimetry technique can be described using Washburn capillary law:

$$D = \frac{4\gamma\cos\theta}{P} \quad \text{Eq. ( 3-7)}$$

where  $D$  represents the diameter of pore throat,  $P$  is the applied pressure,  $\gamma$  is the surface tension of mercury, and  $\theta$  is the contact angle. Note the Washburn formula is based on the assumption that the pores are cylindrical. But there are no cylindrical pores for any porous medium; this equation is usually used to calculate a pore throat size distribution. This measurement is done by

measuring the volume of injected Hg to the sample with pressure. The equation used in this measurement is

$$\delta V_{Hg} = \frac{dV_{Hg}}{dP} \Delta P \quad \text{Eq. (3-8)}$$

Here  $V_{Hg}$  is the volume of the mercury injected and P represents the applied pressure. From Eq. (3-8) we can see that the volume changes with the change of pressure when the mercury injected into the pore space. Fig. 3-7 shows the plot of incremental and cumulative intrusion with pressure for a porous NaCl sample. We converted pressure to pore size using Washburn's equation. The porosity is simply ratio of the volume of the Hg injected at the highest pressure to the bulk volume of the sample as given by the porosimeter at low pressure.

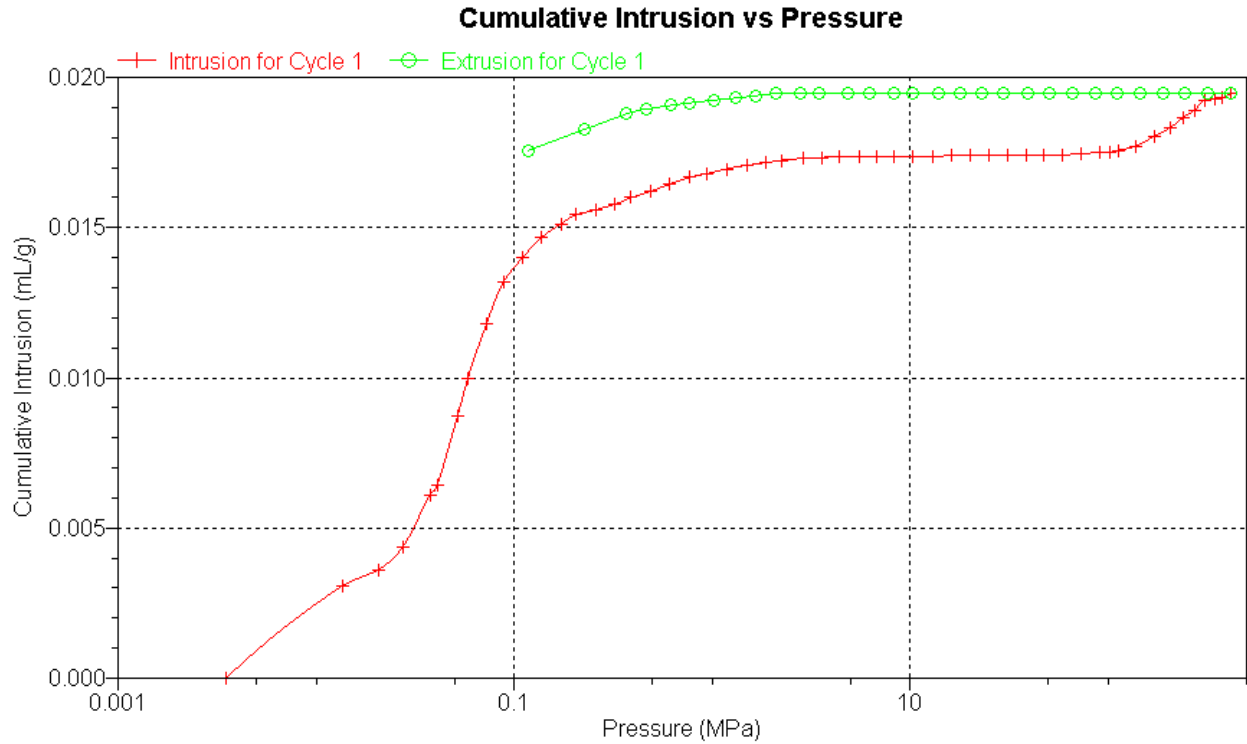


**Figure 3-7 Cumulative intrusion versus pressure for a porous NaCl sample (measured porosity 4%) using Hg porosimeter.**

#### **3.4.4 X-ray Diffraction (XRD)**

X-ray diffraction (XRD) is widely used in geosciences to identify minerals within rocks particularly the fine grained minerals such clays and mixed layers of clays. The basic principle of XRD is the constructive interference of monochromatic x-rays within lattice planes of the minerals. X-ray diffractometers are mainly composed of three parts such an X-ray tube, an X-ray detector and a sample holder. X-ray radiations are generated in a cathode ray tube. These x-rays are directed toward the sample after filtering to produce monochromatic x-rays and collimating them to concentrate. These x-rays interact with the sample and produce constructive interference when the condition for Bragg's law ( $2d\sin\theta = n\lambda$ ) where  $d$  is the spacing between the sample,  $\lambda$  the wavelength,  $\theta$  the diffraction angle) is satisfied. The diffracted x-rays are detected and processed by the x-ray detector, and each mineral will have a characteristic set of diffraction peaks that may be used to identify it.

#### **3.4.5 X-ray Fluorescence (XRF) Elemental Analysis**

For elemental analysis, x-ray fluorescence (XRF) is widely used. This analytical technique is advantageous as all kind of samples (solid, liquid or powder) can be analyzed. XRF provides very accurate and precise measurements and the sample preparation is fast and simple. The basic principle of XRF is based on the source, samples and the detection system. When a sample is exposed to a source of high intensity x-rays, the atoms of the samples become temporarily excited by absorbing energy from the x-rays. If the energy of x-rays is sufficient to dislodge a tightly-bound inner shell electron, the electron cloud become unstable and the missing inner shell electron is replaced by an outer shell electron dropping down. Consequently energy is released in the form of secondary x-rays with energy lower than primary incident x-rays. These 'fluorescent' secondary x-rays are highly tuned to the quantum mechanical energy levels of each

element. The energy differences between the electron shells are fixed and known for each element, so the energy of x-ray fluorescent are unique and can be used to detect the elements present in the samples. The intensities of the different quantum peaks then reveal the concentration of each element within the sample.

### **3.5 Summary**

This chapter includes a description about the dielectric permittivity measurement technique that has been used in our laboratory. Initially we discussed the measurement system, its calibration, and its advantages and limitations. Then the sample preparation technique has been presented. Moreover, the advantages and limitations of this sample preparation technique has been presented. The chapter concluded with a description of the various techniques used in characterizing the material.

# **CHAPTER 4. MEASUREMENTS ON MINERALS AND SYNTHETIC SAMPLES**

## **4.1 Introduction**

Our earliest work on the potash materials (delayed until Chapter 5) showed that it was difficult to obtain a proper measure of the dielectric properties from the core material directly. This motivated us to first step back to examine simpler materials beginning with gem-quality single crystals of the minerals important within the potash mines and leading to the development of the cold compression technique to make reconstituted samples. Hence, before describing the material made from actual cores, we first present measurements on the natural single crystals. This is followed by tests carried out on a variety of cold compressed synthetic samples with particular care to include the effects of porosity. Finally, we discuss these observations in light of the theoretical effective medium mixing-models described in Chapter 2. At the very end of this chapter we have compared our measurement values with the existing mixing theories.

## **4.2 Single Crystal Measurements**

Measurements of the dielectric permittivity of single crystals using the coaxial line sensor technique requires a relatively large crystal of flat and smooth faces of at least 2 cm in diameter and at least 1 cm thick according the instrumental requirements outlined earlier. High quality, pure and naturally occurring single crystals are not easily attainable. Therefore, sometimes we tried to manage large single crystals of high purity that are used primarily for infrared (IR) optics. Fig. 4-1 represents a group of synthetic and natural single evaporite crystals used in the tests here. Dielectric permittivities acquired from the crystals along different directions are

summarized in Table 4-1. The permittivity values are an average of five measurements over the frequency range 10 MHz to 3 GHz.

**Table 4-1 Average real dielectric permittivity for single crystal evaporate minerals over 10 MHz to 3 GHz.**

<b>Crystal</b>	<b>Source</b>	<b>Direction</b>	<b>Permittivity</b>
Halite	Synthetic (from Del Mars photonics Co.) (Fig. 1a)	Average of [100], [010], [001] faces	5.87-5.91
Sylvite	Synthetic (from Del Mars photonics Co.) (Fig. 1b)	Average of [100], [010], [001] faces	4.74-4.82
Calcite	Natural from Brazil (Wards Scientific Co.) (Fig. 1b)	Parallel to the optical axis	8.8—8.95
		Perpendicular to the optical axis	8.30-8.53
	Natural from Mexico (Fig. 1c)	Along $[1\ 0\ 1]$	6.79-7.73
		Along $[1\ 0\ \bar{1}]$	5.43-7.83
		Along $[0\ \bar{1}\ 0]$	6.77-7.90
gypsum	Selenite from Pezuna mine, Naica, Chihuahua. (Fig 1d)	Along $[0\ 1\ 0]$	5.68-6.28
	Gypsum (Fig. 1e)	Along $[0\ 1\ 0]$	5.68-5.92
	UoA museum (Fig. 1f)	Along $[0\ 1\ 0]$	5.90-6.34
	Tyson fine (Fig. 1g)	Along $[0\ 1\ 0]$	5.82-6.29
Dolomite	Tyson fine (Fig. 1h)	Along $[1\ 0\ 1]$	6.20-7.05

The measured permittivity value of the halite crystal was ~5.9 and for sylvite crystal it was ~ 4.8 over the frequency range 10 MHz to 3 GHz. These values did not vary significantly with the change of crystallographic direction on the samples. This lack of variation with direction is likely because halite and sylvite are both optically isotropic crystals. The term isotropic crystal means the crystal that does not change the refractive indices with the change of its crystal axis.

However, we obtained different permittivity values (5.43 to 8.95) for the calcite crystals depending on the crystal orientation. Calcite is a well-known and highly anisotropic crystal that displays a large birefringence at optical frequencies. The refractive index  $n$  is related to the relative dielectric permittivity via the following Eq.

$$n = \frac{c}{V_p} = \sqrt{\epsilon\mu} \quad \text{Eq. ( 4-1)}$$

Refractive indices of rock forming minerals at optical frequencies have long been studied and a large literature exists such as [Dragoman and Dragoman, 2002]. Generally, at visible optical frequencies there are two possible orthogonal polarizations of the light possible in each direction through the material and in general the refractive indices of both of these will be different. This directional variation in the wave speed leads to well-known birefringence effects that have long been exploited by petrologists for mineral identification and orientation. This anisotropy holds for all minerals except for those such as halite and sylvite with cubic symmetry which are optically isotropic and hence have only a single refractive index that applies in all directions.

Measurements of the birefringence of single crystals, of multicrystalline solids, or porous media at GPR frequency ranges are almost nonexistent in part because the relatively long



wavelengths require large samples but also because of difficulties in setting up such experiments. Unexpectedly, the phenomena is perhaps best observed by deep GPR soundings in nature over large glaciers or ice sheets where flow of the ice results in preferential alignments of the ice crystals [Drews *et al.*, 2012; Hargreaves, 1977] or in radar reflectivity from moving sea ice [Kovacs and Morey, 1978]. Anisotropy has also been observed over well characterized rock masses [Sylvie, 1994]. Unfortunately, laboratory measurements of this anisotropy, particularly over the range of frequencies encountered in GPR are rare. Some examples include those of [Hargreaves, 1978; Matsuoka *et al.*, 1997]. Previous several workers [Khanna and Sobhanad, 1972; Sastry *et al.*, 1988] provided measurements of the dielectric permittivity in different directions relative to the crystallographic axes at radio frequency (RF) range. However, to the best of our knowledge there are no reported birefringence measurements at the frequencies used in our study on single crystals of the evaporate minerals.

For the present project, the birefringent effects in composites of randomly oriented and cubic halite and sylvite should not be of critical importance because such multicrystals are expected to be isotropic to EM radiation. Since different dielectric values were obtained due to birefringence of a single crystal, we did not further proceed with these crystals. Moreover, potash does not consist of single mineral; it is a mixture of mostly *NaCl* and *KCl* contaminated with other minerals. This is one of the reasons we developed the cold compression technique to reconstitute the samples.

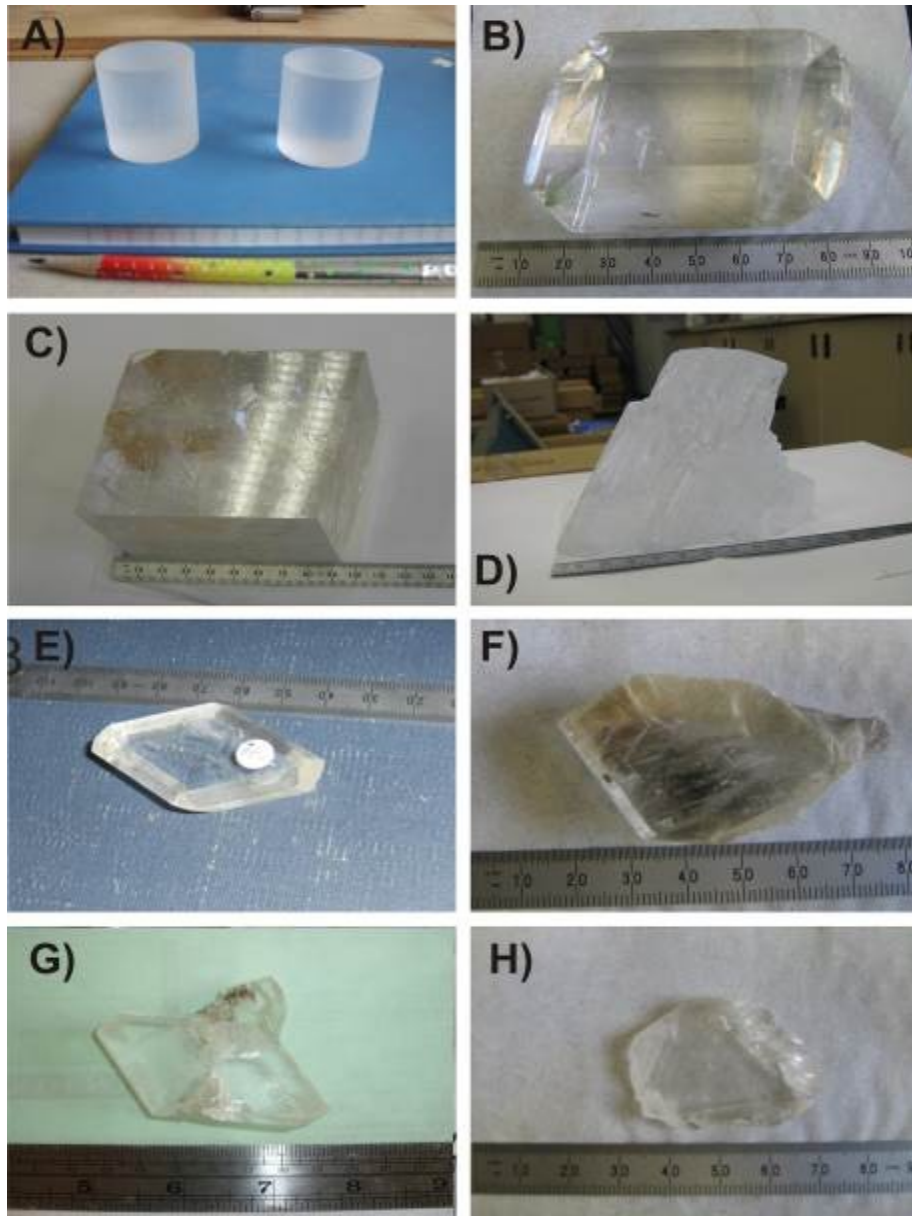


**Figure 4-1 Group of single evaporite crystals. A is halite and sylvite, B and C are calcite, D, E, F and G are gypsum and H is dolomite.**

### 4.3 Measurement on cold compressed halite and sylvite samples

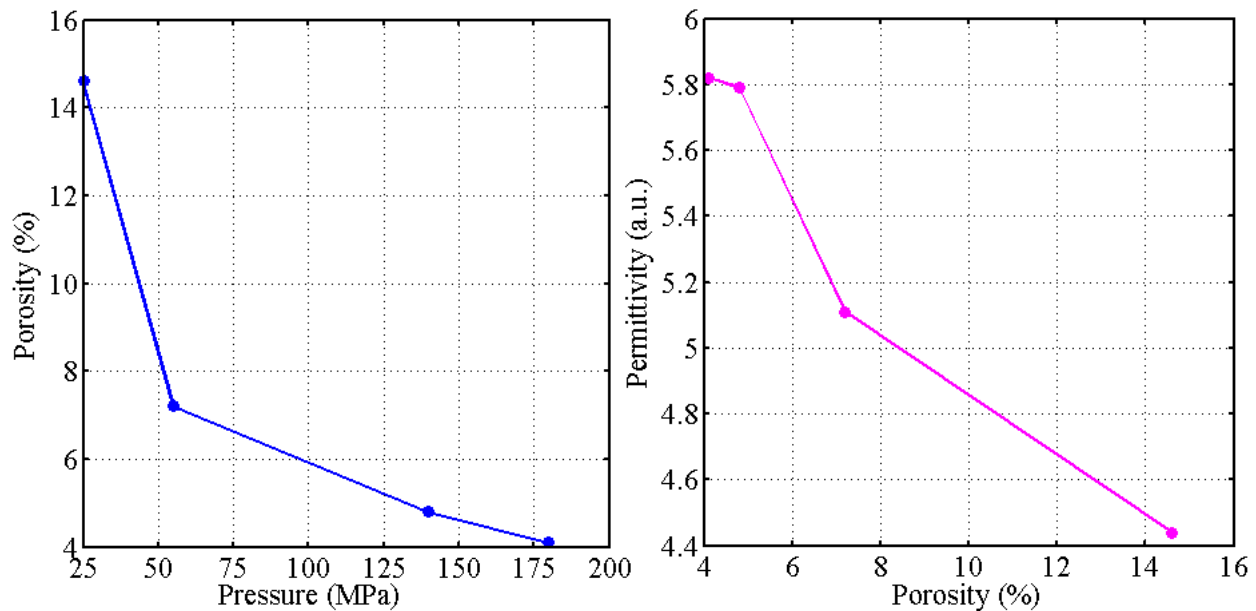
As mentioned earlier (Chapter 3), the cold compression technique was developed for measuring the dielectric permittivity of mineral mixtures such as NaCl and KCl. The plastic deformation behavior of these minerals is well known [*Hardy and Langer, 1989; Senseny et al., 1989*]. A variety of pellets were made using progressively higher pressures in order to evaluate the relationship between peak compression and porosity, this was important to test as we hoped to obtain pore free samples. We use different pressure to find how the porosity changes with increasing pressure and at what pressure most reduces the porosity.

Table 4-2 lists the four NaCl samples that were prepared using cold compression technique. The samples were compressed at different pressure and their porosities were measured using mercury injection porosimetry. The sample compressed under 180 MPa shows ~4% porosity. This measurement shows the possibility of getting nearly pore free samples if we exceed 180 MPa.

**Table 4-2 Dielectric permittivity and porosity values for synthetic NaCl samples compressed at different pressure. Porosity values using mercury porosimeter.**

Sample	Maximum pressure (MPa)	Porosity (%)	Mean permittivity
Compressed NaCl	180	4.1	5.82±0.06
Compressed NaCl	140	4.8	5.79±0.23
Compressed NaCl	55	7.2	5.11±0.12
Compressed NaCl	25	14.6	4.44±0.07

**Note: Data are reported as mean ± standard deviation.**

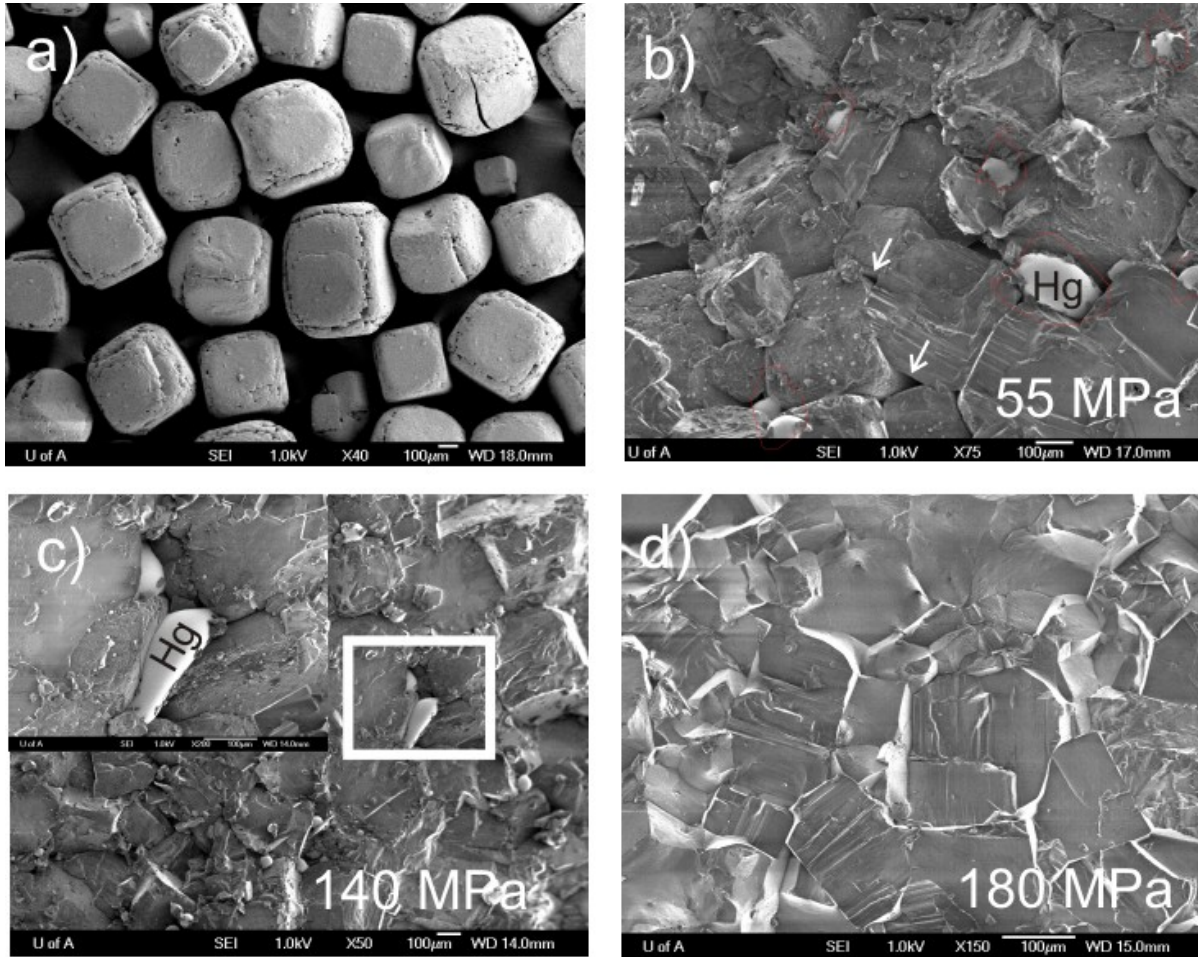


**Figure 4-2 The variation of porosity with pressure and the variation of permittivity with porosity of four halite samples (porosity were measured using mercury porosimeter).**

Fig. 4-2 shows the variation of porosity with pressure and permittivity with porosity. We found that porosity decreases with increasing pressure and permittivity decreases with increasing porosity.

Scanning electron microscopy images of the four NaCl samples after Hg injection porosimetry are shown in Fig. 4-3. Fig. 4-3(a) represents the original NaCl crystals from which the cold compressed samples were prepared. After pressurizing the samples at 140 MPa for 12 hours, some porosity still remained Fig. 4-3(c) The SEM images showed that Hg was able to penetrate into the sample; and the Hg clearly highlights the location of the porosity. However, from Fig. 4-3(b) it was found that at 55 MPa pressure the pores that did not retain Hg, it is not known whether the Hg from these pores drained out or whether the Hg never accessed these pores. With this uncertainty, the measured porosity should be taken as a lower limit for the samples. Despite this, the last image of Fig. 4.3(d) shows the sample compressed at 180 MPa,

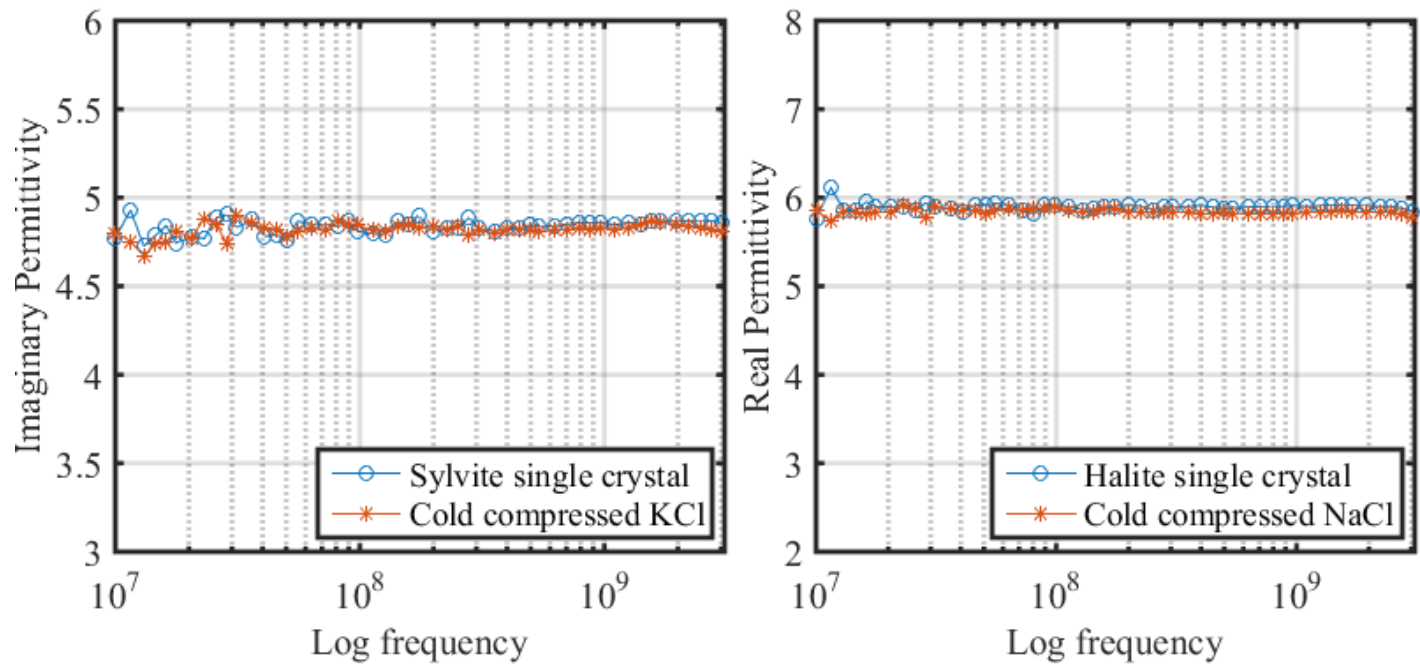
which does not display any open pores or retained Hg suggesting that the cold compression to these pressures produces, with NaCl, acceptable multicrystalline. Though at 180 MPa there were still some porosity present and porosity is about 4.1% according to Table 4-2, it still suggests that using pressure more than 180 MPa can help us to make nearly pore free sample. We have proven this on another NaCl and KCl sample measurements which is shown in Fig. 4-4.



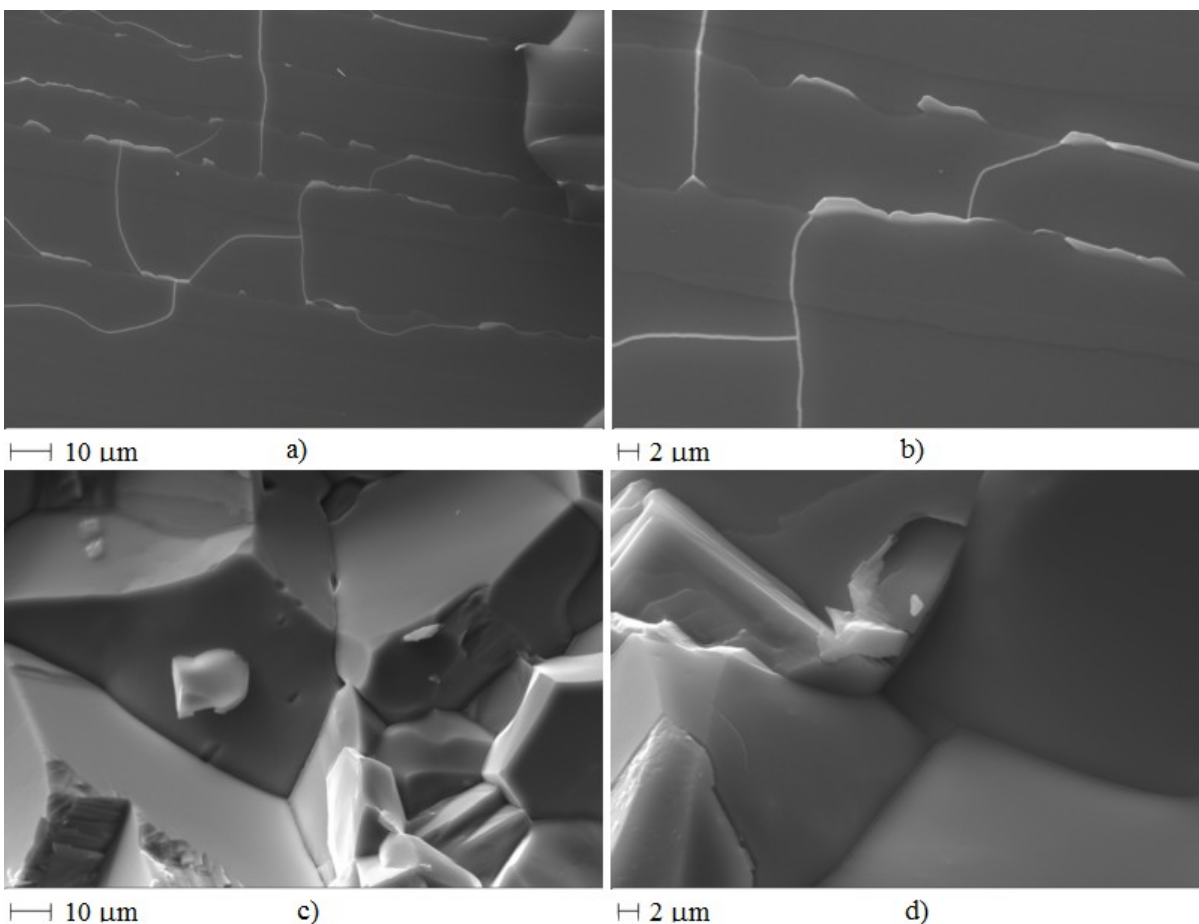
**Figure 4-3 Scanning electron micrographs on cold compressed NaCl. a) Original reagent grade NaCl crystals used to make the samples. b) Porous NaCl sample cold compressed at 55 MPa. Porosity indicated by undrained Hg and by open pores as designated by white arrow.**

Fig. 4-4 demonstrates the dielectric permittivity of NaCl and KCl for both the single crystals and for those cold compressed samples made under a confining pressure of 275 MPa.

Both single crystals and the cold compressed samples give similar results indicating that cold compression technique worked well for these two samples. SEM images of sylvite crystal and compressed KCl are shown in Fig. 4-5 where (a, b) are SEM for single sylvite crystal and (c, d) are SEM of compressed KCl. We broke a small piece from the single sylvite crystal and tried to compare that with the cold compressed synthetic KCl sample which gave us almost the same dielectric value of single crystal. From the SEM images, we can say that the compressed sample is comparable to the single crystal as it doesn't show any visible porosity and the dielectric values are almost same. So we can use 275 MPa as an ideal pressure limit where it is possible to get pore free sample at least for NaCl and KCl. These results suggest that the cold compression technique provides acceptably pore free KCl and NaCl polycrystals.



**Figure 4-4 Dielectric permittivity of a) cold compressed KCl and single sylvite (KCl) crystal; b) cold compressed NaCl and single halite (NaCl) crystal. Cold compressed samples showed similar permittivity values as single crystal.**



**Figure 4-5 Scanning electron microscopy (SEM) of (a-b) single sylvite crystal; (c-d) cold compressed KCl.**

#### 4.4 Salt With Glass Beads

One problem of using KCl-NaCl mixtures is that there is not a great contrast in the dielectric permittivity between the two salts. This makes it difficult later to assess the validity of the mixing laws. In an attempt to overcome this difficulty, samples were prepared by mixing glass beads with NaCl and KCl. Glass was selected because its dielectric permittivity differs from that for the salts and because it does not react chemically with them. We prepared a number of mixtures of glass beads and salts in order to make samples by cold compression. From Table 4-3 it is found that pure NaCl sample has higher dielectric permittivity and it is decreasing with the addition of glass beads. The same trend is found for KCl and glass beads mixtures. If we look



at the dielectric values in Table 4-3 we can see that glass beads mixed with KCl samples are less porous than glass beads mixed with NaCl. Though we did not measure the porosity for these samples, still we can say that because the dielectric values of NaCl, KCl and glass beads are 5.9, 4.8 and 4 respectively. Therefore, the glass beads mixed with NaCl samples should have dielectric permittivity in between 5.9 and 4 but the dielectric values are far below 5.9 and 4 with the increase of glass beads percentage. On the other hand, the dielectric permittivity of glass beads mixed with KCl samples are between 4.8 and 3.9, which means these samples are less porous than the NaCl one. Therefore, KCl sticks together with glass beads better than NaCl.

**Table 4-3 Dielectric permittivity of glass beads mixed with KCl and NaCl according to mass percentage.**

Sample	Glass beads mixed with NaCl			Glass beads mixed with KCl		
	Glass beads volume %	NaCl Volume %	Permittivity	Glass beads volume %	KCl volume %	Permittivity
<b>1</b>	4.50	95.50	4.93	4.08	95.92	4.66
<b>2</b>	8.98	91.02	3.83	8.25	91.75	4.62
<b>3</b>	27.50	72.50	2.89	26.10	73.90	4.59
<b>4</b>	37.17	62.83	2.72	35.06	64.94	3.90

We hoped that we might be able to form nearly pore free samples in this manner, but it was not possible. Fig. 4-6 shows the SEM on NaCl and glass beads mixture sample. The highly nonconductive glass shows as dark gray spheres in the images. Molds of the plucked glass beads show how the NaCl crystals deformed between the stronger glass beads. The image further suggests that it was not possible to remove all of the porosity in these materials.



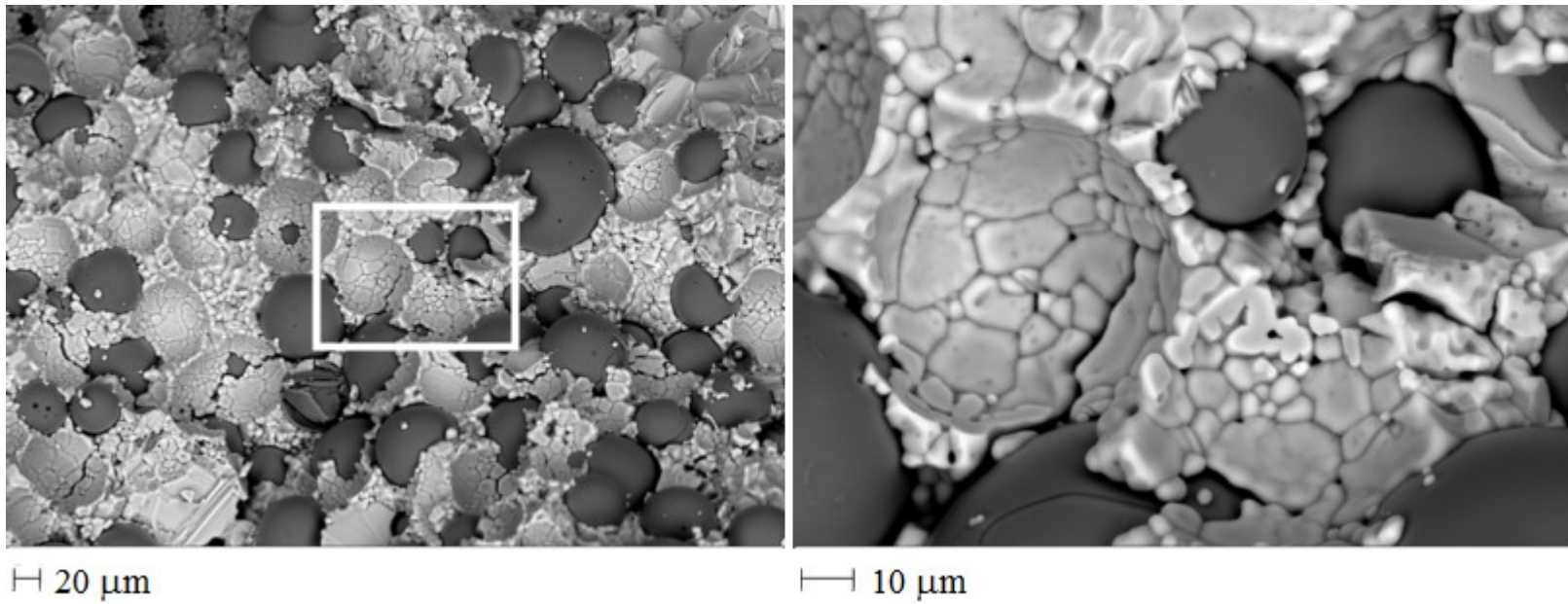


**Figure 4-6 Scanning Electron microscopy on glass beads mixed with NaCl sample.  
Glass beads are not homogeneous with NaCl. So it created more porosity in the sample than expectation.**

## 4.5 Mixing Model

As noted in earlier chapters there are numerous different effective media theories that attempt to describe the dielectric permittivity of mixtures. Here we compare our laboratory observations to nine different rules that are prominent in the literature and that had been described earlier in Chapter 2. The differences in the calculated permittivity for three scenarios are explained. In the first case, mixing model is concerned to the lower permittivity of the inclusion compared to the matrix which corresponds to the dry porous rock, that is, pore filled with air. Secondly, the permittivity of the inclusion is much higher than that of the matrix and corresponds to pore filled with water. In the third case, there is no significant contrast between inclusion and the matrix, and represent a formation like potash which is primarily a mixture of halite and sylvite. The first two cases are important to calculate the real permittivity from its powder as well as to estimate water content based on mineral real permittivity of the formation.

### 4.5.1 *Inclusion of lower permittivity than the matrix*

It is well known that the dielectric permittivity measurements on solids using capacitance methods have some difficulties. For example, it is tedious to fit the solid samples between the two electrodes of the capacitor. However, powders of the solid samples are convenient to use instead. The permittivity of the solid material then can be obtained by considering the powder as a two component mixture where the inclusion is air having a dielectric permittivity of 1. One of the earliest measurements on rock powder were performed by Olhoeft et al. [1981] at a frequency range 100 Hz to 1 MHz and the data were fitted to a formula that was derived from the Lichtenecker equation [Olhoeft and Strangway, 1975]. Previous work [S. O. Nelson, 2005] used six dielectric mixing equations and concluded that the Landau, Lifshitz, Looyenga (LLL)

gave the best fit for his results. It is difficult to determine the appropriate formulae that best describe the behavior of an air filled porous material because the difference of dielectric permittivities obtained from these different mixing theories can be smaller than the uncertainty of the measurements. Fig. 4-7 shows the effective permittivity for a hypothetical air-filled porous NaCl with increasing amounts of pore space calculated using the different theories. For air we have assumed a permittivity of 1 while for NaCl the permittivity value used was 5.96. The fractional pore volume is the same as the porosity and hence the plot ranges from the pure pore free solid to complete air. In practice, it would be difficult to actually create an appropriate 'mixture' of most crystals at porosities above 50% but the calculations are carried to extremes for the sake of illustration. This model clearly shows the following:

- Weiner<sup>+</sup> and Weiner<sup>-</sup> formulae give respectively the upper bound and the lower bounds of the permittivity values calculated using the nine theories. This is as expected as Weiner's bounds equate simply to calculations of the capacitance in either series or parallel.
- The permittivity values obtained from the equations of Hashin-Strickmann (HS<sup>-</sup>) and Sen are similar.
- Maxwell-Garnett and HS<sup>+</sup> give exactly same values of permittivity.
- There is a difference of less than 10% between the values predicted by six theories for porosities less than 15%. These are Maxwell-Garnett, Bruggemann, Complex Refractive Index, Lichtenecker, LLL, Sen and HS<sup>+</sup> formulae. CRIM and Sen showed less than 1% variation. Moreover, Maxwell-Garnett and Lichtenecker showed similar permittivity at porosities less than 15%.

- $Weiner^+$  provides overestimated permittivity values compared to other theories and increases linearly with the increase of porosity while  $Weiner^-$  provides underestimated permittivity which increases nonlinearly with the increase on porosity. This is not surprising as the Weiner model are expected to provide the upper and lower bounds.
- Higher variations in permittivity are found among the models for porosity of 60-80%.
- If the porosity exceeds 40% then the difference between the values predicted by different models might exceed up to 14% for those six theories.

A computer program used to calculate these different effective permittivities is provided in Appendix B.

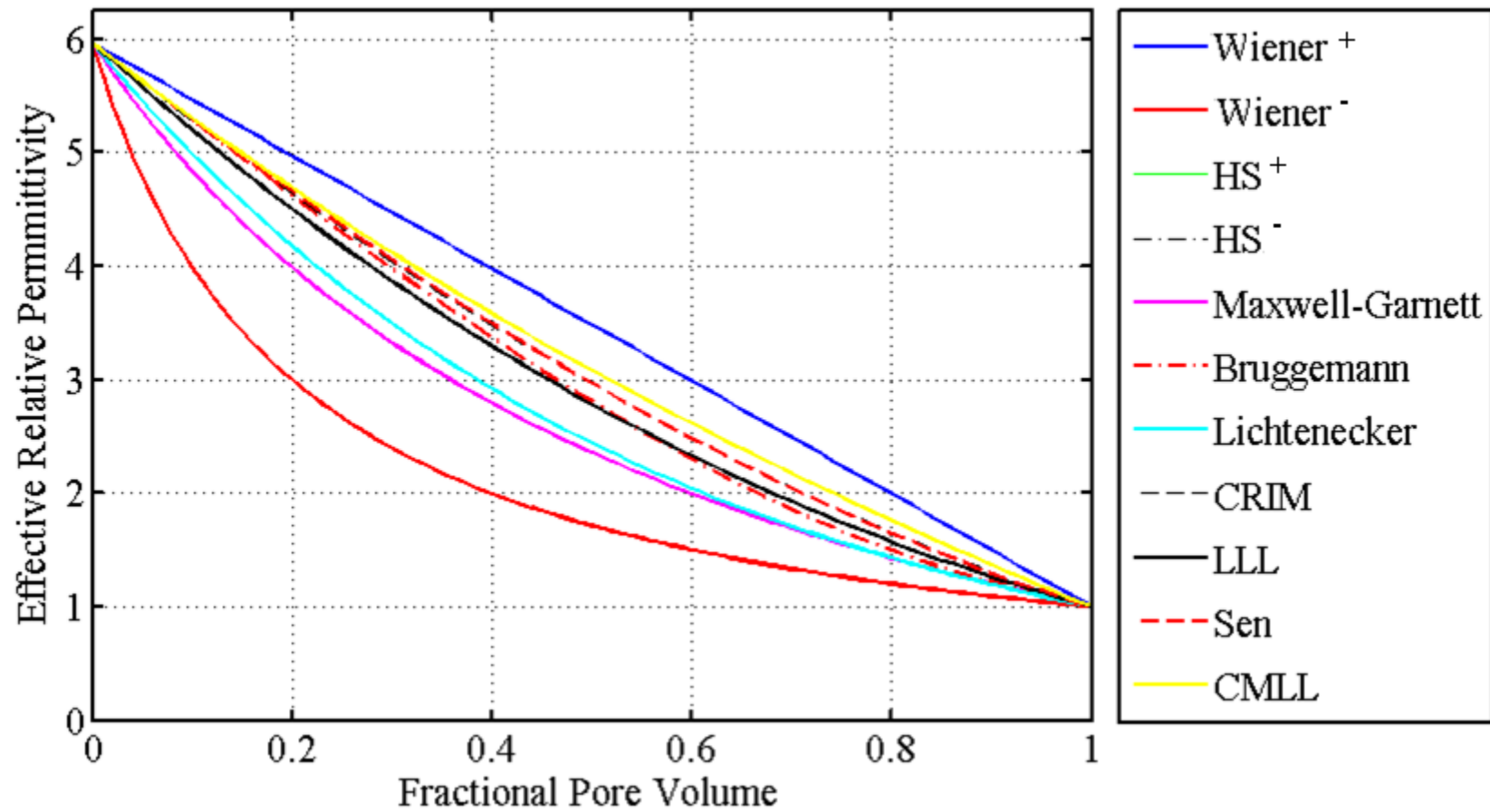


Figure 4-7 Calculated permittivities of the dry porous NaCl as a fraction of air filled pore volume between 0 to 1. Superscripts + and - are upper and lower bounds.

#### 4.5.2 Inclusion of higher permittivity than the matrix

Water saturated rock is an example in which the permittivity of the inclusion is much greater than the matrix. The permittivity of the water is  $\sim 80$  at the frequencies studied and this is at least 10 times larger than many of the rock forming minerals. This huge contrast is exploited in geosciences in estimating water content by probing the formation with electromagnetic radiation at frequencies that range between few MHz to approximately 1 GHz. These methods include Ground Penetrating Radar [*al Hagrey and Muller, 2000*], Time Domain Reflectometry [*Dalton et al., 1984; Dalton and Vangenuchten, 1986*] and Dielectric logging [*Pascal et al., 1981*]. In these methods the observed travel time is converted into velocity from which the dielectric permittivity is calculated. In many cases and in particular in the near surface of the earth the empirical equation developed by Topp *et al.* [1980]. They found that the dielectric constant was varied with the volumetric water content while almost invariant to the soil density, texture and salt content. Moreover, due to the change in volumetric water content of 0 to 0.55 in minerals soils causes the variation in dielectric constant from 3 to 40 [*Topp et al., 1980*].

Otherwise, the calculation is done assuming that (at high frequencies) the permittivity of both of the solid material and that of the fluid are known, so the water volume can be estimated accurately by applying a mixing model. Improvement of the accuracy of water estimation has been proposed by assuming that the rock water system is a three component mixture: solid matrix, free water and bound water. The latter is supposed to have a much lower permittivity of free water because of the restriction of the water molecule motion due to the surface forces. Determination of the bound water volume remains unclear because the best prediction was that something between one and 3 monolayers of water molecules [*Or and Wraith, 1999*].

In this study we calculated the effective permittivity of the simplest case ignoring these surface forces and assuming that all the water present in the system is free (which is not true in most cases especially clayey soils). We carried out these calculations using NaCl and water at a frequency of 10 MHz to 3 GHz for contrast with Fig. 4.7, obviously once we mix NaCl and water in reality the NaCl would dissolve and so these calculations are only for the sake of illustration. Figure 4.8 shows the calculated permittivity using these models. The following points summarized the results:

- $Weiner^+$  and  $Weiner^-$  formulae give the upper bound and the lower bound respectively of the permittivity values calculated using the nine theories.
- Maxwell-Garnett and  $HS^+$  give exactly same dielectric values.
- CMLL and  $HS^-$  provide exactly same result.
- 2-6% variations in permittivity were found for Bruggemann,  $HS^+$ , Lichtenecker and Maxwell-Garnett when porosity is less than 15%. However, variations are 13-20% for CRIM and Sen theories compared to LLL at porosity of 15%.
- Maximum variations in permittivity between  $Weiner^+$  and  $Weiner^-$  were observed at porosity of 76%.

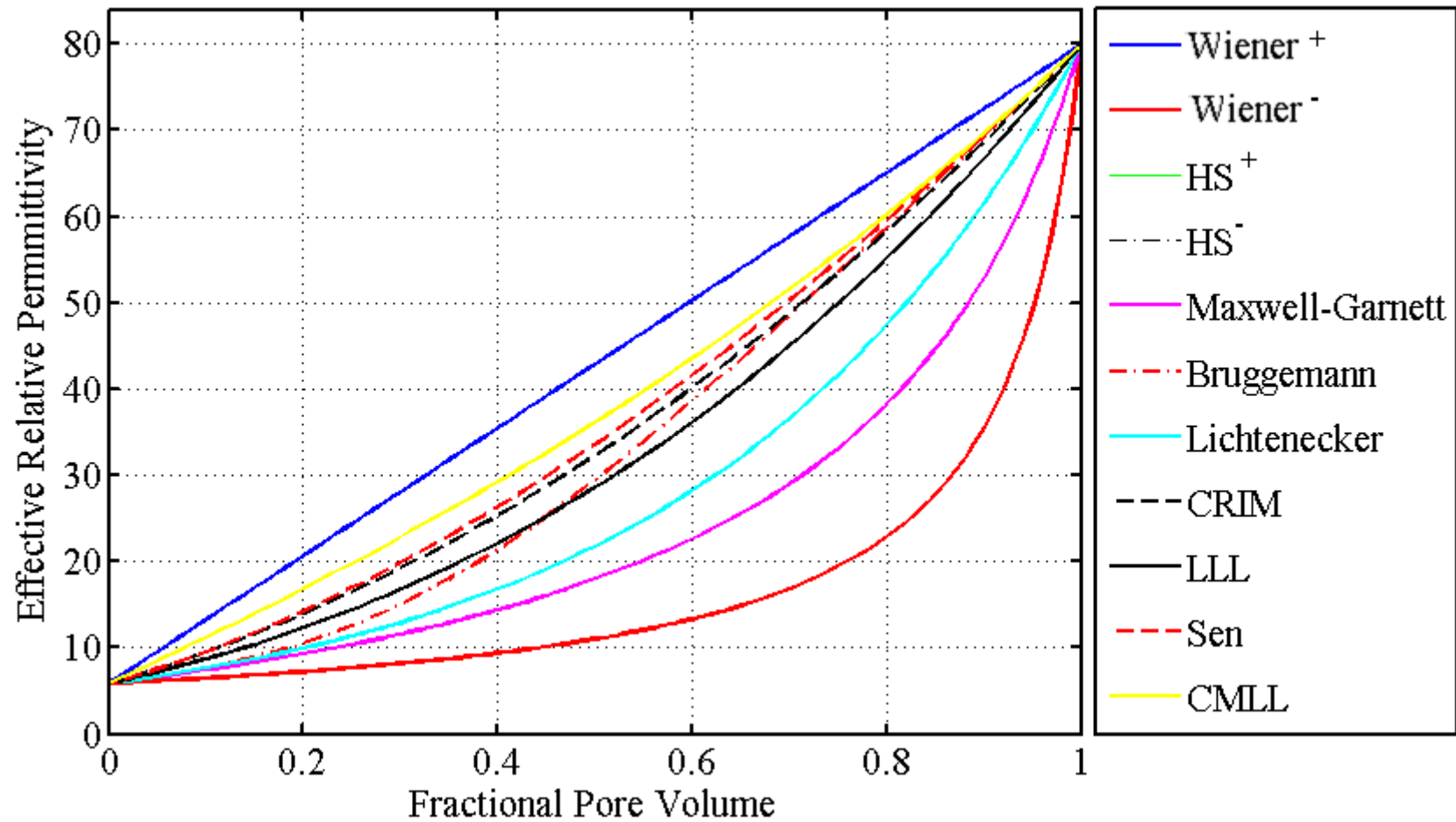


Figure 4-8 Calculated permittivity of the water saturated NaCl at fraction pore volume between 0 to 1. Permittivities were calculated from nine mixing theories.



#### ***4.5.3 Inclusion of permittivity comparable to the matrix***

In the context of potash deposits that are usually of low porosity and do not contain substantial water, the main constituents are primarily NaCl and KCl with similar permittivities of 5.9 and 4.85, respectively. The permittivity calculated by the nine theories for this type of mixture is very similar. In Fig. 4-9 the permittivity values of halite-sylvite mixture are shown for different fractional pore volumes. The nine theory lines are difficult to distinguish from each other implying a very minute difference. A maximum 1% variation in the permittivity values were found between even the Weiner<sup>+</sup> and Weiner<sup>-</sup> at equal volume fractions of 50%.

Examination of Fig. 4-9 suggests that for practical purposes the dielectric permittivity of a pure KCl-NaCl mixture could be described by a nearly linear function. This simplicity may actually provide a methodology for assessing the quality of the potash ores quickly by measuring the dielectric properties. That is, the lower the value of the dielectric permittivity the richer the proportion of KCl.

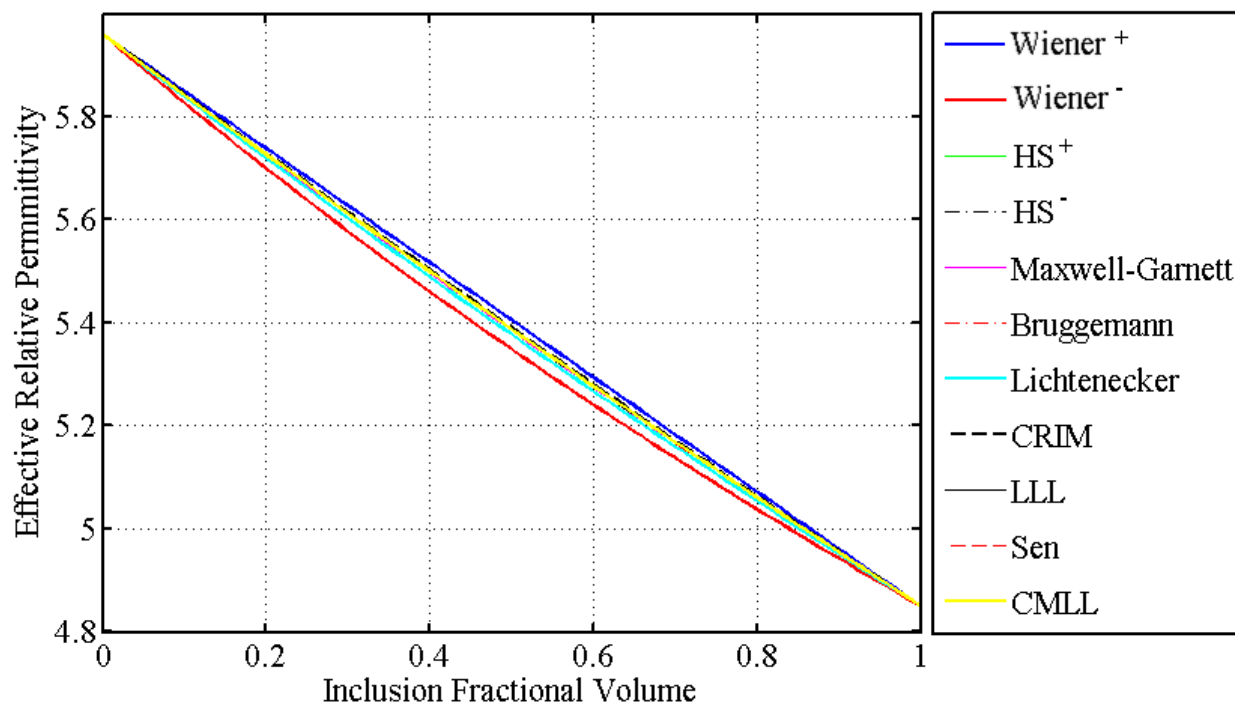


**Figure 4-9 Calculated permittivity of Halite-Sylvite mixtures versus fraction volume of sylvite. A comparison of our measurement value with theoretical model**

#### 4.5.4 Comparison of porous salts with theory

Measurements were done on a series of porous NaCl and KCl samples. These samples were all formed using the cold compression technique as described earlier. We have applied different pressures on the samples to get different porosities. A less expensive alternative method was used to determine the porosity of these samples relative to the initial test pieces described in earlier in Section 4.3. Porosity was calculated for all of the samples using the He pycnometer (see Section 3.9). To measure porosity in this way one must obtain measures of the sample's bulk  $V_b$  and solid  $V_g$  volumes. Again, the porosity,  $\varphi = \frac{[V_b - V_g]}{V_b}$ . As described in Chapter 3,  $V_g$  is obtained directly from the He pycnometer. Obtaining  $V_b$ , however, is usually problematic in even the best situations. This is normally accomplished by measuring the length and diameter of a

cylindrical sample. Carrying this out on even well machined cylinders, however, allows for accumulation of the uncertainties as errors are propagated. Our cold compressed samples, however, were not perfect cylinders and another approach was necessary for finding the bulk volume.

The approach began by vacuum-sealing sealing the samples with plastic film. Then the sealed sample was reinserted to the He pycnometer and its volume  $V_S$  measured. Next, the sample was removed from the pycnometer and extracted from the plastic film whose volume  $V_F$  was then determined again in the pycnometer. The bulk volume is simply then  $V_b = V_S - V_F$  which once obtained allowed for ready calculation of  $\phi$ . This approach could be readily adapted to more standard Archimedean techniques that rely on immersion of samples into liquids of known density. Such techniques are often problematic for determining the density of porous media.

Table (4-4) gives the dielectric permittivity with uncertainties, the calculated porosity and their uncertainties, and the grain and bulk volumes for the porous NaCl and KCl samples. In Fig. 4-10 the black circles with error bars are our measurement values of eight porous NaCl samples. In Fig. 4-11 the black circles with error bars represent the experimental measurement values for the porous KCl sample. Table (4-5, 4-6) report the relative percent change between the experiments and theories for NaCl and KCl respectively. The following formula was used to calculate the percent change

$$\text{Relative \% change} = \frac{(\text{Experimntal value} - \text{model value})}{\text{Experimntal value}} \times 100\% \quad \text{Eq. ( 4-2)}$$

From the Figs. (4-10,4-11) and Tables (4-5,4-6) it is apparent that none of the theories not match the experimental results perfectly for both the NaCl and KCl samples. This is likely a combination of deficiencies in the experimental approach and because none of the mixing

models truly accounts for microscopic structure of these materials. Variance and standard deviation of the mixing theories with the experimental results are also provided in the Tables (4-10, 4-11). If we accept that the ‘best’ model will have the lowest standard deviation, then for both cases it appears that the Hashin-Shtrickman and Sen models best describe the data.

**Table 4-4 Dielectric permittivity, porosity, grain volume and bulk volume of NaCl and KCl samples. Both the grain volume and bulk volume were calculated using He pycnometer.**

<b>sample</b>	<b>Permittivity</b>	<b>Porosity (%)</b>	<b>grain volume(cm<sup>3</sup>)</b>	<b>Bulk volume(cm<sup>3</sup>)</b>
<b>NaCl1</b>	5.38±0.12	2.99±0.08	10.130	10.441
<b>NaCl2</b>	5.23±0.04	7.52±0.09	7.348	7.946
<b>NaCl3</b>	5.85±0.06	1.71±0.20	5.893	5.995
<b>NaCl4</b>	5.4±0.03	5.08±0.09	8.373	8.822
<b>NaCl5</b>	5.64±0.04	3.47±0.11	6.450	6.682
<b>NaCl6</b>	5.70±0.09	2.09±0.06	11.835	12.088
<b>NaCl7</b>	5.31±0.04	4.12±0.14	4.018	4.191
<b>NaCl8</b>	5.52±0.09	3.11±0.11	8.262	8.527
<b>KCl1</b>	4.53±0.02	3.06±0.10	10.508	10.840
<b>KCl2</b>	4.48±0.05	4.02±0.09	9.691	10.096
<b>KCl3</b>	4.50±0.05	3.56±0.10	11.478	11.901
<b>KCl4</b>	4.51±0.04	5.12±0.19	7.544	7.951
<b>KCl5</b>	4.53±0.04	5.25±0.16	7.079	7.471
<b>KCl6</b>	4.21±0.07	6.80±0.14	5.456	5.854
<b>KCl7</b>	4.78±0.06	1.42±0.49	6.229	6.319
<b>KCl8</b>	3.99±0.05	8.04±0.27	2.611	2.839

**Note: Data are reported as mean ± standard deviation.**

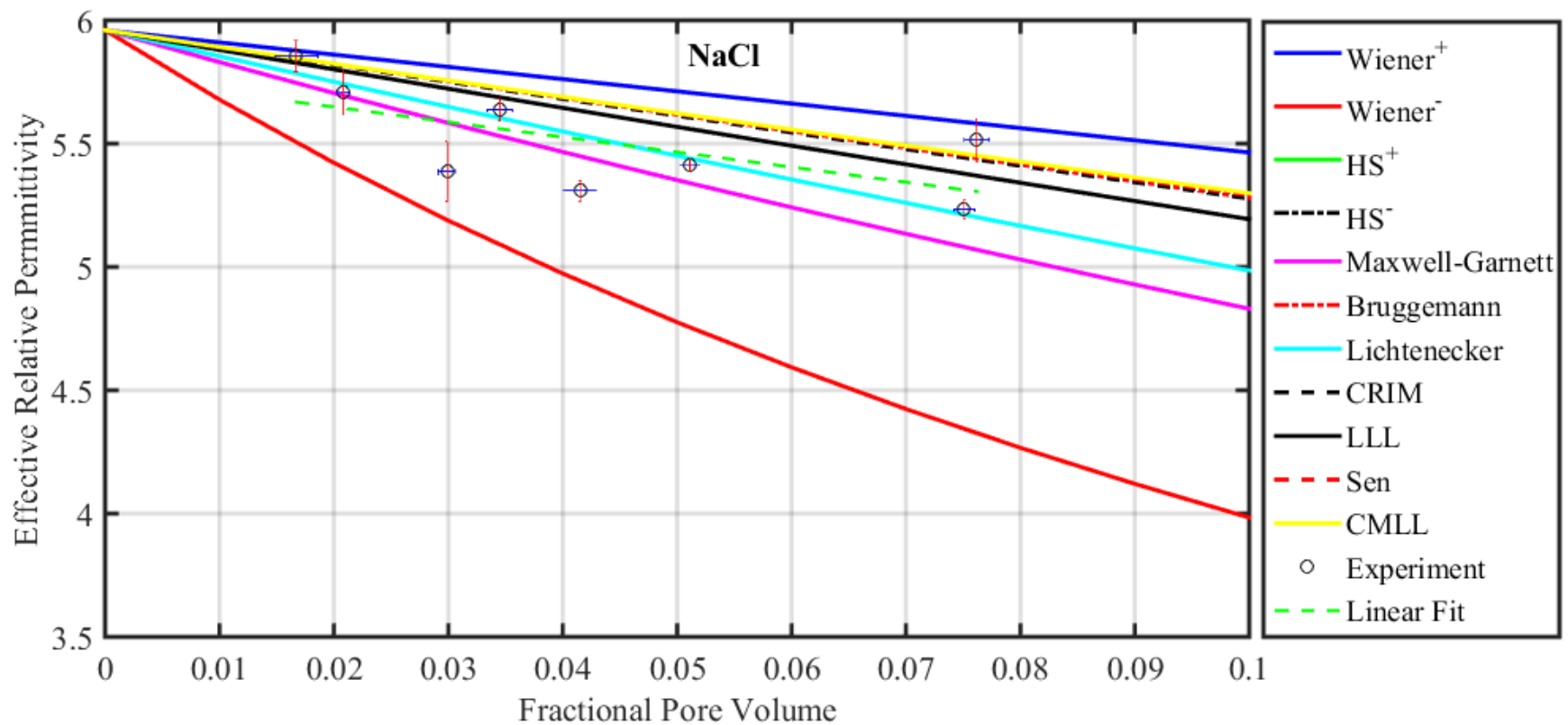


**Figure 4-10: Dielectric permittivity of porous NaCl versus fractional pore volume plots using mixing models and experiments. The black circles with error bars represent experimental values for the eight porous NaCl samples, and the green dashed line is the linear fit.**

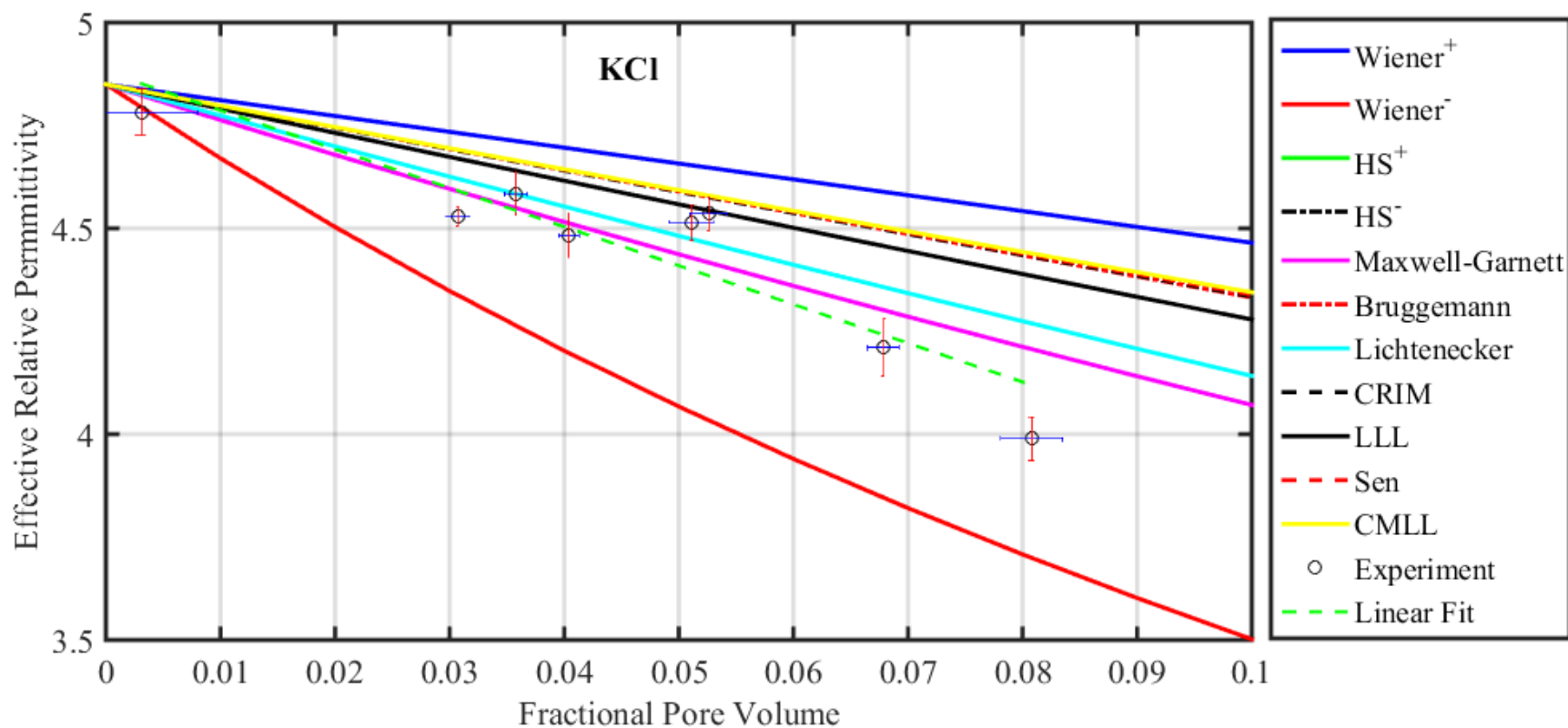


**Figure 4-11: Dielectric permittivity of porous KCl versus fractional pore volume plots using mixing models and experiments. The black circles with error bars represent the experimental values for the eight porous KCl samples, and the green dashed line is the linear fit.**

**Table 4-5: Relative percentage change between the experimental results and mixing theories for NaCl samples. Variance and standard deviation is also shown. Experimental values are taken as reference.**

<b>Relative % change (NaCl)</b>											
<b>Sample #</b>	<b>Wiener1</b>	<b>Wiener2</b>	<b>HS1</b>	<b>HS2</b>	<b>MaxGar</b>	<b>Bruggeman</b>	<b>Lichteneker</b>	<b>CRIM</b>	<b>LLL</b>	<b>Sen</b>	<b>CMLL</b>
<b>1</b>	7.290	3.809	3.527	6.411	3.527	6.382	4.641	6.319	5.861	6.397	6.411
<b>2</b>	6.326	20.530	3.015	4.120	3.015	3.932	0.417	3.843	2.675	4.029	4.120
<b>3</b>	0.377	6.375	1.894	0.152	1.894	0.161	1.210	0.204	0.478	0.156	0.152
<b>4</b>	5.179	13.799	1.331	3.650	1.331	3.563	0.540	3.475	2.672	3.607	3.650
<b>5</b>	2.606	10.784	1.944	1.541	1.944	1.501	0.606	1.428	0.872	1.521	1.541
<b>6</b>	2.558	5.633	0.204	1.913	0.204	1.899	0.622	1.849	1.514	1.906	1.913
<b>7</b>	7.718	7.433	2.549	6.507	2.549	6.452	4.055	6.374	5.740	6.480	6.507
<b>8</b>	1.201	27.506	8.790	1.158	8.790	1.364	6.016	1.456	2.706	1.258	1.158
<b>Variance and standard deviation (SD)</b>											
<b>Variance</b>	0.014	0.057	0.032	0.018	0.032	0.019	0.027	0.019	0.021	0.019	0.018
<b>SD</b>	0.117	0.238	0.179	0.136	0.179	0.137	0.165	0.138	0.146	0.136	0.136

**Table 4-6 Relative percentage change between the experimental results and mixing theories for KCl samples. Variance and standard deviation is also shown. Experimental values are taken as reference.**

<b>Relative % change (KCl)</b>											
<b>Sample #</b>	<b>Wiener1</b>	<b>Wiener2</b>	<b>HS1</b>	<b>HS2</b>	<b>Maxgar</b>	<b>Bruggeman</b>	<b>Lichteneker</b>	<b>CRIM</b>	<b>LLL</b>	<b>Sen</b>	<b>CMLL</b>
<b>1</b>	4.264	4.442	1.315	3.432	1.314	3.407	1.958	3.386	2.987	3.420	3.432
<b>2</b>	4.504	6.810	0.651	3.415	0.650	3.370	1.478	3.350	2.826	3.393	3.415
<b>3</b>	2.698	7.566	0.788	1.714	0.788	1.678	0.033	1.657	1.184	1.696	1.714
<b>4</b>	2.971	11.407	1.954	1.576	1.954	1.503	0.915	1.487	0.814	1.540	1.576
<b>5</b>	2.398	12.465	2.697	0.955	2.697	0.877	1.625	0.862	0.165	0.917	0.955
<b>6</b>	8.228	9.522	2.091	6.484	2.091	6.362	3.349	6.361	5.515	6.425	6.484
<b>7</b>	1.158	0.225	0.847	1.071	0.847	1.071	0.918	1.067	1.025	1.071	1.071
<b>8</b>	12.115	7.833	5.169	10.136	5.169	9.969	6.560	9.986	9.023	10.055	10.136
<b>Variance and standard deviation (SD)</b>											
<b>Variance</b>	0.018	0.064	0.037	0.024	0.037	0.024	0.033	0.024	0.027	0.024	0.024
<b>SD</b>	0.134	0.252	0.191	0.154	0.191	0.156	0.182	0.155	0.164	0.155	0.154



## 4.6 Summary

In this chapter we have carried out dielectric measurements on single crystal of the evaporate minerals and on cold compressed synthetic samples. At first dielectric measurements on single crystals were done. Due to birefringence effect we did not work a lot on crystals. Later on we used cold compressed technique to prepare samples from different mineral powder. Moreover, different mixing theories were used to create a theoretical model. We have shown this theoretical model for three scenarios: 1) Inclusion of lower permittivity than the matrix, 2) Inclusion of higher permittivity than the matrix and 3) Inclusion of permittivity comparable to the matrix. Further a series of eight porous NaCl and KCl samples were prepared and their measurement values were compared to the different mixing theories. The Hashin-Shtrikman upper bound, which has the same value numerically as the Sen *et al.* [1980] model appear to describe these data best.

# CHAPTER 5. APPLICATION TO ROCK CORES

## 5.1 Introduction

A main goal of this thesis is to examine in detail the conditions under which reflections are produced in ground penetrating radar images acquired in potash mines. In this chapter we have presented an overview about the Potash formation and measurements on samples taken from core obtained during planning of the Rocanville, SK potash mine. We first review the geology of the potash formation including the stratigraphy in the area, the formation of the potash deposits, and the mineralogy of potash formation. The focus then shifts to measurements carried out on the core materials. We discuss the first attempts to make measurements directly on the split core sample, measurements that were not successful and motivated the development of the cold compression technique to create reconstituted samples. We have prepared eight cold compressed samples from eight different depths along the core. Dielectric permittivity measurements as well as different mineralogical analysis such as XRD, XRF and SEM were also carried out on these samples. At the end of this chapter we have calculated the reflection coefficients for those eight depth ranges and we have created a synthetic GPR trace.

## 5.2 Background

The Saskatchewan potash deposits lie within the Prairie Evaporite Unit [*Milner and Dunn, 2004*] of the vast Elk Point Basin Group, which contains the bulk of the salt deposits within the Western Canada Sedimentary Basin [*Grobe, 2002*]. The Elk Point Group basin (Fig.

5-1) is large and stretches from Montana and North Dakota across western Manitoba, and nearly all of Saskatchewan and Alberta ending in the Yukon and N.W.T. [Holter, 1969]. The Elk Point Group consists of a number of formations that vary regionally but were precipitated or deposited during the Early through the Middle Subdivisions of the Devonian Period from about 420 Mya to 385 Mya. The deposits are primarily carbonates, anhydrites, dolostones, and salts laid down in horizontal beds in restricted shallow seas. The main focus of this study is on the Prairie Evaporite formation which is a major unit of the Elk Point Group. It is particularly interesting as it is primarily composed of halite, sylvite, and carnallite with some thin seams of dolomitic mudstone [Mossman *et al.*, 1982] as well as anhydrites. The thin seams of dolomitic mudstone are the same as the 'shale' layers that are the targets of the GPR studies. Its maximum thickness is about 218 m. Although the Prairie Evaporite extends from northern Alberta through Saskatchewan to North Dakota and Montana, the economically important KCl rich area (Fig. 5.1) primarily lies under Saskatchewan and this resource has generated a large industry in that Province.

The mineralogy, stratigraphy and structure of potash deposit of Saskatchewan is relatively simple. The potash deposit consists of mainly halite (NaCl) with two potassium chloride minerals of sylvite (KCl) and carnallite ( $\text{KCl} \cdot \text{MgCl}_2 \cdot 6\text{H}_2\text{O}$ ). The KCl is the actual material that is sought during mining. The Carnallite is problematic for both mining and processing. Therefore, it is to be avoided as much as possible during mining operation. The deposits also include some insoluble minerals such as anhydrite and lesser amounts of quartz, dolomite and clays. The potash ores also contain trace amounts of hematite that do not appear to be important in terms of the overall physical properties but which do give the potash its characteristic pink color.

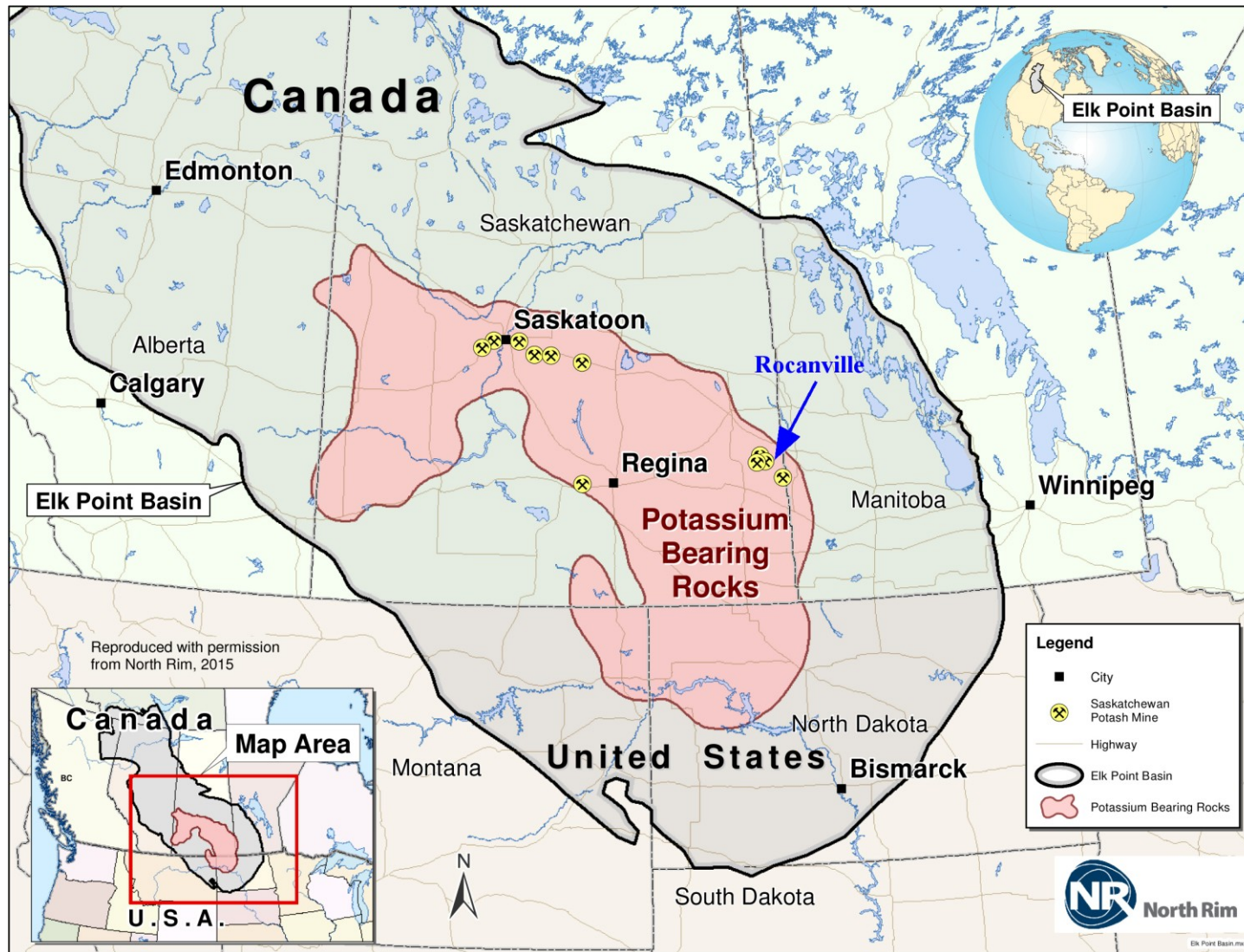
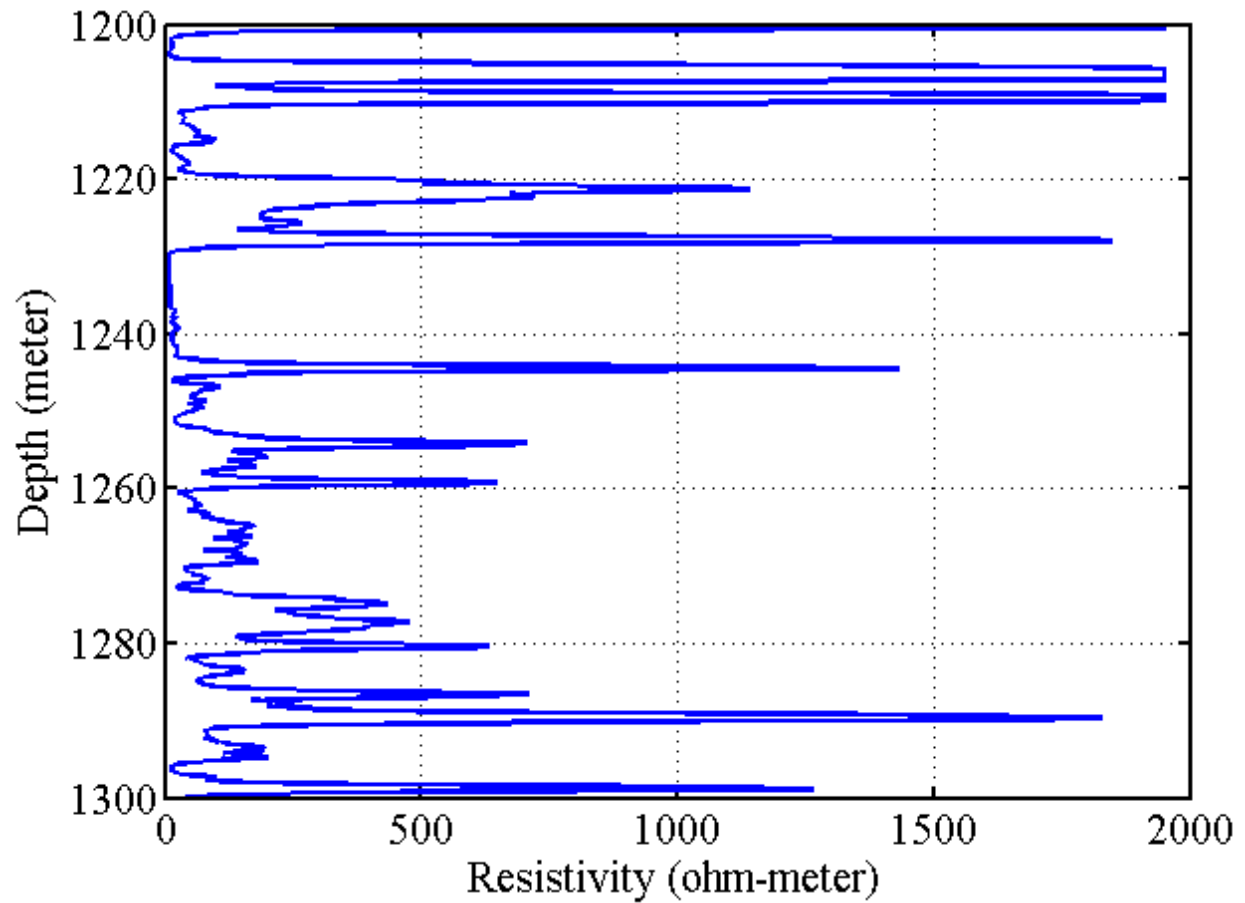


Figure 5-1: Potash mining belt (Reproduced with permission from NorthRim)

### ***5.2.1 Geology and Geophysical Logs at Rocanville***

The Rocanville potash mine is situated on south-east Saskatchewan about 16 km north of Rocanville and about 200 km east of Regina. According to Rocanville lithology this potash mine is mainly composed of halite with a variable amount of sylvite, carnallite and clay minerals. At the depth of around 960 meter the main ore zones can be found. According to Potash Corporation of Saskatchewan, the reserve of Rocanville has about 372 metric tons of 22.5%  $K_2O$  which is sufficient to support production for next 59 years.

Fig. 5-2 shows the resistivity values for the depth range 1200 to 1300 meter in Rocanville potash mine. We have used this resistivity values later on in this section.



**Figure 5-2 Resistivity of different depths in Rocanville Potash mine**

### **5.3 Core Materials Studied**

An extensive collection of core was obtained during the drilling of the PCS Rocanville 13-09-16-33W. In this section we provide the results of the measurements of the dielectric permittivity on the two suites of reconstituted core samples. The first ensemble consists of 14 pieces all extracted from a single short section of the rock core. The second one consists of eight samples from eight different depths. The measurement protocols are exactly the same as those already described in Chapter 4.

### ***5.3.1 Heterogeneity in a single sample***

In an attempt to better characterize the actual geological materials from a potash mine, a series of permittivity measurements on a rock core sample were carried out. The core was taken from (1238.68-1239.37) meter depths from a borehole drilled through the potash formation. The material provided is a ‘split’ core which is a half cylinder that is sawed from the original cylindrical core material. The dimensions of this core are 30 cm × 10 cm. As such there is a large flat region that allows easy access for the dielectric probe head. The sample was cut into 14 separate sections with a surface region of about 8 cm × 10 cm. Fig. 5-3 shows the piece of core that was cut into 14 pieces. Pieces are marked on the picture.



**Figure 5-3 A piece of core sample in the depth range of 1238.678-1239.37 meter**

Each of these pieces was placed directly on the sensor in order to make measurements and we have repeated same measurements three times and then the average of these three measurements were calculated. These directly measured dielectric values of the raw potash samples are shown in Fig. 5-4 and an image format of the same measurements are presented in Fig. 5-5(a) in order to emphasize the spatial variability while the corresponding values are reported in Table 5-1. Note that the values provided are the average permittivities over the frequency range 10 MHz to 3 GHz.

In an attempt to evaluate whether any Debye type mechanisms were active within these samples all of the data were plotted in an Argand  $\epsilon' - \epsilon''$  plot and shown in Appendix A where they were fit to a Cole-Cole circle. Most of the plots show tight clusters that are very poorly fit by a circle. This is because for those samples, there is little dispersion and low attenuation, and the scattering of the cluster essentially represents the noise of the measurements. This suggests that our frequency band is far from any appropriate Debye type resonance.

The directly measured permittivities range from 2.10 to 4.95. This scattering was not expected because this potash ore material is primarily composed of NaCl and KCl whose dielectric permittivities are 4.85 and 5.9 respectively, and the mixing theories and measurements on synthetic cold compressed samples of the previous chapter suggested that we should observe permittivities between these bounds. Although there are little amounts of other minerals within the material such as hematite that lies at grain boundaries and gives the potash its characteristic pink color. We believe these direct measurements failed for the following reasons:

- The spatial resolution of the measurement technique is only few millimeters and this is comparable to the individual dimensions of the crystals that make up the potash ore. As



such, the measurements cannot be expected to determine the effective properties of the core.

- The removal of the core samples from in situ pressures and the stress concentrations seen by the core as part of the drilling process tends to damage the material with the production of small cracks both within the grains and along grain boundaries. Even though these cracks are not visible to the eye, it is likely that they still can disrupt the flow of current between the probe's electrodes with the result that the apparent permittivity is significantly reduced relative to that which a propagating radar wave would see. These phenomena may also be related to the unsubstantiated observation of the mine geophysicist that old, and hence highly damaged, mine pillars do not provide good measures of radar wave speeds.
- The slabbing of the core was not done perfectly resulting in a surface that was not sufficiently flat for the measurements. Polishing of the surface did not improve the quality of the measurements, however.

**Table 5-1 Dielectric permittivity of different samples using raw potash measurement and cold compressed technique**

Sample	Dielectric permittivity	
	Raw potash measurement	Cold compressed potash
<b>1</b>	4.95±0.39	4.65±0.04
<b>2</b>	3.40±0.93	4.70±0.21
<b>3</b>	3.03±0.80	5.12±0.13
<b>4</b>	2.90±0.11	4.42±0.07
<b>5</b>	2.10±0.36	5.18±0.31
<b>6</b>	3.75±1.53	4.65±0.07
<b>7</b>	4.13±0.78	5.11±0.09
<b>8</b>	3.06±0.70	4.81±0.18
<b>9</b>	3.48±0.24	5.14±0.11
<b>10</b>	3.78±0.44	5.04±0.45
<b>11</b>	3.07±0.34	5.02±0.09
<b>12</b>	2.76±0.55	4.72±0.14
<b>13</b>	3.97±0.67	4.74±0.13
<b>14</b>	4.15±0.38	5.06±0.16

**Note: Data are reported as mean ± standard deviation.**

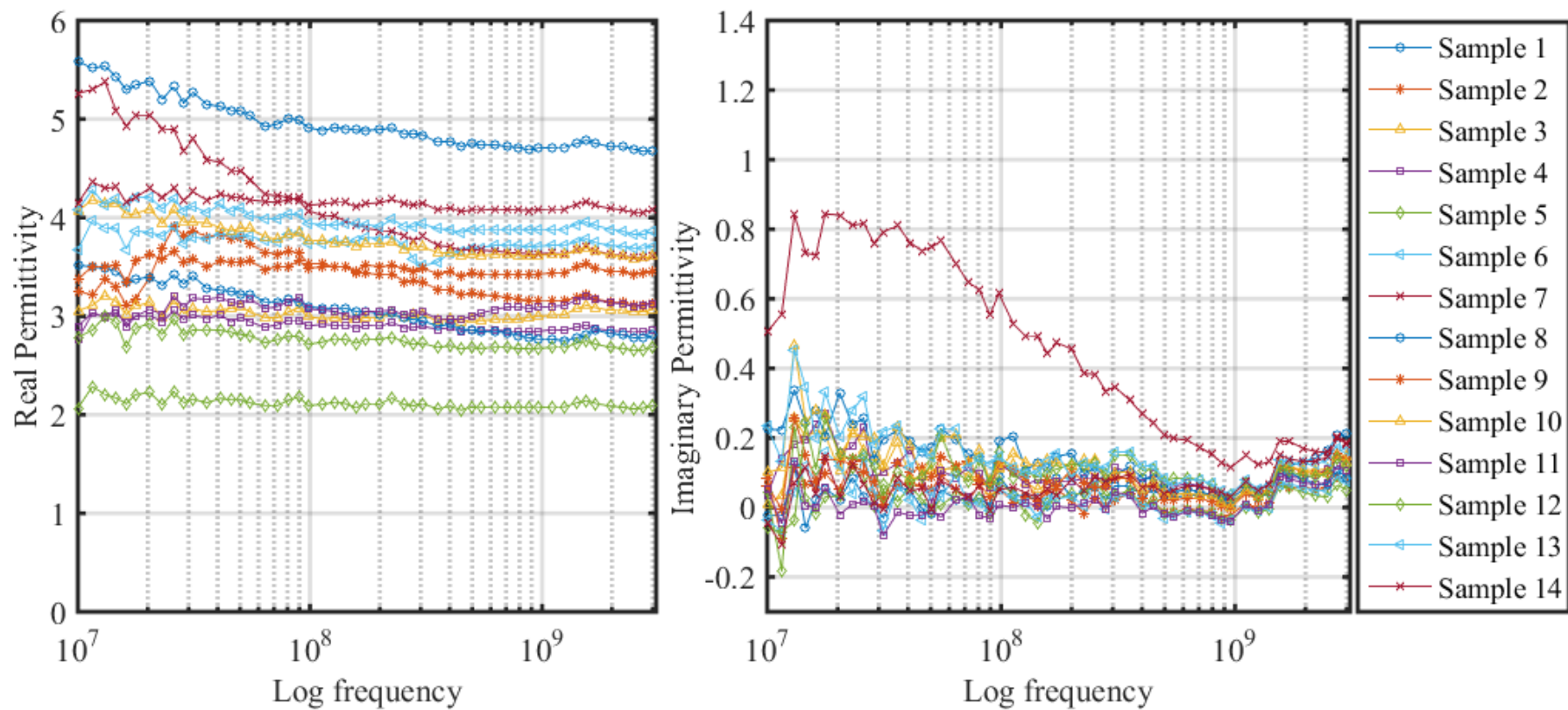


**Figure 5-4 Real and imaginary permittivity versus frequency for raw potash samples**

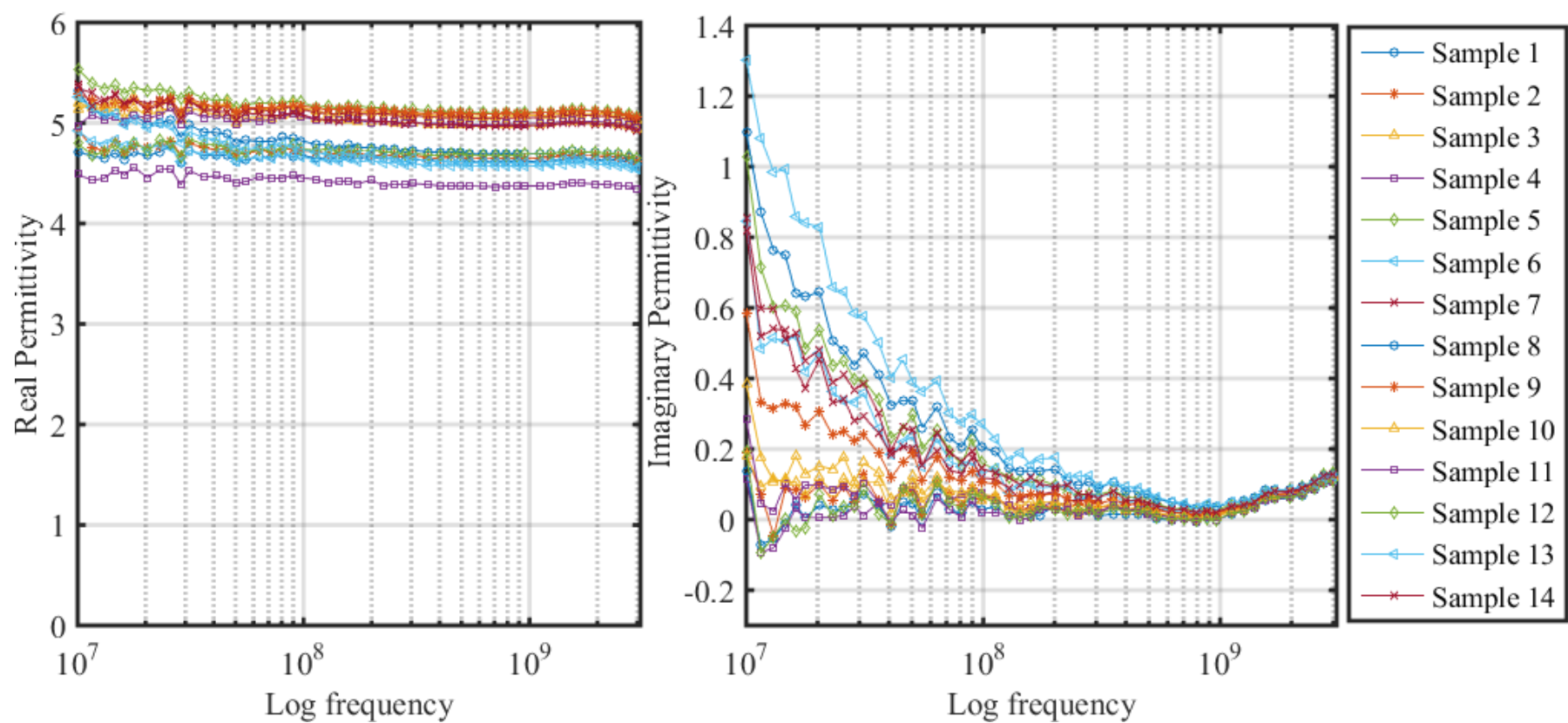


**Figure 5-5 Real and imaginary permittivity versus frequency for compressed potash samples**

These observations led us to the development of the cold compression technique that was tested in Chapter 4. The essential idea is that if we can make, at the scale that the probe requires, a homogeneous and nearly pore free material, then this material would be more amenable to providing a measure of the effective permittivity of the formation as a whole. Consequently, each of the 14 pieces was crushed and ground to a fine powder in the motorized mortar and pestle. These powders were then used to make cold compressed pellets that were ready for measurement. The applied pressures to make these samples were 250 MPa.

The real part of the dielectric values of these reconstituted samples ranges mostly between 4.5 to 5.2 shown in Fig. 5-5. These values are also provided in Table 5-1 and the dielectric values with their uncertainties are provided as an image in Fig. 5-5 (b,d) respectively. Cole-Cole plots for all of the samples are also given in Appendix A but, as with the samples from the single core these do not indicate that the measurements are near any Debye type resonance.

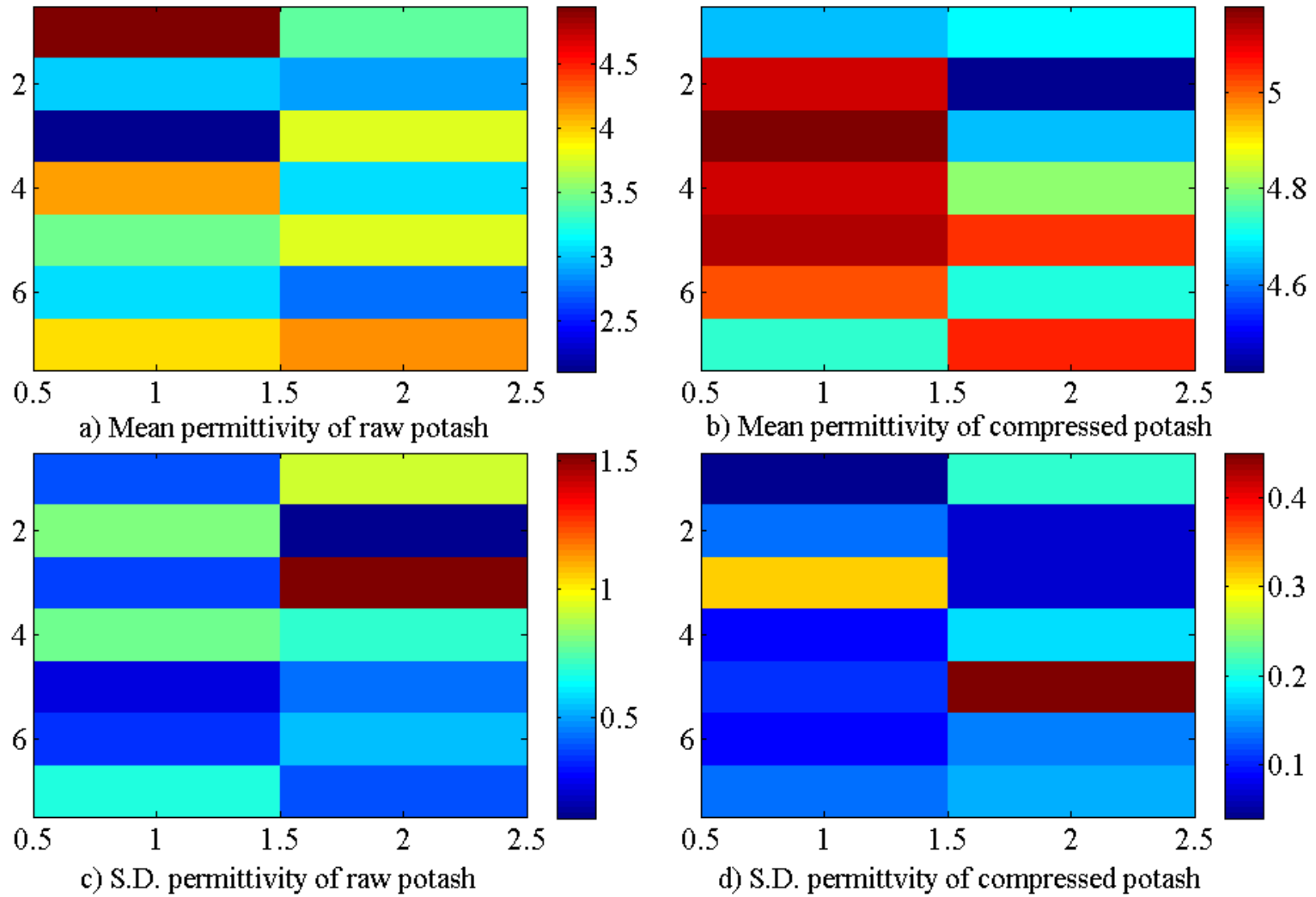


**Figure 5-6 (a) represents dielectric values placing each of the 14 pieces of the core directly on the sensor. The core was taken from depth (1238.68-1239.31 meter, (b). represents the dielectric values of 14 (compressed) samples. All the permittivity values were averaged out from four measurements. (c, d) represent the standard deviations (S.D.) of the permittivity in the raw and compressed samples respectively.**

### **5.3.2 Variations with depth**

Eight pieces of the core were selected from different depths of Rocanville potash mine. We cut a small piece from each depth range. The dimensions of these pieces were around 4 cm long. Then each of these small pieces was crushed into a powder and ground in the mortar/pestle. These powders were then cold compressed to make reconstituted pellets for measurement. From each set of powder one sample was prepared. Fig. 5-7 shows the reconstituted pellets.

#### **5.3.2.1 Variations in Permittivity with Depth on Reconstituted Samples**

The results in the last section highlighted the degree of heterogeneity that could be found within a single core sample over a relative short range of depths of only 0.6 m. However, the typical wavelengths of the GPR radar waves are roughly from about 0.5 m to 1.5 m over the frequency range from 100 MHz to 1 GHz assuming that the wave speed in the potash formation is 50% that of  $c$ . As such, better knowledge of how the dielectric properties will vary with depth in the earth (or equivalently with stratigraphic level). Having such values would then allow us to carry out a simplified modelling of what we expect the GPR wave responses to be.

The dielectric permittivities (real and imaginary) and calculated velocities are summarized in Table 5-2. The observed real dielectric permittivities from Fig. 5-8 we can see that at (1216.65-1217.27) meter and (1223.67-1224.30) meter depths it is decreasing with increasing frequency and for the rest of the depth samples it is independent on frequency. The imaginary part of permittivity is also high for (1216.65-1217.27) meter and (1223.67-1224.30) meter which indicates the presence of minerals having higher conductivity. This result indicates the presence of clay or dense dolomite at these depths.

Fig. 5-9 shows the velocity of GPR at different frequencies. The difference between the low frequency GPR (< 50 MHz) and the high frequency GPR (> 200 MHz) becomes significant

when the clay content increase and therefore conducting a GPR at two frequencies may be used as indicator of clay content.



**Figure 5-7: Compressed samples at the eight different depths of Rocanville potash mine.**

**Table 5-2 Dielectric permittivity (real and imaginary) and velocity in different depth ranges. Data reported as mean  $\pm$  standard deviation. The measurement frequency was 10 MHz to 3 GHz**

Sample	Depth Range (m)	Real	Imaginary	Velocity (ns)
1	1216.65-1217.27	6.06 $\pm$ 0.41	0.47 $\pm$ 0.24	121.93 $\pm$ 4.11
2	1223.67-1224.30	5.33 $\pm$ 0.23	0.27 $\pm$ 0.12	130.03 $\pm$ 2.80
3	1230.28-1230.49	5.21 $\pm$ 0.04	0.02 $\pm$ 0.05	131.42 $\pm$ 0.47
4	1246.25-1247.00	4.98 $\pm$ 0.03	0.00 $\pm$ 0.05	134.46 $\pm$ 0.47
5	1255.63-1256.31	4.75 $\pm$ 0.04	-0.01 $\pm$ 0.06	137.62 $\pm$ 0.61
6	1266.34-1266.71	4.89 $\pm$ 0.05	0.09 $\pm$ 0.08	135.63 $\pm$ 0.64
7	1271.86-1272.49	4.79 $\pm$ 0.05	0.12 $\pm$ 0.11	137.08 $\pm$ 0.75
8	1284.33-1284.89	4.99 $\pm$ 0.04	0.00 $\pm$ 0.05	134.30 $\pm$ 0.56

**Note: Data are reported as mean  $\pm$  standard deviation.**



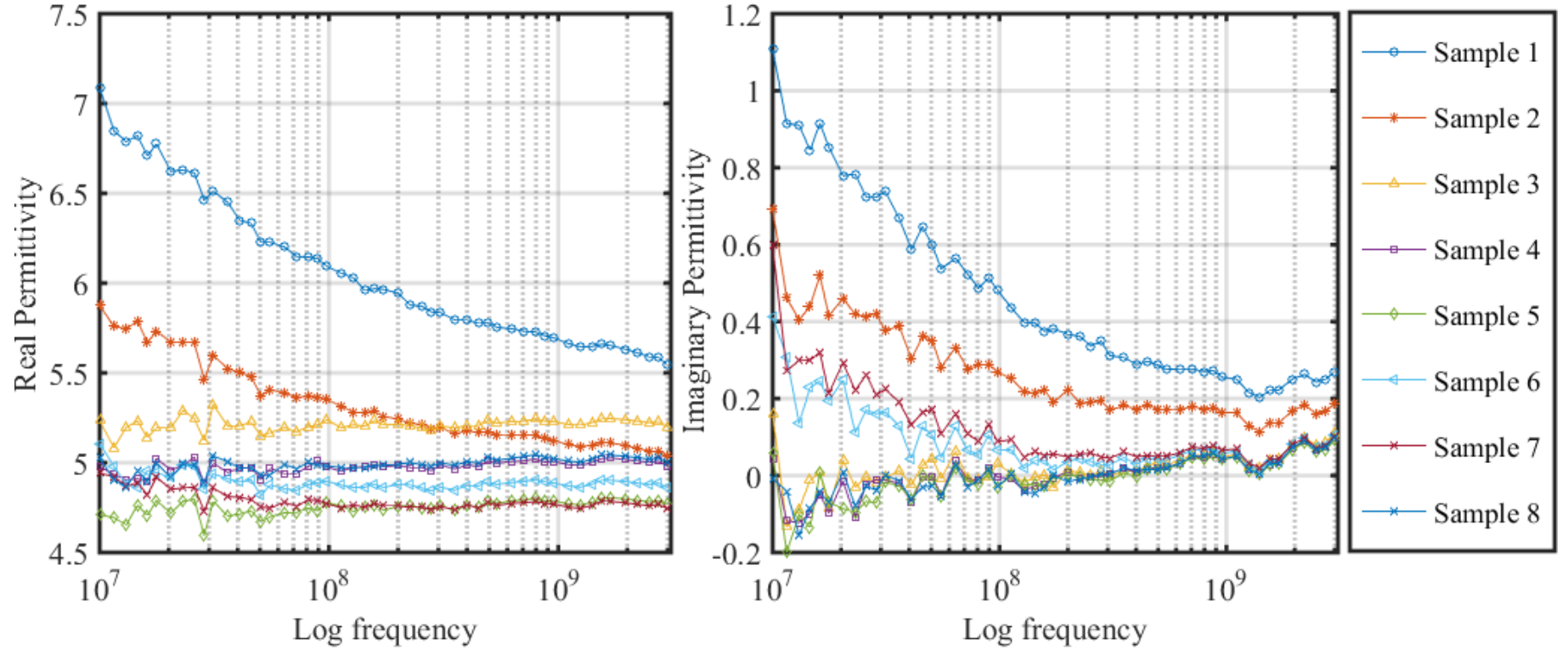


**Figure 5-8** The real and imaginary relative permittivity of samples taken from GPR reflection zone. The samples names stand for the depth it was taken from.

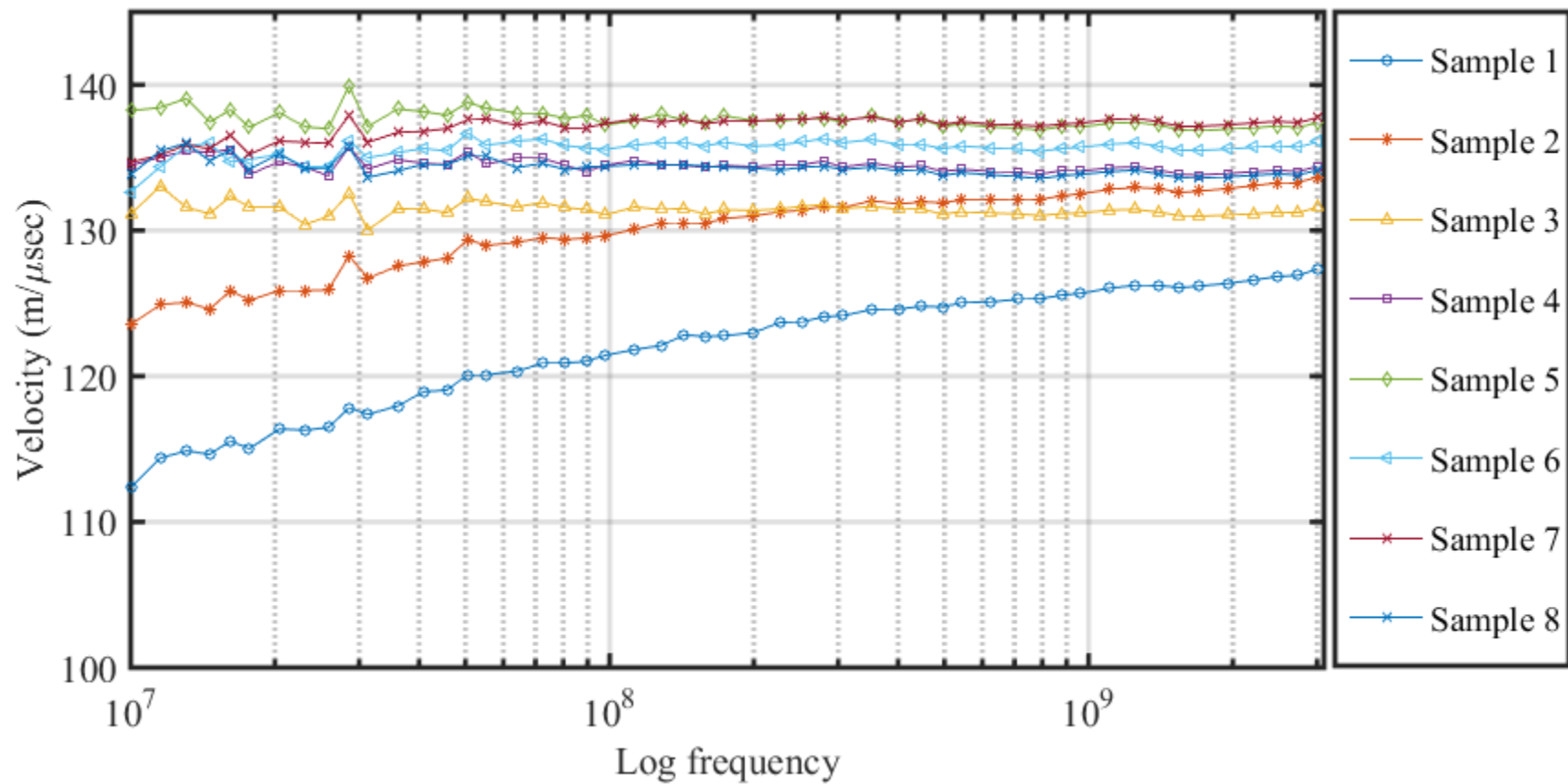


**Figure 5-9** Calculated speed wave for the samples taken from GPR reflection zone. The name of the samples stand for the depth it was taken from. At high clay content the velocity becomes a function of frequency.

**Table 5-3 The mineralogy of a sample taken from the depth range (1216.65 - 1217.27) meter.**

	Depth Range (meter)	Main minerals (XRD)	Main minerals (XRF %)				
			NaCl	KCl	SiO <sub>2</sub>	Al <sub>2</sub> O <sub>3</sub>	Fe <sub>2</sub> O <sub>3</sub>
<b>Sample 1</b>	1216.65 - 1217.27	Dolomite, Halite, Sodalite, Clinochlore, Sepiolite, Pyrite, Quartz	< 0.01	0.01	12.29	4.89	1.99

### **5.3.3 Sample 1: Depth (1216.65-1217.27) meter**

This sample is taken from a zone which was identified by the geological report of Potash Corporation of Saskatchewan (PCS) as a salty dense shaly dolomite and is from the 2<sup>nd</sup> Red Bed Formation. According to log data at this depth the density is high ( $\sim 2.6 \text{ g/cm}^3$ ) and the resistivity is low ( $\sim 11 \text{ } \Omega\text{m}$ ). The high density is because of the presence significant amount of dolomite ( $\sim 2.84 \text{ g/cm}^3$ ). The absorbed water in this sample may be causing high conductivity and low resistivity. Moreover, this absorbed water has high salinity because of the presence of NaCl which are detected by XRD. From Fig. 5-8 we can see that the permittivity dispersion of this sample at frequencies less than 50 MHz is attributed mainly to the interfacial polarization. In this case, the absorbed water content, particle size and salinity of the absorbed water mainly contribute to the polarization. This sample contain significant amount of sepiolite, clinochlore, pyrite and quartz. All clays particularly sepiolite ( $\text{Mg}_4\text{Si}_8(\text{OH})_2 \cdot 6\text{H}_2\text{O}$ ) retain water within its structure. The water layers coating the grains (whether free or bound) create a medium for the charge carrier movements. The significant amount of NaCl implies that the layer charge density

and the interfacial polarizations are high. So the increase in charge density of the layer causes increase in permittivity and conductivity as well as causes GPR reflection. Fig. 5-8 indicates the permittivity values for the compressed sample. So the plot did not represent the real in situ condition as it was made by grinding, heating and pressurizing and therefore a significant amount of water has evaporated during grinding and heating. In this case, the trend of the plot (permittivity-frequency) trend is important. Table 5-3 shows the minerals present at this depth and the percentage of the minerals. Fig. 5-10 shows the SEM image at this depth. From this image we can also identify the presence of the minerals listed in Table 5-3.

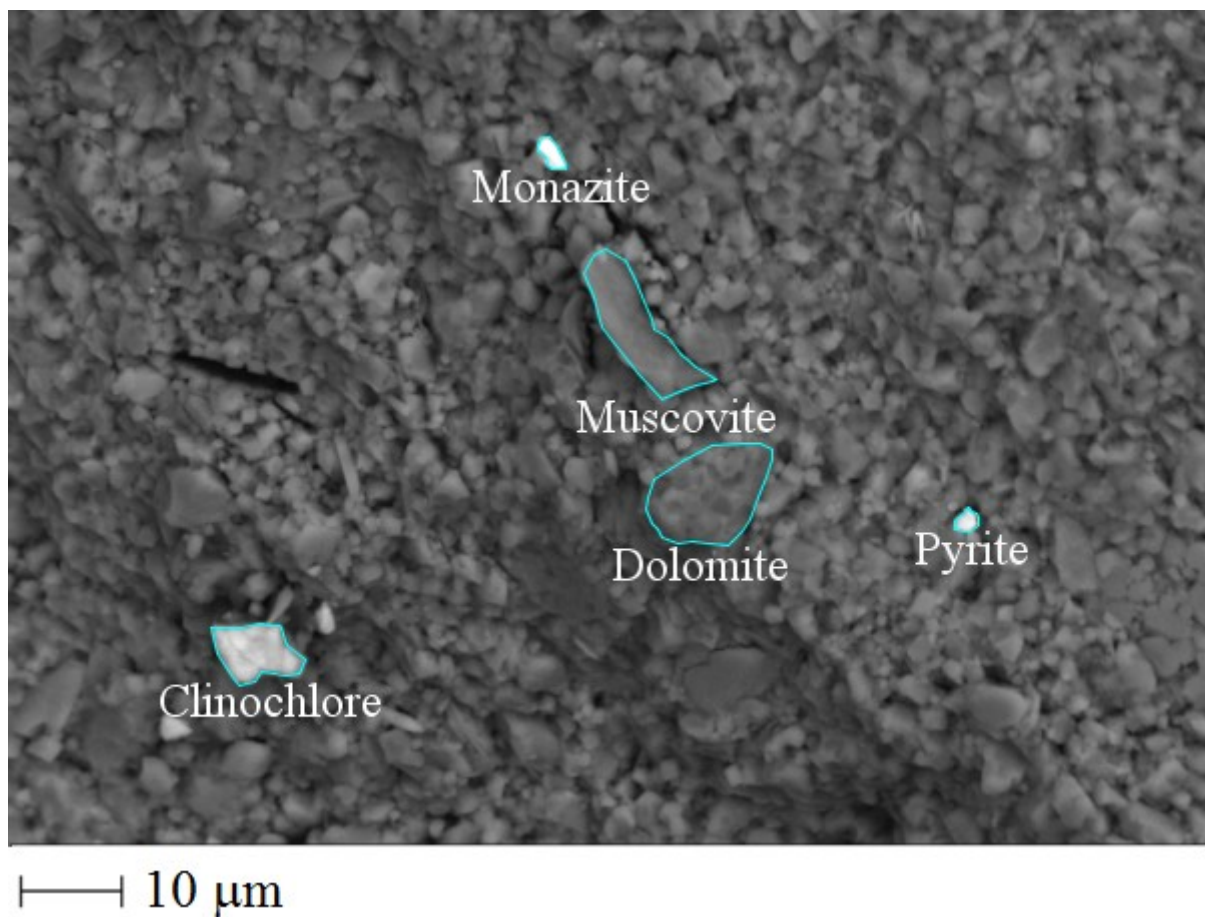


**Figure 5-10 Scanning Electron Microscope image of a sample taken from (1216.65 - 1217.27) meter depth.**

### 5.3.4 Sample 2: Depth (1223.67-1224.30) meter

According to Potash Corp. of Saskatchewan (PCS) geological report there is a transition zone between 1223 and 1225 meters where all the physical properties changes including density and resistivity. We took a sample from (1223.67-1224.30) meter depth range. The density is  $\sim 2.8 \text{ g/cm}^3$  which is relatively high and this is because of the presence of dolomite, muscovite, clinocllore, bassanite, anhydrite, and quartz mixed with some amount of NaCl (from XRD). The log data shows a low resistivity which indicates a highly conductive zone. From Fig. 5-9 we also found a relaxation frequency around 50 MHz which is an indication of attenuation of radar waves. The presence of clays especially muscovite retains water causing dispersion and as a result radar waves attenuate. Table 5-4 shows the minerals and their percentage at this depth. Fig. 5-11 is an SEM image at this depth. From the SEM image we can see the presence of dolomite which could be responsible for the GPR reflection at this depth range.

**Table 5-4 The mineralogy of a sample taken from the depth range (1223.67 - 1224.30) meter.**

	Depth Range (meter)	Main minerals (XRD)	Main minerals (XRF %)				
			NaCl	KCl	SiO <sub>2</sub>	Al <sub>2</sub> O <sub>3</sub>	Fe <sub>2</sub> O <sub>3</sub>
<b>Sample 2</b>	1223.67-1224.30	Quartz,	5.16	0.64	19.29	6.59	2.64
		Dolomite, Halite, Anhydrite, Muscovite, Chlinocllore, Bassanite					

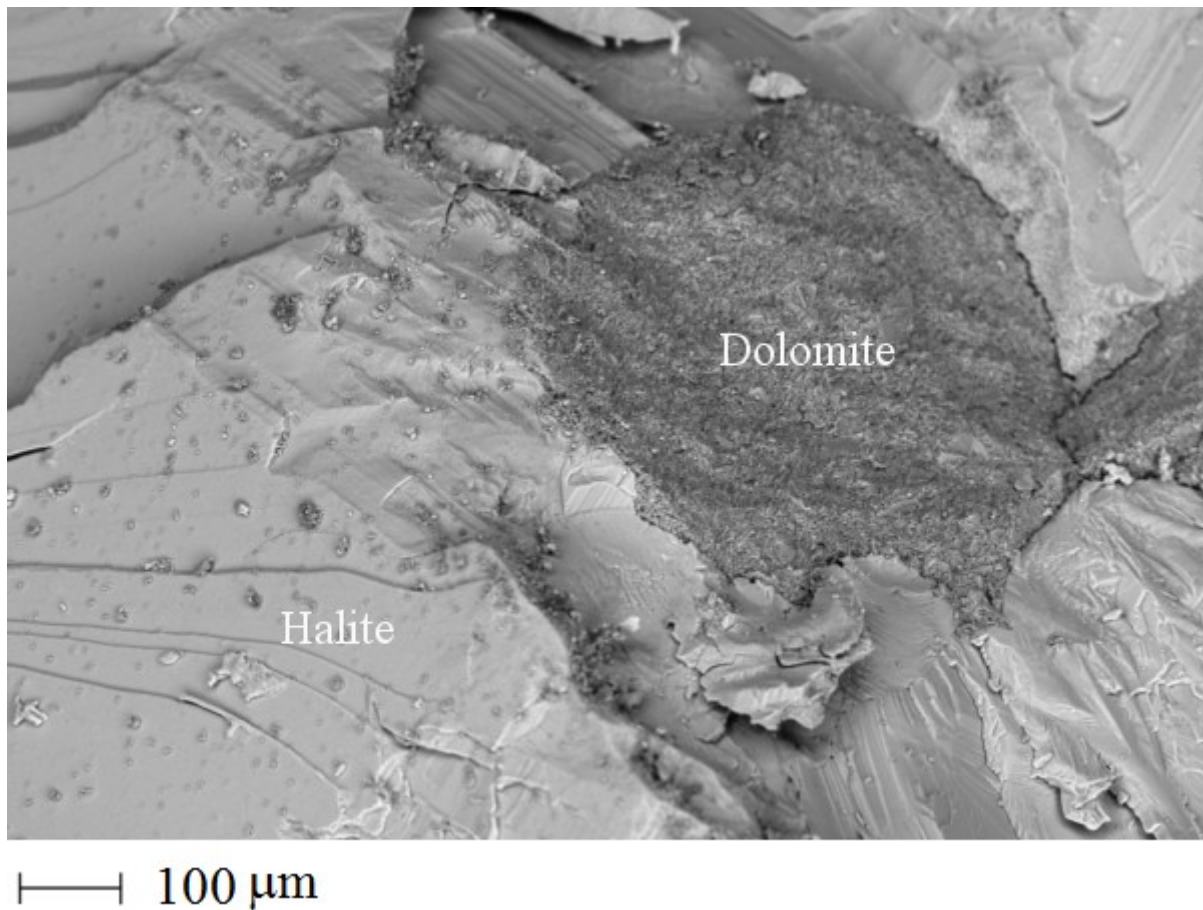


**Figure 5-11 Scanning Electron Microscope image of a sample taken from (1223.67-1224.30) meter depth.**

### **5.3.5 Sample 3: Depth (1230.28-1230.49) meter**

The sample from this depth range is mainly composed of NaCl and KCl (from XRD). But from Table 5-5 the last three element percentage ( $\text{SiO}_2$ ,  $\text{Al}_2\text{O}_3$ ,  $\text{Fe}_2\text{O}_3$ ) in the XRF represents the presence of a tiny amount of contaminants. Fig. 5-12 is the SEM image of the core at this depth. It shows the presence of halite, sylvite, muscovite and albite. To our knowledge, the presence of these contaminants might make it a GPR reflector.

**Table 5-5 The mineralogy of a sample taken from the depth range (1230.28 - 1230.49) meter.**

Sample 3	Depth Range (meter)	Main minerals (XRD)	Main minerals (XRF %)				
			NaCl	KCl	SiO <sub>2</sub>	Al <sub>2</sub> O <sub>3</sub>	Fe <sub>2</sub> O <sub>3</sub>
	1230.28-1230.49	Halite, Sylvite,  Albite	48.15	1.54	0.34	0.55	0.04

#### **5.3.6 Sample 4: Depth (1246.25-1247.00) meter**

This sample is mainly composed of NaCl, KCl and a tiny amount of dolomite (XRD and XRF) from Table 5-6. We can also find the presence of dolomite from the SEM image in Fig. 5-13. The presence of the dolomite at this depth is making the reflection on GPR image.

**Table 5-6 The mineralogy of a sample taken from the depth range (1246.25 - 1247.00) meter.**

Sample 4	Depth Range (meter)	Main minerals (XRD)	Main minerals (XRF %)				
			NaCl	KCl	SiO <sub>2</sub>	Al <sub>2</sub> O <sub>3</sub>	Fe <sub>2</sub> O <sub>3</sub>
	1246.25-1247.00	Halite, Sylvite,  Dolomite	42.42	6.48	0.36	0.33	0.05



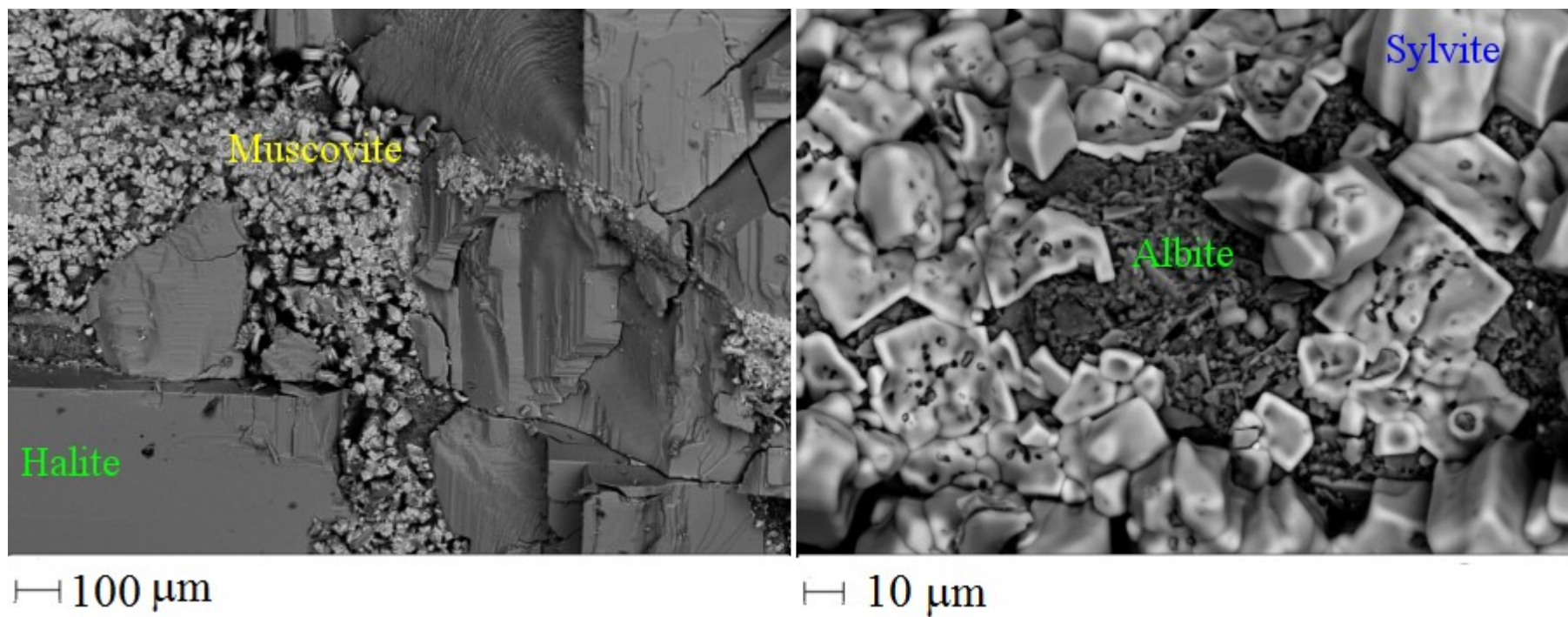


Figure 5-12: Scanning Electron Microscope image of a sample taken from (1230.28-1230.49) meter depth.



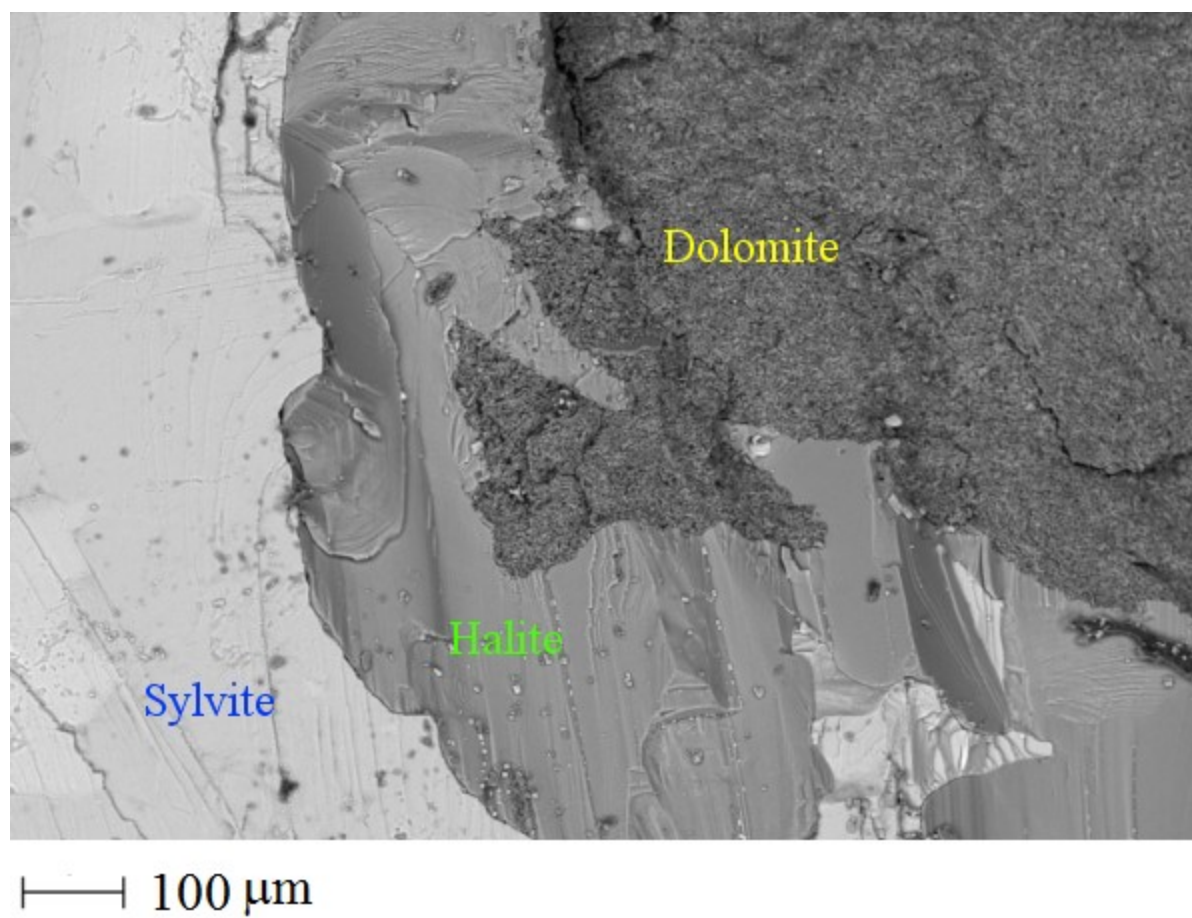


Figure 5-13 Scanning Electron Microscope image of a sample taken from (1246.25-1247.00) meter depth.

### 5.3.7 Sample 5: Depth (1255.63-1256.31) meter

This sample mainly consists of halite, anhydrite, carnallite and sylvite (from XRD and XRF). Carnallite has dielectric permittivity similar to salt. Fig. 5-14 shows the SEM image of the natural sample at this depth. The three phase- sylvite, carnallite and anhydrite are marked on the image. The presence of anhydrite is making this sample as a GPR reflector.

**Table 5-7 The mineralogy of a sample taken from the depth range (1255.63 - 1256.31) meter.**

	Depth Range (meter)	Main minerals (XRD)	Main minerals (XRF %)				
			NaCl	KCl	SiO <sub>2</sub>	Al <sub>2</sub> O <sub>3</sub>	Fe <sub>2</sub> O <sub>3</sub>
Sample 5	1255.63-1256.31	Sylvite, Carnallite, Anhydrite, Halite	42.6	1.52	0.1	0.61	0.02

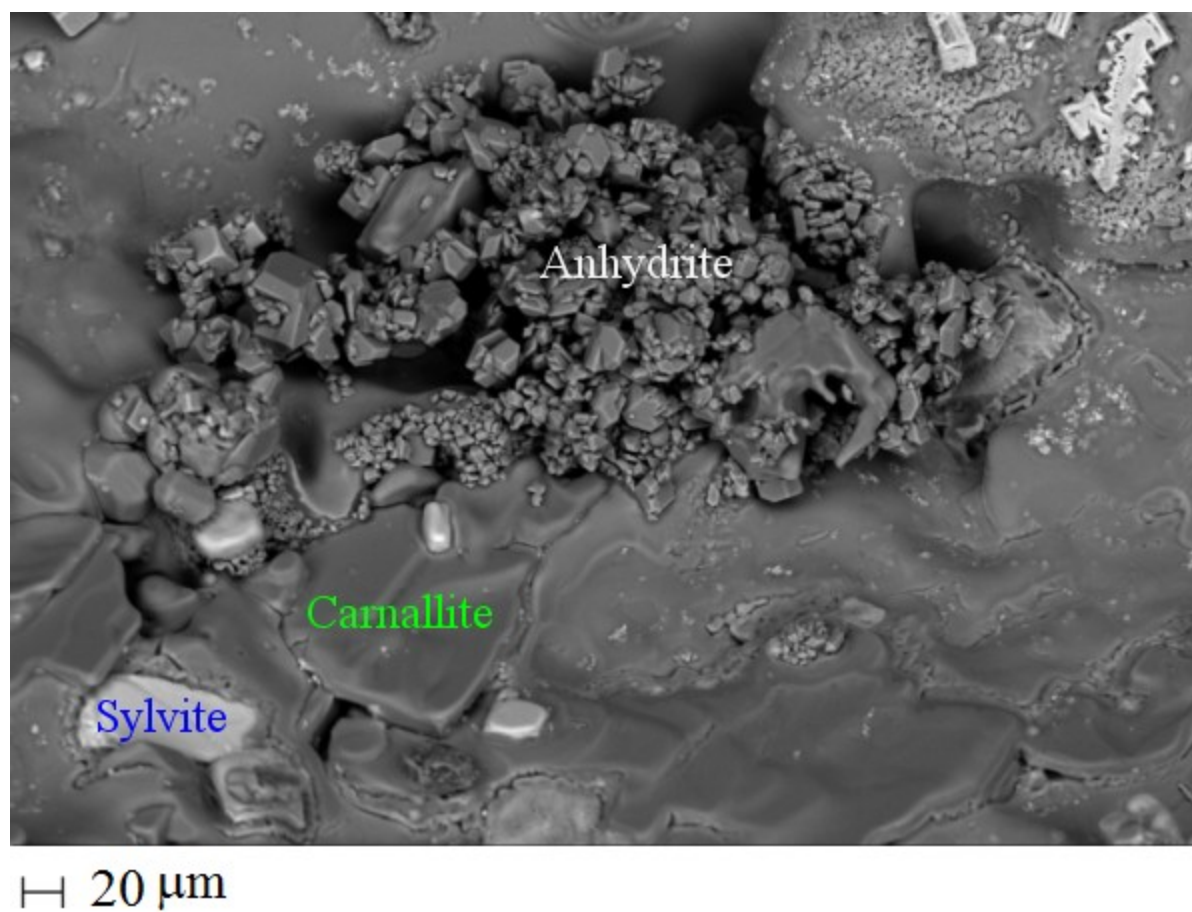


Figure 5-14 Scanning Electron Microscope image of a sample taken from (1255.63 - 1256.31) meter depth.

### 5.3.8 Sample 6: Depth (1266.34-1266.71) meter

This sample is mainly composed of anhydrite, halite and a little amount of anhydrite, sylvite and thenardite (XRD and XRF). Fig. 5-15 shows the presence of hematite as well. The presence of carnallite, anhydrite and thenardite are responsible to make this depth as a GPR reflector.

**Table 5-8 The mineralogy of a sample taken from the depth range (1266.34 - 1266.71) meter.**

	Depth Range (meter)	Main minerals (XRD)	Main minerals (XRF %)				
			NaCl	KCl	SiO <sub>2</sub>	Al <sub>2</sub> O <sub>3</sub>	Fe <sub>2</sub> O <sub>3</sub>
Sample 6	1266.34-1266.71	Sylvite, Carnallite, Anhydrite, Halite, Thenardite	47.33	0.69	0.07	0.33	0.03

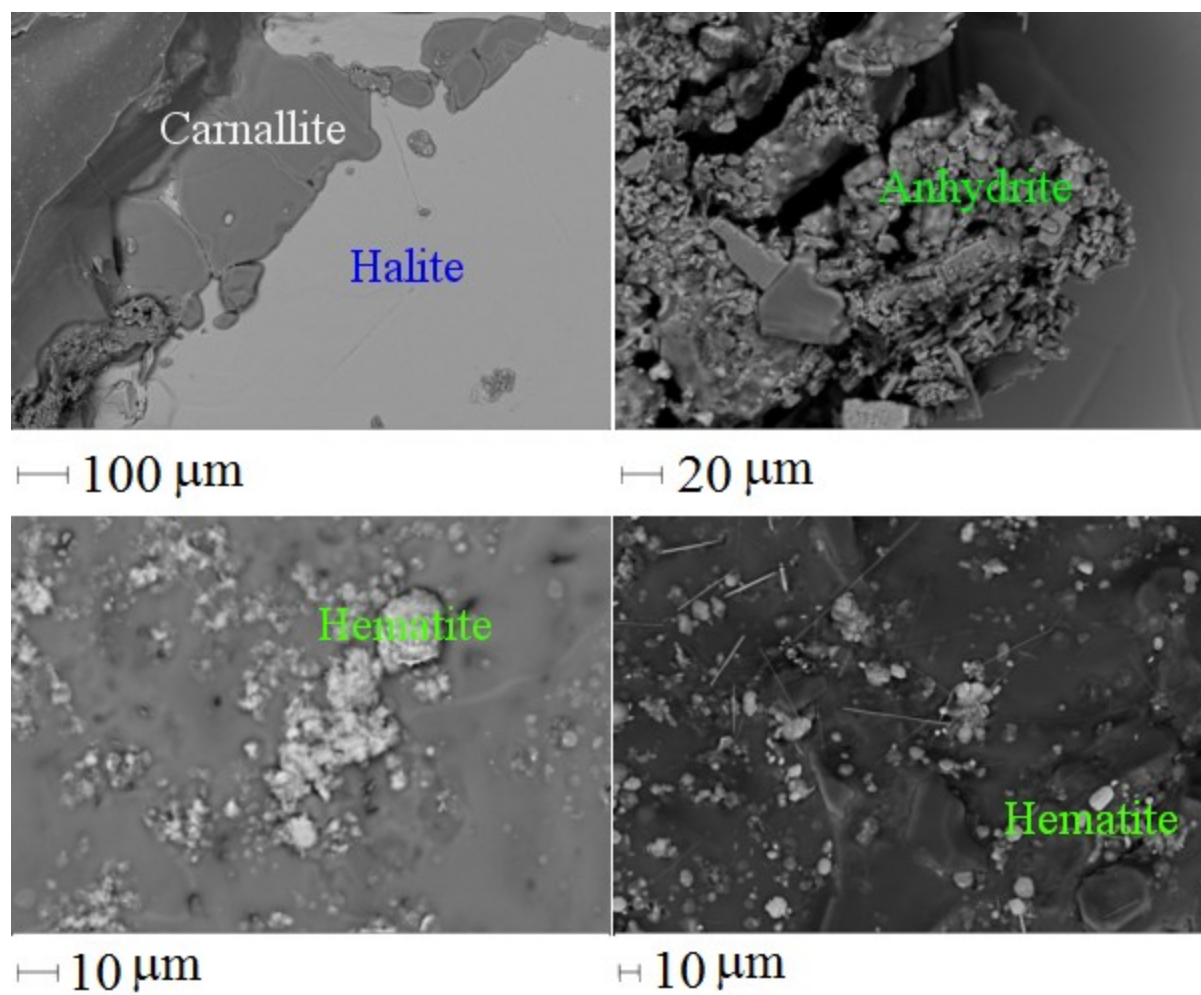


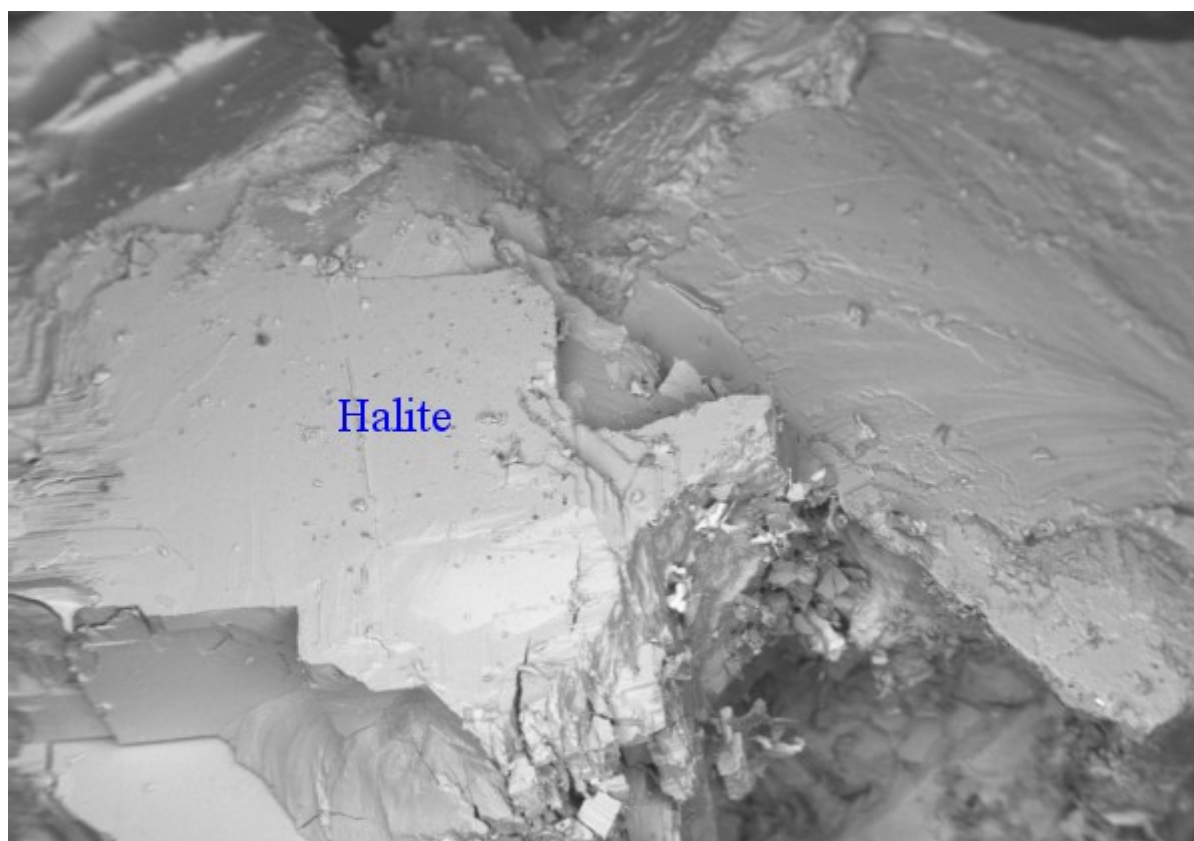
Figure 5-15 Scanning Electron Microscope image of a sample taken from (1266.34 - 1266.71) meter depth.

### 5.3.9 Sample 7: Depth (1271.86-1272.49) meter

This sample is mainly composed of halite and sylvite. The SEM in Fig. 5-16 shows the presence of halite only. As the samples was a small piece to perform SEM and the piece was only consists of halite so the image did not show the presence of sylvite. It proves that at these depths fresh salt are present. But from the XRF result in Table 5-9 still shows a tiny amount of contaminants. These contaminants might make this depth a GPR reflector.

**Table 5-9 The mineralogy of a sample taken from the depth range (1271.86 - 1272.49) meter.**

Sample 7	Depth Range (meter)	Main minerals (XRD)	Main minerals (XRF %)				
			NaCl	KCl	SiO <sub>2</sub>	Al <sub>2</sub> O <sub>3</sub>	Fe <sub>2</sub> O <sub>3</sub>
	1271.86-1272.49	Halite, Sylvite	50.34	0.06	0.01	0.18	0.03



|—| 1 mm

**Figure 5-16 Scanning Electron Microscope image of a sample taken from (1271.86 - 1272.49) meter depth.**

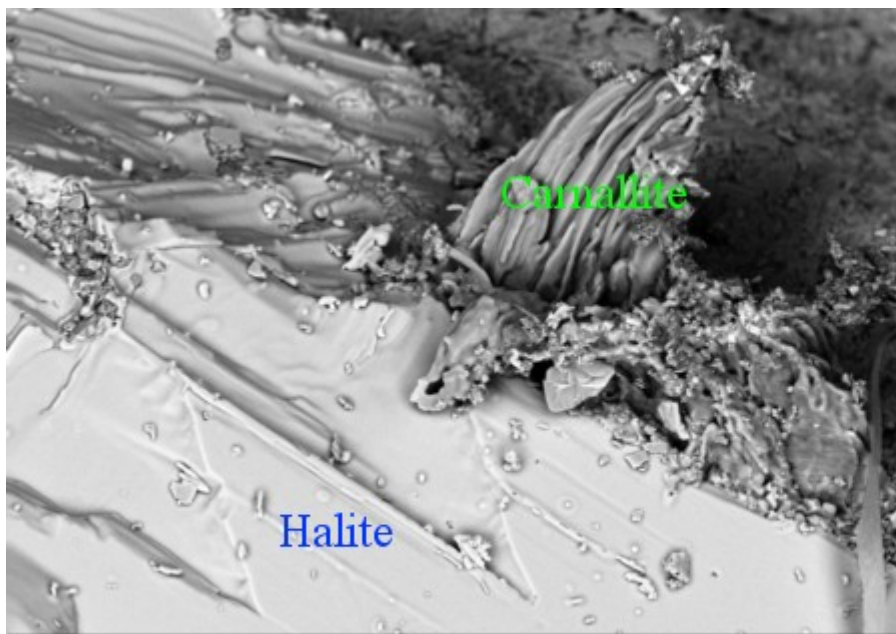
### 5.3.10 Sample 8: Depth (1284.33 - 1284.89) meter

From Table 5-10 we can find that this sample mainly composed of halite, sylvite, dolomite and anhydrite according to XRD. XRF was not done on this sample. According to SEM image in Fig. 5-17, this sample also contains some amount of carnallite as well. The presence of dolomite, anhydrite and carnallite might cause reflection on the GPR image.

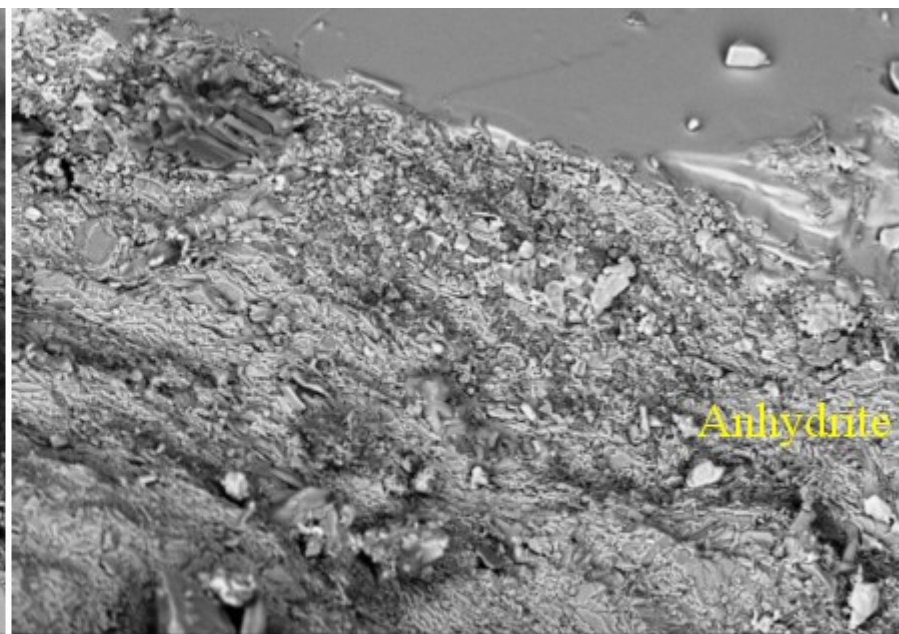
**Table 5-10 The mineralogy of a sample taken from the depth range (1284.33 - 1284.89) meter.**

Sample 8	Depth Range (meter)	Main minerals (XRD)	Main minerals (XRF %)				
			NaCl	KCl	SiO <sub>2</sub>	Al <sub>2</sub> O <sub>3</sub>	Fe <sub>2</sub> O <sub>3</sub>
	1284.33-1284.89	Halite, Sylvite,  Dolomite,  Anhydrite	--	--	--	--	--





20  $\mu\text{m}$



20  $\mu\text{m}$

Figure 5-17 Scanning Electron Microscope image of a sample taken from (1284.33 - 1284.89) meter depth.

From the above mentioned XRD, XRF and SEM results we can suggest that the GPR reflection in this particular case is because of the presence of a relatively conductive zone. The conductivity of the zones is related to the amount of clay content. The conductive (or clayey) zones should show frequency dependent behavior. So we anticipate that conducting the survey at frequency less than 200 MHz and at 50 MHz can be useful in locating clayey zones. This is because the contrast in the reflectivity of GPR in the clayey zones is much greater at the low frequency. Detail about this zone is given below:

#### ***5.3.11 Relatively conductive zone (e.g clay or clayey evaporite)***

In this geological environment, the most conductive zones are those containing some amount of clay. The conductivity of the clay may be further enhanced by the salinity of the adsorbed water. According to the resistivity log data five out of the seven GPR reflector zones are highly conductive (Table 5-11). The resistivities of the five zones were less than 250 Ohm.m, compared to the ~1800 ohm.m for the nearby relatively clean evaporite. Only one zone near 1290 m depth has a relatively high resistivity of 1767 ohm.m.

**Table 5-11 Resistivities of GPR reflection zones.**

Zone name (or description)	Zone's Depth(m)	Peak resistivity depth	Resistivity(ohm.m)
2 <sup>nd</sup> red bed	1215 to 1217	Constant low resistivity	11.53
Transition zone (from clay to evaporite )	1223 to 1224.5	1223.31m	152.15
White bear marker	1235.35 to 1237.18	1235.81m	8.38
Halite + clay flakes	1275.28 to 1275.8	1275.58m	229.19
Anhydrite zone	1285.79 to 1286.4	1286.1m	307.71
Anhydrite zone	1262.93 to 1263.24	1263.24m	86.5
Clean evaporite zone	Around 1290	1289.45m	1767

### 5.3.12 Brine inclusions effect

Brine inclusions within the salt rock might have a small effect on the dielectric permittivity because we think that their concentration (or number of inclusions within a unit volume) is low and also because of the high salt concentration. Salt solution has a lower permittivity than pure water. For example the permittivity of 4 mol/l of NaCl is approximately 40 [Zasetsky and Svishchev, 2001] compared to ~80 for pure water. Igel *et al.* [2006] reported a lack of distinct reflection from a massive brine reservoir that exist in a potash salt mine (in Germany). They attribute this to the presence of a gradient zone or gradient increase in the brine content inside the anhydrite. We haven't measured the permittivity of evaporite samples that contain brine inclusions but we think that if the concentration of these inclusions is not high enough to cause a reflection.

## 5.4 Reflection modelling

Reflection coefficients for the above mentioned depths were calculated using the dielectric values in provided Table 5-2. We have used the following formula to calculate the reflection coefficients (RC)

$$RC = \left[ \frac{\sqrt{\epsilon_1} - \sqrt{\epsilon_2}}{\sqrt{\epsilon_1} + \sqrt{\epsilon_2}} \right] \quad \text{Eq. (5-1)}$$

where  $\epsilon_1$  and  $\epsilon_2$  are dielectric constants of upper and lower layers respectively. We have calculated time from the relation between distance and velocity. The velocity values are presented in Table 5-2. Fig. 5-18 shows the change of reflection coefficients with frequency. From Fig. 5-18 it is noted that reflection coefficients (RC1, RC2, RC5 and RC7) started decreasing with the increase in frequency. The mean reflection coefficients and the corresponding times are summarized in Table 5-12.

The fact that there is substantial dispersion of the wave speeds for some of the layers with the corresponding attenuation will affect the modelling of the reflectivity in two ways. First, if there is substantial dispersion and attenuation this means that the wave pulse will change its shape during its transit path. This is most easily considered in the frequency domain where after having propagated a given distance the phases of the different frequency components will be shifted and because the amplitudes of these different components will experience differing degrees of attenuation. As Fig 5-18 illustrates, this is further complicated by the fact that the different frequency components will be reflected with different strengths. Proper modelling of such responses requires that all of these different factors be taken into account. This is not done as part of this thesis and it remains for future work.

Instead, we assumed that we could use the average values of the reflectivity and wave speed for each sample. This is somewhat justified by the fact that the transit distance and attenuations are both small such that we do not expect the waveforms to change greatly. A synthetic radar trace

was generated by convolving a Ricker wavelet with the calculated reflection coefficients. The Ricker wavelet equation is given below with frequency  $f$  at time  $t$ :

$$w = (1 - 2\pi^2 f^2 t^2) e^{-\pi^2 f^2 t^2} \quad \text{Eq. (5-2)}$$

By convolving these two signals we have generated a synthetic GPR trace which is shown in Fig. 5-20. Fig. 5-19 shows that the polarity of the output signal depends on the polarity of reflection coefficients.

**Table 5-12 Reflection coefficients and time.**

RC	Time ( $\mu$ s)
0.0332	9.68
0.0153	19.06
0.0115	38.05
0.0117	75.98
0.0094	151.99
0.0060	304.06
0.0140	608.23

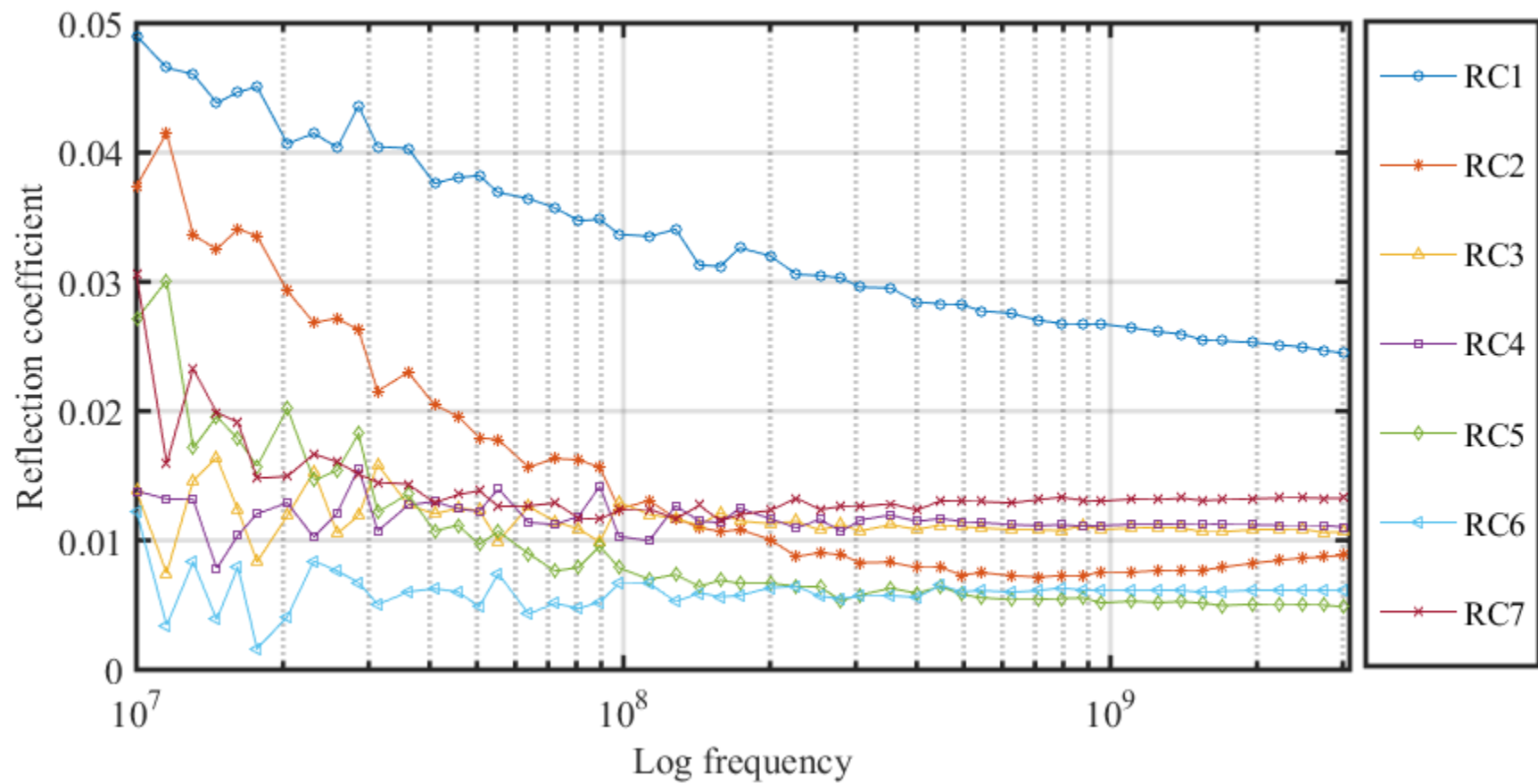
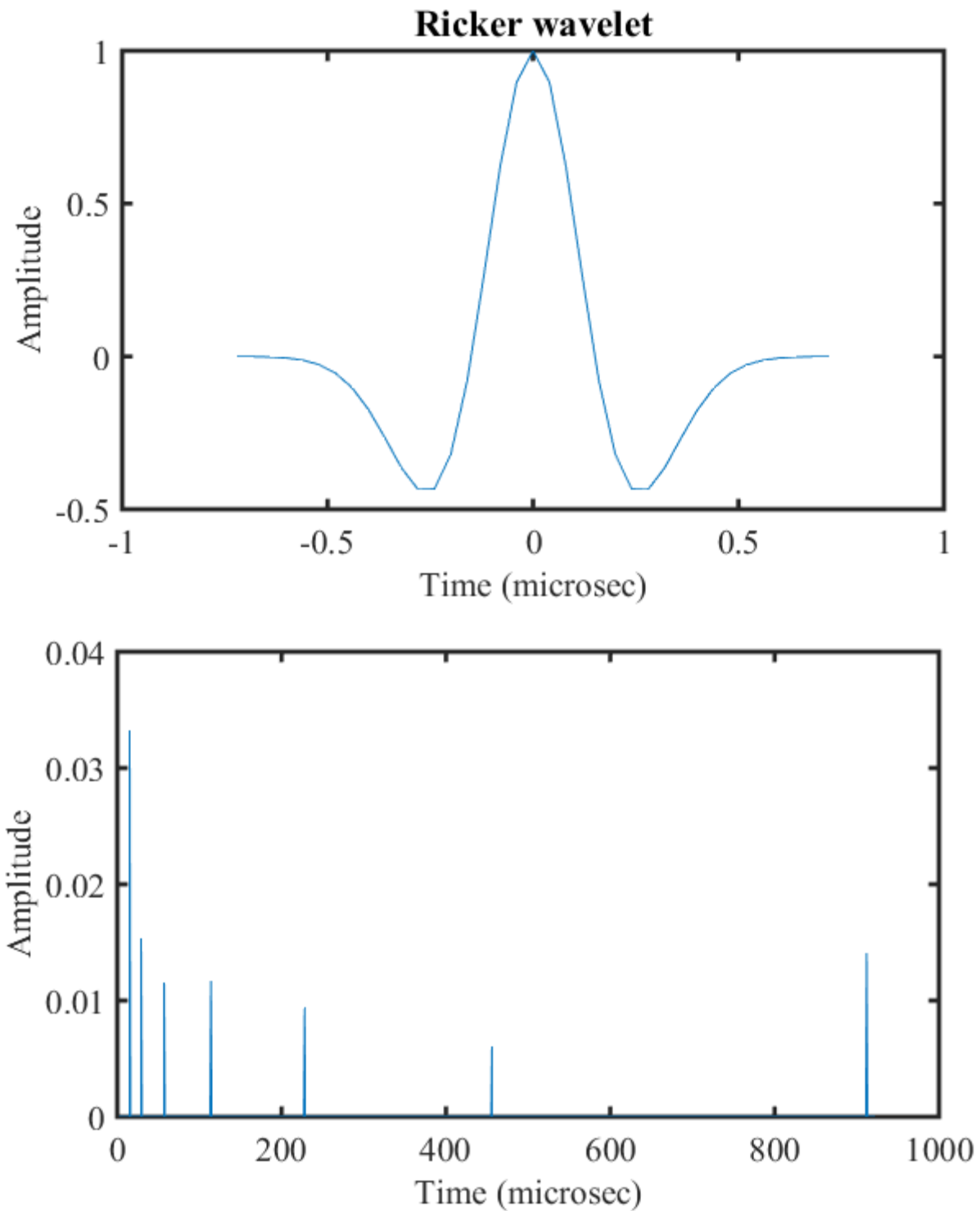
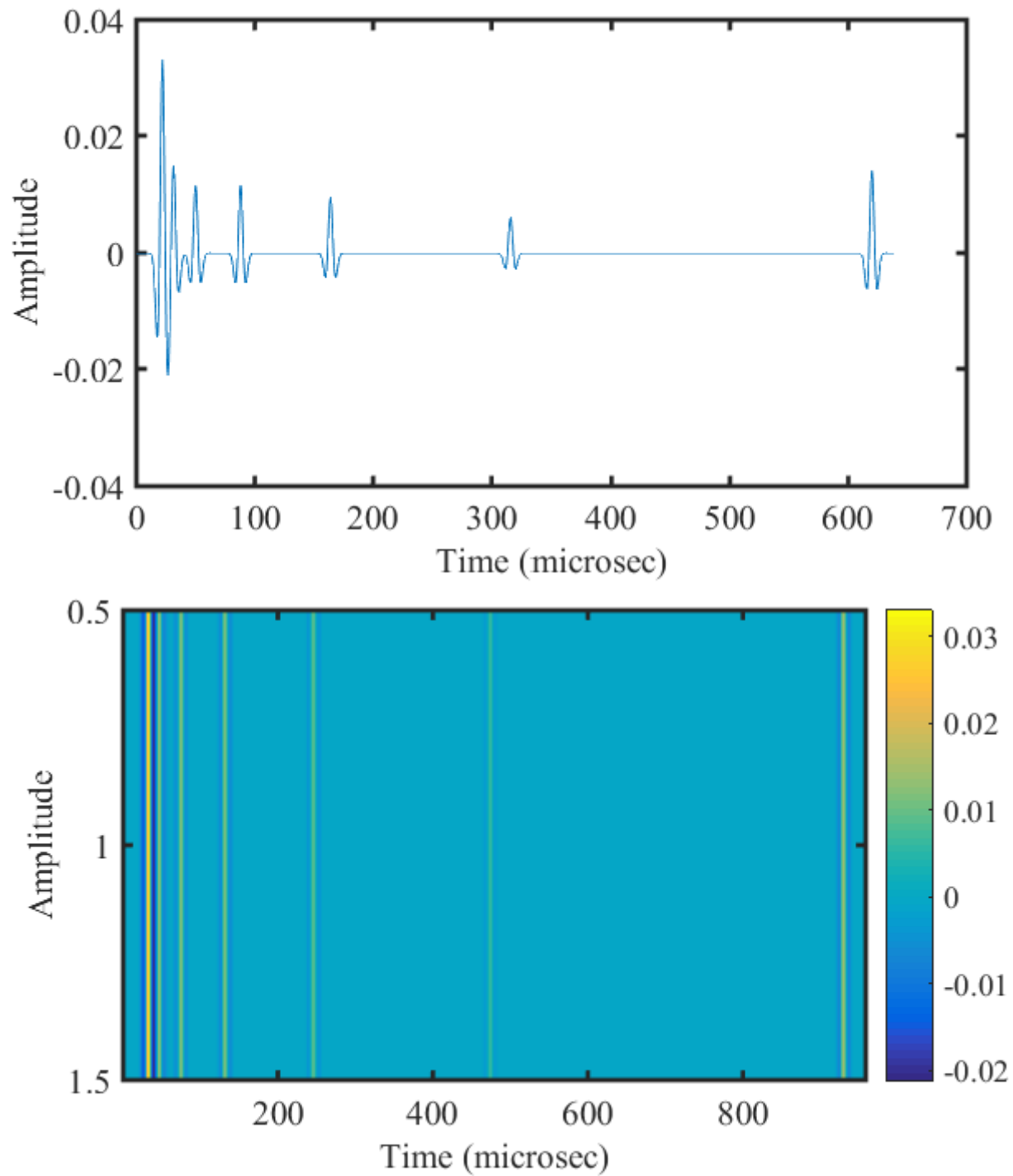


Figure 5-18 Change of reflection coefficient with frequency.



**Figure 5-19 Ricker wavelet (up). Generated signal using reflection coefficients of eight different depths of potash mine and corresponding propagation time (down).**



**Figure 5-20** Synthetic GPR trace after convolution of the above mentioned signal with the ricker wavelet.



From Fig. 5-20 we can find that the amplitude peak is highest at 19.38  $\mu s$  which represents a strong reflection between depth1 (1216 meter) and depth2 (1223 meter). If we consider the XRD and XRF data from Table 5-3 and Table 5-4 we can find that at these depths the contaminant mineral percentage is highest. We also got reflections for the rest of the depths but the reflections are less strong than the reflection event between depth1 and depth2. Therefore, combining both the mineralogical analyses (XRD, XRF and SEM) and the reflection modelling we can conclude that the presence of contaminant minerals with salt is mainly responsible for the GPR reflection in Rocanville potash mine.

## **5.5 Summary**

In this chapter we have studied core rock materials from Rocanville potash mine. At first a core from (1238.68-1239.37) meter depth was cut into 14 pieces. Dielectric measurements were done in two different ways. The two ways were placing each core pieces directly onto the sensor and measurements on the cold compressed samples of the same 14 pieces. Cold compressed samples showed better dielectric values than the raw pieces. This result proves the importance of cold compressed samples. Then eight samples from eight different depths were prepared using the cold compressed technique. Dielectric measurements as well as mineralogical analyses like XRD, XRF and SEM were done on these samples. This chapter was ended up with a forward modelling. Combining the reflection modelling result with the mineralogical analyses we came up with the idea that the reflections on GPR image of potash mine caused because of the presence of contaminant minerals.

## CHAPTER 6. CONCLUSION

### 6.1 Summary of Work Completed

Knowledge of dielectric permittivity and the factors influencing it is important to understand the reflections on GPR images. Moreover, the lack of knowledge of what dielectric permittivities are may cause misinterpretation of GPR results. This study was done to support the interpretation of GPR surveys conducted in the potash mines by Potash Corporation of Saskatchewan (PCS). Reflection events observed in GPR profiles result from contrast in dielectric permittivity between different materials within the mines as well as the absorption of the radar waves while propagating into and back from the formation influences the quality of the GPR signal. Therefore, the knowledge of the dielectric permittivity values of the evaporites and their contaminants is necessary to maximize the utility of the GPR data more efficient real-time mining, particularly for mine safety.

In this study we have measured dielectric permittivities over the frequency range of 10 MHz to 3 GHz on a variety of synthetic and natural evaporite minerals and rocks that may occur in the mining environment. The main findings of this study are:

1. The radar velocity in clean dry evaporite minerals is frequency-independent as the real permittivity is frequency independent and the imaginary permittivity is low enough that we can ignore it.

2. Nine mixing theories were employed to calculate the dielectric permittivities for different types of two phase mixtures (for example, air-filled NaCl, water saturated NaCl, mixture of NaCl and KCl). A series of eight porous NaCl and eight porous KCl samples were prepared and their permittivity values were compared with the theoretical model. For porous

NaCl our measurement data were best described by the Maxwell-Garnett theory but for porous KCl it was not clear which mixing model worked best. We may need to consider in future better ways to control and measure the porosity of such types of samples.

3. A core sample from (1238.68-1239.37) meter depth of Rocanville potash core was divided into 14 pieces. Each of the pieces were placed directly on the sensor and their dielectric permittivities were individually measured. The dielectric values for different pieces were within 2.5 to 4.5. This result was troublesome and suggested that the technique does not work well on the unaltered potash ore as the main mineral composition of the mine has dielectric values 4.85 and 5.9. Each of these 14 pieces were crushed into powder and cold compressed them at 250 MPa to form reconstituted samples. The dielectric values for these cold compressed samples ranges mostly in between 4.5 to 5.2 which is a better result compared to that of placing core directly on the sensor although there remains some concern that porosity affects the results.

4. A series of eight samples were prepared from eight different depths along a rock core taken from the Rocanville potash mine. To interpret the dielectric permittivity values of these samples mineralogical analysis were done using a number of techniques including X-ray diffraction (XRD), X-ray fluorescence (XRF) and scanning electron microscopy (SEM). The first two techniques were used to obtain information about the mineralogy and chemical composition of the samples and the third one was used to obtain information about the geometry of the grains.

5. The reflection of GPR waves in potash mines is caused mainly by the contamination of evaporite by clay. The clay absorbed water gives rise to the Maxwell-Wagner polarization, which could cause a significant increase in the permittivity at lower frequency.

6. The EM wave velocity of evaporite samples contaminated with clay is frequency dependent between 10 MHz to 200 MHz. Therefore, conducting the GPR survey at these frequencies might give indication of clay contamination.

## **6.2 Recommendation for Future Work**

1. We have done theoretical modelling only for two phase mixtures of mostly air filled samples but did not work with water saturated samples. Measurements could be done on water saturated samples and the measurement values can be compared with the water saturated theoretical modelling.

2. We tried to make samples using two different minerals (glass beads with NaCl and KCl) but the measurement values did not fit with any mixing law. We are confident it happened due to the difficulty to create pore free mixtures even after applying high pressure. Therefore, we did not present these results in the results section. The permittivity data from these samples did not fit as the samples were porous. In practice, these samples were three phase mixtures instead of two phases. Solving the various mixing laws for three phase mixtures may be an important future task.

3. We have measured the porosity mainly using He pycnometer. It would be better if we can measure the porosity of the samples using mercury porosimeter and compare the results from these two techniques.

4. We prepared only eight samples from different depths of Rocanville potash mine. More samples can be prepared and it will give us more precise results.

5. In this study we calculated the reflection coefficients of eight samples and generated a synthetic GPR trace with that but we do not have any real GPR data from the potash mine. It will be a good practice if we could manage real GPR data from them and compare our forward modelling result with that. The modelling procedures that we employed assumed that dispersion and attenuation could be ignored. While we believe this to be approximately true for our data set future plans will need to include a more sophisticated approach to modelling of the reflectivity to account for these frequency dispersive effects.

## References

- Agilent (2003), Agilent Technologies Impedance Measurement Handbook. <http://www.tnnc.ncsu.edu/files/testing/manuals/ImpedanceMeasurementHandbookRev3.pdf>, Agilent Technologies, Inc.
- Agilent (2005), Agilent application note “Basics of Measuring the Dielectric Properties of Materials”, from <http://cp.literature.agilent.com/litweb/pdf/5989-2589EN.pdf>, Agilent Technologies, Inc.
- Agilent (2001), Agilent Advanced impedance measurement capability of the RF I-V method compared to the network analysis method. <http://cp.literature.agilent.com/litweb/pdf/5988-0728EN.pdf>, Agilent Technologies, Inc.
- al Hagrey, S. A., and C. Muller (2000), GPR study of pore water content and salinity in sand, *Geophysical Prospecting*, 48(1), 63-85.
- Annan, A. P., J. L. Davis, and D. Gendzwill (1988), Radar Sounding in Potash Mines, Saskatchewan, Canada, *Geophysics*, 53(12), 1556-1564.
- Arai, M., and J. G. P. Binner (1995), Estimating Errors Due to Sample Surface-Roughness in Microwave Complex Permittivity Measurements Obtained Using a Coaxial Probe, *Electronics Letters*, 31(2), 115-117.
- Avelin, J., and A. Sihvola (2002), Polarizability of polyhedral dielectric scatterers, *Microwave and Optical Technology Letters*, 32(1), 60-64, doi:10.1002/mop.10091.
- Baker, G. S., T. E. Jordan, and J. Pardy (2007), An introduction to ground penetrating radar (GPR), *Stratigraphic Analyses Using Gpr*, 432, 1-18, doi:10.1130/2007.2432(01).
- Bergman, D. J., and D. Stroud (1992), Physical-properties of macroscopically inhomogeneous-media, *Solid State Physics: Advances in Research and Applications*, Vol 46, 46, 147-269, doi:10.1016/s0081-1947(08)60398-7.
- Brovelli, A., ; , and G. Cassiani (2008), Effective permittivity of porous media: a critical analysis of the complex refractive index model, *Geophysical Prospecting*, 56(5), 715-727.

- Bruggeman, D. A. G. (1935), Calculation of various physics constants in heterogenous substances I Dielectricity constants and conductivity of mixed bodies from isotropic substances, *Annalen Der Physik*, 24(7), 636-664.
- Chen, L. F., C. K. Ong, C. P. Neo, V. V. Varadan, and V. K. Varadan (2004), *Microwave Electronics: Measurement and Materials Characterization*, John Wiley & Sons Ltd.
- Chiba, M., et al. (2006), Measurement of attenuation length for radio wave in natural rock salt samples concerning ultra high energy neutrino detection, *International Journal of Modern Physics A*, 21, 25-29.
- Choy, T. (1999), *Effective Medium Theory: Principles and Applications*, 182 pp., Oxford University Press, New York.
- Chung, C. C., and C. P. Lin (2009), Apparent Dielectric Constant and Effective Frequency of TDR Measurements: Influencing Factors and Comparison, *Vadose Zone Journal*, 8(3), 548-556, doi:10.2136/vzj2008.0089.
- Clarke, R. N., A. P. Gregory, D. Cannell, M. Patrick, S. Wylie, I. Youngs, and G. Hill (2003), *A guide to the characterisation of dielectric materials at RF and microwave frequencies.*, Institute of Measurement and Control / National Physical Laboratory.
- Cosenza, P., C. Camerlynck, and A. Tabbagh (2003), Differential effective medium schemes for investigating the relationship between high-frequency relative dielectric permittivity and water content of soils, *Water Resources Research*, 39(9).
- Czichos, H., T. Saito, and L.R. Smith (2006), *Handbook of Materials Measurement Methods*, Springer Science and Technology Media.
- Dalton, F. N., W. N. Herkelrath, D. S. Rawlins, and J. D. Rhoades (1984), Time-domain reflectometry - simultaneous measurement of soil-water content and electrical-conductivity with a single probe, *Science*, 224(4652), 989-990, doi:10.1126/science.224.4652.989.
- Dalton, F. N., and M. T. Vangenuchten (1986), The time-domain reflectometry method for measuring soil-water content and salinity, *Geoderma*, 38(1-4), 237-250, doi:10.1016/0016-7061(86)90018-2.

Daniels, D. J., and I. E. Engineers (2004), *Ground penetrating radar*, Institution of Electrical Engineers.

Daniels, D. J., D. J. Gunton, and H. F. Scott (1988), Introduction to Subsurface Radar, *Iee Proceedings-F Radar and Signal Processing*, 135(4), 278-320.

Davies, C. E., S. J. Tallon, and N. Brown (2005), Continuous monitoring of bulk density and particle size in flowable powders and grains, *Chemical Engineering Research & Design*, 83(A7), 782-787.

Dirksen, C., and S. Dasberg (1993), Improved calibration of time-domain reflectometry soil-water content measurements, *Soil Science Society of America Journal*, 57(3), 660-667.

Dobson, M. C., F. T. Ulaby, M. T. Hallikainen, and M. A. Elrayes (1985), Microwave dielectric behavior of wet soil .2. Dielectric mixing models, *Ieee Transactions on Geoscience and Remote Sensing*, 23(1), 35-46, doi:10.1109/tgrs.1985.289498.

Dragoman, D., and M. Dragoman (2002), *Optical Characterization of Solids*, Springer.

Drews, R., O. Eisen, D. Steinhage, I. Weikusat, S. Kipfstuhl, and F. Wilhelms (2012), Potential mechanisms for anisotropy in ice-penetrating radar data, *Journal of Glaciology*, 58(209), 613-624.

Dube, D. C. (1970), Study of Landau-Lifshitz-Looyengas Formula for Dielectric Correlation between Powder and Bulk, *Journal of Physics D-Applied Physics*, 3(11), 1648-&.

Dube, D. C., and R. Parshad (1970), Study of bottchers formula for dielectric correlation between powder and bulk

*Journal of Physics D-Applied Physics*, 3(5), 677-&, doi:10.1088/0022-3727/3/5/306.

Dube, D. C., R. S. Yadava, and R. Parshad (1971), Formula for Correlating Dielectric Constant of Powder and Bulk, *Indian Journal of Pure & Applied Physics*, 9(9), 719-&.

Dyer, S. A. (2004), *Wiley Survey of Instrumentation and Measurement*, Wiley-IEEE Press.

Economos, G. (Ed.) (1958), *Effect of microstructure on the electrical and magnetic properties of ceramics*, 199-213 pp., John Wiley, New York.



- Egorov, V. N. (2007), Resonance methods for microwave studies of dielectrics - (Review), *Instruments and Experimental Techniques*, 50(2), 143-175, doi:10.1134/s0020441207020017.
- Ellison, W. J., K. Lamkaouchi, and J. M. Moreau (1996), Water: a dielectric reference, *J. Mol. Liq.*, 68(2-3), 171-279.
- Garnett, J. C. M. (1904), Colours in metal glasses and in metallic films, *Philosophical Transactions of the Royal Society of London Series a-Containing Papers of a Mathematical or Physical Character*, 203, 385-420, doi:10.1098/rsta.1904.0024.
- Giesche, H. (2006), Mercury porosimetry: A general (practical) overview, *Particle & Particle Systems Characterization*, 23(1), 9-19, doi:10.1002/ppsc.200601009.
- Gorham, P., D. Saltzberg, A. Odian, D. Williams, D. Besson, G. Frichter, and S. Tantawi (2002), Measurements of the suitability of large rock salt formations for radio detection of high-energy neutrinos, *Nuclear Instruments & Methods in Physics Research Section a-Accelerators Spectrometers Detectors and Associated Equipment*, 490(3), 476-491.
- Gregory, A. P., and R. N. Clarke (2006), A review of RF and microwave techniques for dielectric measurements on polar liquids, *Ieee Transactions on Dielectrics and Electrical Insulation*, 13(4), 727-743.
- Gregory, A. P., and R. N. Clarke (2007), Dielectric metrology with coaxial sensors, *Measurement Science & Technology*, 18(5), 1372-1386.
- Griffiths, D. J. (2012), *Introduction to Electrodynamics* 4 edition (Sept. 26 2012) ed., Addison-Wesley.
- Grobe, M. (2002), Distribution and thickness of salt within the Devonian Elk Point Group, Western Canada Sedimentary Basin Rep. 2002-02, 35 pp, Alberta Energy and Utilities Board, Alberta Geological Survey, Edmonton.
- Guéguen, Y., and V. Palciauskas (1994), *Introduction to the Physics of Rocks*, 294 pp., Princeton University Press, Princeton, New Jersey.
- Hanai, T. (1968), *Electrical Properties of Emulsions*, Academic Press, London.
- Hardy, H. R., and M. Langer (1989), *Mechanical Behavior of Salt: Proceedings of the 2nd Conference*, Trans Tech Pubn.

Hargreaves, N. (1977), The polarization of radio signals in the radio echo sounding of ice sheets, *Journal of Physics D: Applied Physics*, 10(9), 1285.

Hargreaves, N. (1978), The radio-frequency birefringence of polar ice, *Journal of Glaciology*, 21, 301-313.

Hecht, E. (2002), *Optics*, 4th edition ed., Addison-Wesley.

Hilhorst, M. A., C. Dirksen, F. W. H. Kampers, and R. A. Feddes (2000), New dielectric mixture equation for porous materials based on depolarization factors, *Soil Science Society of America Journal*, 64(5), 1581-1587.

Hoekstra, P., and A. Delaney (1974), Dielectric properties of soils at uhf and microwave-frequencies, *Journal of Geophysical Research*, 79(11), 1699-1708, doi:10.1029/JB079i011p01699.

Holser, W. T., Unterber.Rr., R. J. S. Brown, Fredriks.Oa., and F. A. Roberts (1972), Radar Logging of a Salt Dome, *Geophysics*, 37(5), 889-&.

Holter, M. (1969), The Middle Devonian Prairie Evaporite of Saskatchewan, Report No. 123Rep. 123, 133 pp, Dept. of Mineral Resources, Geological Sciences Branch, Industrial Minerals Division, Regina.

Hook, W. R., and N. J. Livingston (1996), Errors in converting time domain reflectometry measurements of propagation velocity to estimates of soil water content, *Soil Science Society of America Journal*, 60(1), 35-41.

Igel, J., G. Kurz, and R. Schulz (2006), Detecting brine zones in salt deposits with the ground penetrating radar (GPR) for safety assessments of underground waste disposals, *Near Surface Geophysics*, 4(4), 265-274.

Jones, S. B., and S. P. Friedman (2000), Particle shape effects on the effective permittivity of anisotropic or isotropic media consisting of aligned or randomly oriented ellipsoidal particles, *Water Resources Research*, 36(10), 2821-2833, doi:10.1029/2000wr900198.

Josh, M., L. Esteban, C. Delle Piane, J. Sarout, D. N. Dewhurst, and M. B. Clennell (2012), Laboratory characterisation of shale properties, *Journal of Petroleum Science and Engineering*, 88-89, 107-124, doi:10.1016/j.petrol.2012.01.023.

Kaatze, U., and Y. Feldman (2006), Broadband dielectric spectrometry of liquids and biosystems, *Measurement Science & Technology*, 17(2), R17-R35, doi:10.1088/0957-0233/17/2/r01.

Kata, K., and Y. Shimada (1992), Low dielectric-constant glass ceramic composite controlled isolated porosity, *Nippon Seramikkusu Kyokai Gakujutsu Ronbunshi-Journal of the Ceramic Society of Japan*, 100(4), 570-576.

Khanna, R. K., and J. Sobhanad (1972), Dielectric properties of lithium sulfate at radio and microwave-frequencies, *Physica Status Solidi a-Applied Research*, 12(1), 225-&, doi:10.1002/pssa.2210120124.

Kingery, W. D., H. K. Bowen, and D. R. Uhlmann (1976), *Introduction to ceramics*, John Wiley & Sons Ltd.

Knoll, M. D. (1996), A petrophysical basis for ground-penetrating radar and very early time electromagnetics, electrical properties of sand-clay mixtures, University of British Columbia, BC, Canada.

Koledintseva, M. Y., S. K. Patil, R. W. Schwartz, W. R. Huebner, N. Konstantin, J. Shen, and J. Chen (2009), Prediction of Effective Permittivity of Diphasic Dielectrics as a Function of Frequency, *Ieee Transactions on Dielectrics and Electrical Insulation*, 16(3), 793-808.

Kovacs, A., and R. M. Morey (1978), Radar anisotropy of sea ice due to preferred azimuthal orientation of the horizontal c axes of ice crystals, *Journal of Geophysical Research: Oceans (1978–2012)*, 83(C12), 6037-6046.

Krupka, J. (2006), Frequency domain complex permittivity measurements at microwave frequencies, *Measurement Science & Technology*, 17(6), R55-R70.

Kulenkampff, J. M., and U. Yaramanci (1993), Frequency-Dependent Complex Resistivity of Rock-Salt Samples and Related Petrophysical Parameters, *Geophysical Prospecting*, 41(8), 995-1008.

Lichtenecker, K., and K. Rother (1931), The derivation of the logarithmic compound law from general principles of the stationary current, *Physikalische Zeitschrift*, 32, 255-260.

Looyenga, H. (1965), Dielectric Constants of Heterogeneous Mixtures, *Physica*, 31(3), 401-406.

- Lowndes, R. P. (1966), Temperature Dependence of Static Dielectric Constant of Alkali Silver and Thallium Halides, *Physics Letters*, 21(1), 26-&.
- Malicki, M. A., R. Plagge, and C. H. Roth (1996), Improving the calibration of dielectric TDR soil moisture determination taking into account the solid soil, *Eur. J. Soil Sci.*, 47(3), 357-366.
- Martinez, A., and A. P. Brynes (2001), *Modeling Dielectric-constant Values of Geologic Materials: An Aid to Ground-penetrating Radar Data Collection and Interpretation*, Kansas Geological Survey.
- Martinez, A., and A. P. Brynes (2001), Modeling Dielectric-constant Values of Geologic Materials: An Aid to Ground-penetrating Radar Data Collection and Interpretation, *Kansas Geological Survey, Bulletin 247, part 1*.
- Matsuoka, T., S. Fujita, S. Morishima, and S. Mae (1997), Precise measurement of dielectric anisotropy in ice Ih at 39 GHz, *Journal of Applied Physics*, 81(5), 2344-2348.
- Mattei, E., A. De Santis, A. Di Matteo, E. Pettinelli, and G. Vannaroni (2007), Effective frequency and attenuation measurements of glass beads/magnetite mixtures by time-domain reflectometry, *Near Surface Geophysics*, 5(1), 77-82.
- Mattei, E., A. Santis, A. Di Matteo, E. Pettinelli, and G. Vannaroni (2008), Electromagnetic Parameters of Dielectric and Magnetic Mixtures Evaluated by Time-Domain Reflectometry, *IEEE Geosci. Remote Sens. Lett.*, 5(4), 730-734.
- Matzler, C. (1998), Microwave permittivity of dry sand, *Ieee Transactions on Geoscience and Remote Sensing*, 36(1), 317-319.
- Mdarhrj, A., F. Carmona, and M. E. Achour (2008), Modelling of the dielectric response of heterogeneous media constituted by conductive particles in an insulating epoxy polymer, *Annales De Chimie-Science Des Materiaux*, 33(2), 87-96.
- Milner, K. R., and C. E. Dunn (2004), Prairie Evaporite, in *Lexicon of Canadian Stratigraphy, Volume 4: western Canada including eastern British Columbia, Alberta, Saskatchewan, and southern Manitoba*, edited by D. J. Glass, Canadian Society of Petroleum Geologists.

- Mohr, P. J., B. N. Taylor, and D. B. Newell (2008), CODATA recommended values of the fundamental physical constants: 2006, *Reviews of Modern Physics*, 80(2), 633-730, doi:10.1103/RevModPhys.80.633.
- Mossman, D. J., R. N. Delabio, and A. D. Mackintosh (1982), Mineralogy Of Clay Marker Seams In Some Saskatchewan Potash Mine, *Canadian Journal of Earth Sciences*, 19(11), 2126-2140, doi:10.1139/e82-187.
- Myroshnychenko, V., and C. Brosseau (2005), Finite-element modeling method for the prediction of the complex effective permittivity of two-phase random statistically isotropic heterostructures, *Journal of Applied Physics*, 97(4), doi:10.1063/1.1835544.
- Neelakanta, P. S. (1995), *Handbook of electromagnetic materials : monolithic and composite versions and their applications*, Boca Raton [u.a.] : CRC Press.
- Nelson, S., D. Lindroth, and R. Blake (1989), Dielectric-Properties of Selected and Purified Minerals at 1 to 22 Ghz, *Journal of Microwave Power and Electromagnetic Energy*, 24(4), 213-220.
- Nelson, S. O. (1983), Observations on the Density Dependence of Dielectric-Properties of Particulate Materials, *Journal of Microwave Power and Electromagnetic Energy*, 18(2), 143-152.
- Nelson, S. O. (1994), Measurement of Microwave Dielectric-Properties of Particulate Materials, *Journal of Food Engineering*, 21(3), 365-384.
- Nelson, S. O. (2001), Measurement and calculation of powdered mixture permittivities, *Ieee Transactions on Instrumentation and Measurement*, 50(5), 1066-1070, doi:10.1109/19.963159.
- Nelson, S. O. (2005), Density-permittivity relationships for powdered and granular materials, *Ieee Transactions on Instrumentation and Measurement*, 54(5), 2033-2040, doi:10.1109/tim.2005.853346.
- Nelson, S. O., and P. G. Bartley (1998), Open-ended coaxial-line permittivity measurements on pulverized materials, *Ieee Transactions on Instrumentation and Measurement*, 47(1), 133-137.
- Olhoeft, G. R. (1981), Electrical properties of rocks, in *Physical properties of Rocks and Minerals*

edited by Y. S. Touloukian, W. R. Judd and R. F. Roy, p. 298, McGraw-Hill, New York.

Olhoeft, G. R., and D. W. Strangway (1975), Dielectric properties of first 100 meters of moon., *Earth and Planetary Science Letters*, 24(3), 394-404, doi:10.1016/0012-821x(75)90146-6.

Or, D., and J. M. Wraith (1999), Temperature effects on soil bulk dielectric permittivity measured by time domain reflectometry: A physical model, *Water Resources Research*, 35(2), 371-383, doi:10.1029/1998wr900008.

Parkhomenko, E. I. (2012), *Electrical Properties of Rocks*, Springer US.

Pascal, H., F. Pascal, and D. Rankin (1981), Attenuation and dispersion of electromagnetic-waves in fluid-saturated porous rocks and applications to dielectric-constant well logging, *Geophysics*, 46(4), 415-415.

Payne, D. (1973), The Role of Internal Boundaries upon the Dielectric properties of Polycrystalline Ferroelectric Materials, The Pennsylvania State University, USA.

Pepin, S., N. J. Livingston, and W. R. Hook (1995), Temperature-dependent measurement errors in time-domain reflectometry determinations of soil-water, *Soil Science Society of America Journal*, 59(1), 38-43.

Powers, M. H. (1997), Modeling frequency-dependent GPR, *U. S. Geological Survey the leading edge*, 16 (11), 1657-1662.

Rawlins, C. (2000), Basic AC Circuits, edited, Newnes.

Reynolds, J. A., and J. M. Hough (1957), Formulae for Dielectric Constant of Mixtures, *Proceedings of the Physical Society of London Section B*, 70(8), 769-775.

Robinson, D. A., J. P. Bell, and C. H. Batchelor (1994), Influence of Iron Minerals on the Determination of Soil-Water Content Using Dielectric Techniques, *Journal of Hydrology*, 161(1-4), 169-180.

Robinson, D. A., and S. P. Friedman (2003), A method for measuring the solid particle permittivity or electrical conductivity of rocks, sediments, and granular materials, *Journal of Geophysical Research-Solid Earth*, 108(B2), doi:10.1029/2001jb000691.

Robinson, D. A., and S. P. Friedman (2005), Electrical conductivity and dielectric permittivity of sphere packings: Measurements and modelling of cubic lattices, randomly packed monosize

spheres and multi-size mixtures, *Physica a-Statistical Mechanics and Its Applications*, 358(2-4), 447-465.

Robinson, D. A., S. B. Jones, J. M. Wraith, D. Or, and S. P. Friedman (2003), A Review of Advances in Dielectric and Electrical Conductivity Measurement in Soils Using Time Domain Reflectometry, *Vadose Zone Journal*, 2(4), 444-475.

Roth, C. H., M. A. Malicki, and R. Plagge (1992), Empirical-Evaluation of the Relationship between Soil Dielectric-Constant and Volumetric Water-Content as the Basis for Calibrating Soil-Moisture Measurements by Tdr, *Journal of Soil Science*, 43(1), 1-13.

Rust, A. C., J. K. Russell, and R. J. Knight (1999), Dielectric constant as a predictor of porosity in dry volcanic rocks, *Journal of Volcanology and Geothermal Research*, 91(1), 79-96.

Saarenketo, T. (1998), Electrical properties of water in clay and silty soils, *Journal of Applied Geophysics*, 40(1-3), 73-88, doi:10.1016/s0926-9851(98)00017-2.

Sakaki, T., K. Sugihara, T. Adachi, K. Nishida, and W. R. Lin (1998), Application of time domain reflectometry to determination of volumetric water content in rock, *Water Resources Research*, 34(10), 2623-2631, doi:10.1029/98wr02038.

Sastry, S. S., G. Satyanandam, A. Subrahmanyam, and V. R. K. Murphy (1988), Dielectric Properties of HgCl<sub>2</sub>:2KCl:H<sub>2</sub>O Single Crystals in the Radio Frequency Region *phys. stat. sol.*, 105( K71).

Schey, H. M., and H. M. Schey (2005), *DIV, Grad, Curl, and All That: An Informal Text on Vector Calculus*, 4th Revised edition edition ed., W W Norton & Co Inc (Np).

Sen, P. N., C. Scala, and M. H. Cohen (1981), A self-similar model for sedimentary-rocks with application to the dielectric-constant of fused glass-beads, *Geophysics*, 46(5), 781-795, doi:10.1190/1.1441215.

Senseny, P. E., K. D. Mellegard, and J. D. Nieland (1989), Influence of end effects on the deformation of salt, *International Journal of Rock Mechanics and Mining Sciences & Geomechanics Abstracts*, 26(5), 435-444, doi:10.1016/0148-9062(89)90939-x.

- Sihvola, A. (2013), Homogenization principles and effect of mixing on dielectric behavior, *Photonics and Nanostructures-Fundamentals and Applications*, 11(4), 364-373, doi:10.1016/j.photonics.2013.01.004.
- Sihvola, A. H. (1989), Self-consistency aspects of dielectric mixing theories, *Ieee Transactions on Geoscience and Remote Sensing*, 27(4), 403-415.
- Sihvola, A. H. (1999), *Electromagnetic Mixing Formulas and Applications*, IEEE Publishing, London, UK.
- Sivhola, A. H. (2002), How strict are theoretical bounds for dielectric properties of mixtures?, *IEEE Trans. Geosci. Rem. Sens.*, 40(4), 880- 886.
- Skierucha, W., R. Walczak, and A. Wilczek (2004), Comparison of Open-Ended Coax and TDR sensors for the measurement of soil dielectric permittivity in microwave frequencies, *International Agrophysics*, 18(4), 355-362.
- Spanoudaki, A., and R. Pelster (2001), Effective dielectric properties of composite materials: The dependence on the particle size distribution, *Physical Review B*, 64(6), doi:10.1103/PhysRevB.64.064205.
- Stuchly, M. A., and S. S. Stuchly (1980), Coaxial line reflection methods for measuring dielectric-properties of biological substances at radio and microwave-frequencies - a review, *Ieee Transactions on Instrumentation and Measurement*, 29(3), 176-183, doi:10.1109/tim.1980.4314902.
- Sun, Z. J., G. D. Young, R. A. McFarlane, and B. M. Chambers (2000), The effect of soil electrical conductivity on moisture determination using time-domain reflectometry in sandy soil, *Canadian Journal of Soil Science*, 80(1), 13-22.
- Sylvie, T. (1994), Radar experiments in isotropic and anisotropic geological formations (granite and schists), *Geophysical Prospecting*, 42(6), 615-636.
- Thierbac, R. (1974), Electromagnetic Reflections in Salt Deposits, *Journal of Geophysics-Zeitschrift Fur Geophysik*, 40(5), 633-637.



- Topp, G. C., J. L. Davis, and A. P. Annan (1980), Electromagnetic determination of soil-water content - measurements in coaxial transmission-lines, *Water Resources Research*, 16(3), 574-582, doi:10.1029/WR016i003p00574.
- Ulaby, F. T., E. Michielssen, and U. Ravaioli (2010), *Fundamentals of Applied Electromagnetics*, 6th edition ed., Prentice Hall.
- Unterberger, R. R. (1978), Radar Propagation in Rock Salt, *Geophysical Prospecting*, 26(2), 312-328.
- van Beck, L. K. H. (1967), *Dielectric behavior of heterogeneous systems*, J.B. Birks, ed., London, UK, Heywood Books,.
- Van Dam, R. L., W. Schlagerz, M. J. Dekkers, and J. A. Huisman (2002), Iron oxides as a cause of GPR reflections, *Geophysics*, 67(2), 536-545.
- vonHippel, A. R. (1954), *Dielectric materials and applications*, Artech House.
- vonHippel, A. R., and A. S. Labounskyl (1995), *Dielectric Materials and Applications*, Artech House.
- Wang, J. R., and T. J. Schmugge (1980), An empirical-model for the complex dielectric permittivity of soils as a function of water-content, *Ieee Transactions on Geoscience and Remote Sensing*, 18(4), 288-295, doi:10.1109/tgrs.1980.350304.
- Weast, R. C. (1984), *Handbook of physics and chemistry*, CRC Press, Boca Ratoon FL.
- Whalley, W. R. (1993), Considerations on the use of time-domain reflectometry (TDR) for measuring soil-water content, *Journal of Soil Science*, 44(1), 1-9.
- Wharton, R. P., R. N. Rau, and D. L. Best (1980), Electromagnetic propagation logging—Advances in technique and interpretation, in *SPE Annual Technical Conference and Exhibition*, edited, Society of Petroleum Engineers, Dallas, Texas.
- Widjajakusuma, J., and B. H. Biswal, R. (2003), Quantitative comparison of mean field mixing laws for conductivity and dielectric constants of porous media, *Physica a-Statistical Mechanics and Its Applications*, 318(3-4), 319-333.
- Young, K. F., and H. P. R. Frederikse (1973), Compilation of the Static Dielectric Constant of Inorganic Solids, *J. Phys. Chem. Ref. Data*, 2(2).

Zakri, T., J. P. Laurent, and M. Vauclin (1998), Theoretical evidence for 'Lichtenecker's mixture formulae' based on the effective medium theory, *Journal of Physics D-Applied Physics*, 31(13), 1589-1594, doi:10.1088/0022-3727/31/13/013.

Zasetsky, A. Y., and I. M. Svishchev (2001), Dielectric response of concentrated NaCl aqueous solutions: Molecular dynamics simulations, *Journal of Chemical Physics*, 115(3), 1448-1454, doi:10.1063/1.1381055.

## **Appendix A**

### **A1: Cole-Cole plot for the eight cold compressed different depth samples**

Fig. A-1 and Fig. A-2 are representing the Cole-Cole plots for eight cold compressed samples that were from different depths of Rocanville potash mine. The list of samples, depth ranges, dielectric permittivity values can be found in Table 5-2 and Fig. 5-8 in chapter 5. From Fig. (A-1, A-2) we can find that none of the eight samples were fitting properly with the circles. Therefore it is not possible to explain the experimental results of the samples by Cole-Cole assumption.

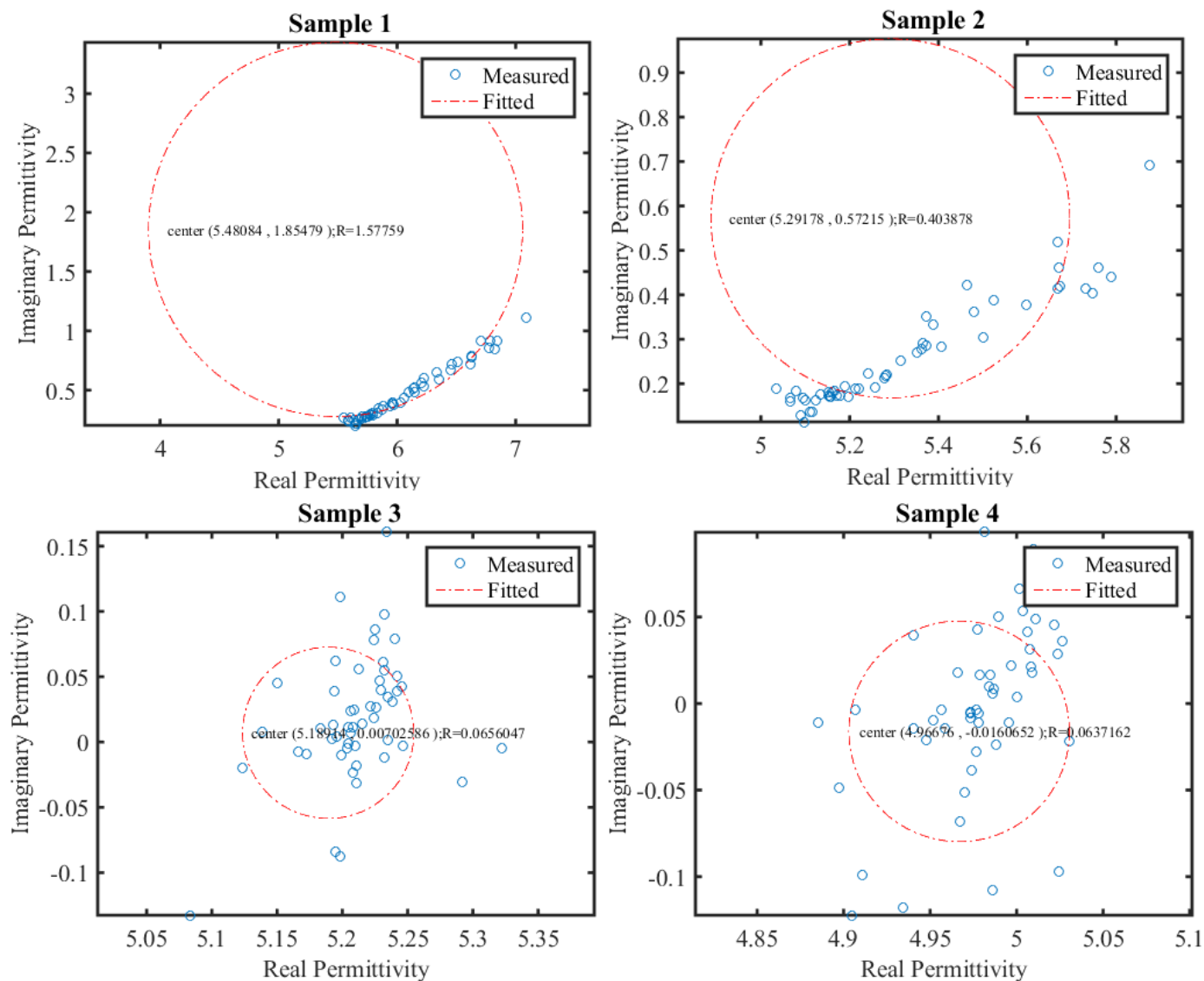


**Figure A-1 Cole-Cole plots for four of the eight different depth samples (samples are listed in Table 5-2). All the samples were prepared by cold compress technique.**

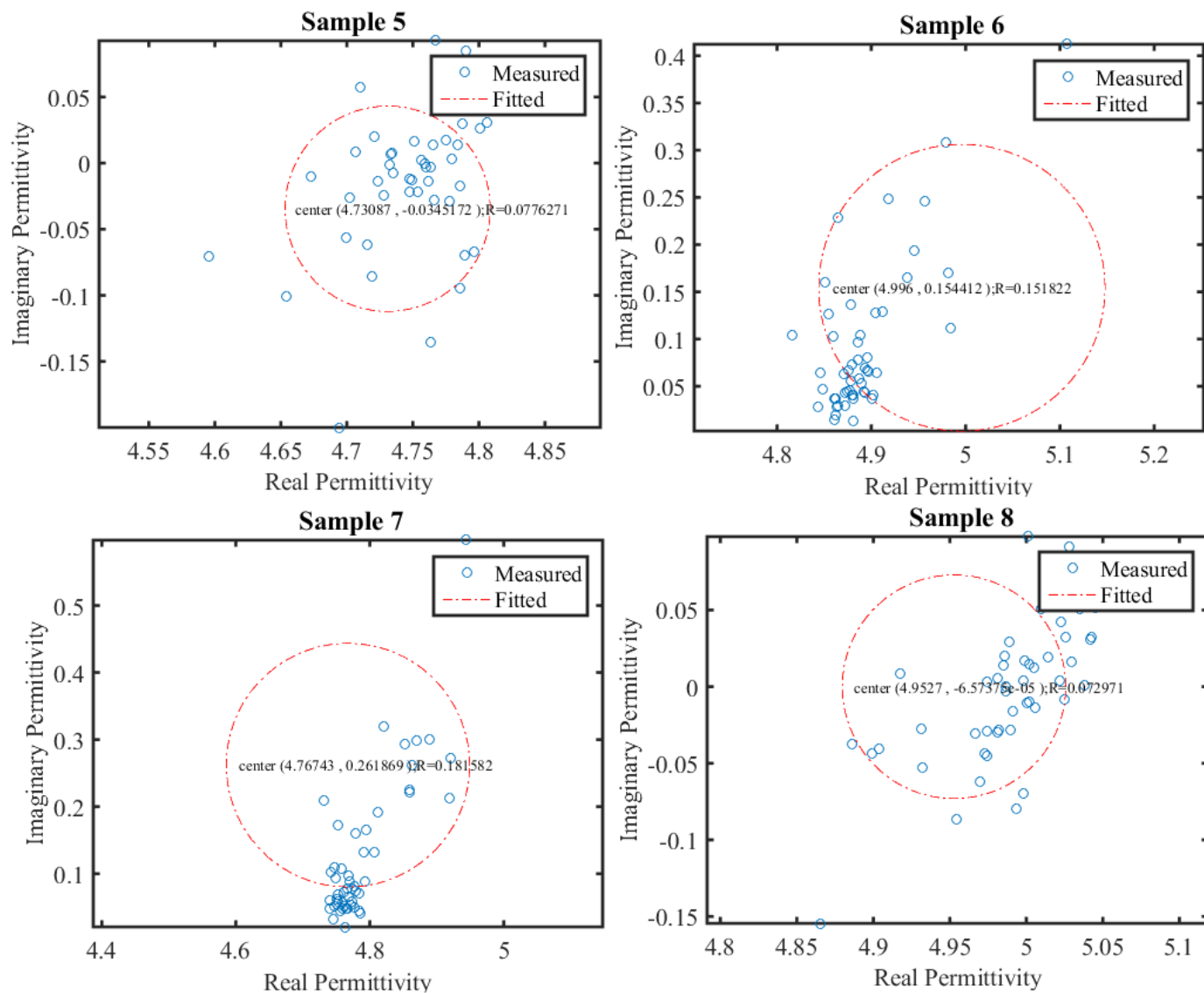


**Figure A-2 Cole-Cole plots for four of the eight different depth samples (samples are listed in Table 5-2). All the samples were prepared by cold compress technique.**

## **A2: Cole-Cole plot for the fourteen raw potash samples**

Figs. (A-3, A-4, A-5, A-6) below are the Cole-Cole plots of the fourteen raw potash core samples. All of these 14 samples were obtained from a single short piece of core. A list of the samples, and dielectric permittivity values could be found in Table 5-1 and Fig. 5-4. From the Cole-Cole plots we found that none of the raw potash samples matched with the circle except the sample 7 showed a better fit. We presumed that sample 7 had a relatively higher imaginary permittivity than the other samples.

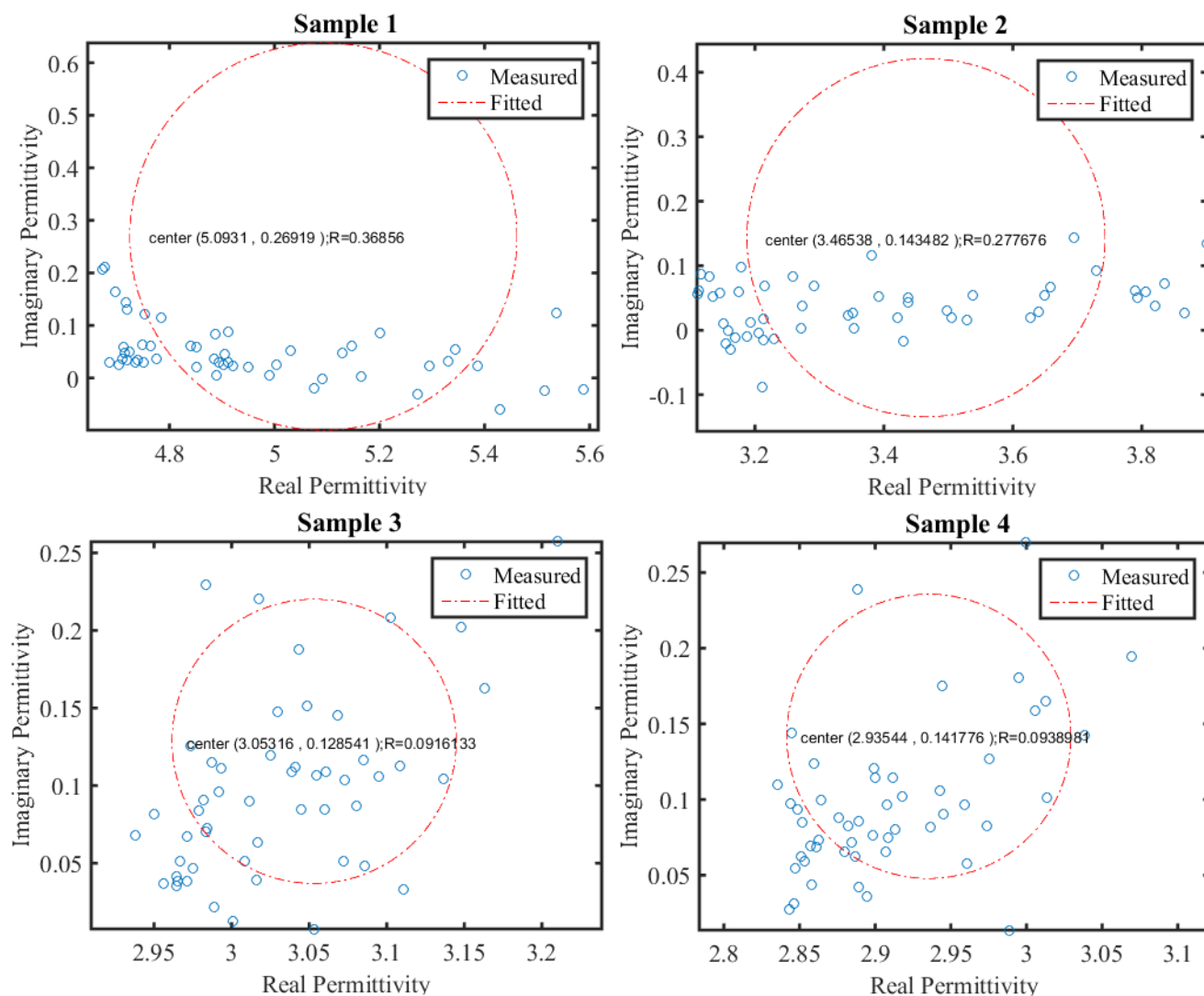


**Figure A-3 Cole-Cole plots for four of the fourteen raw potash samples (samples are listed in table 5-1 and Fig. 5-4). Dielectric measurements were done by placing the samples directly on the sensor.**

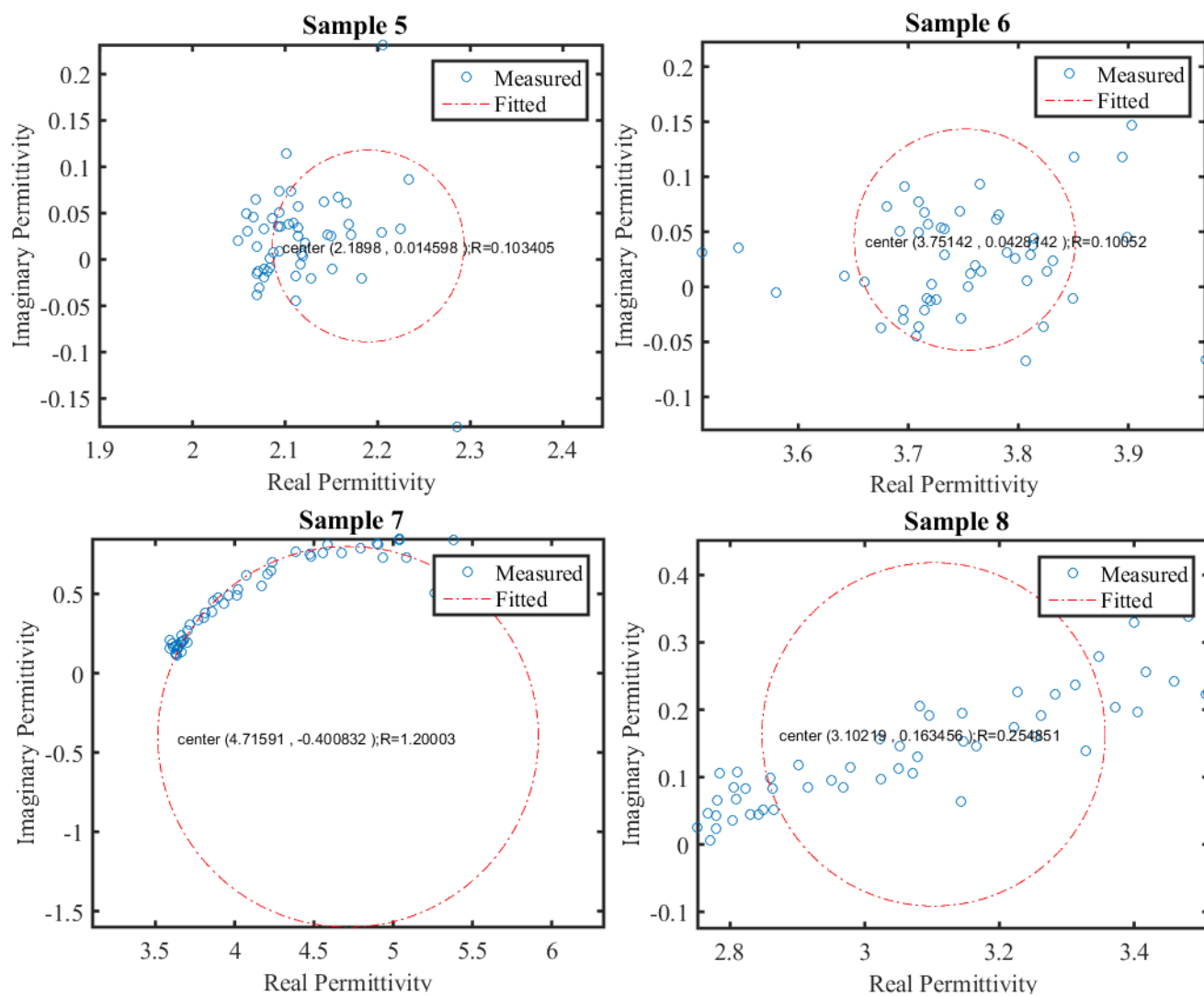


**Figure A-4 Cole-Cole plots for four of the fourteen raw potash samples (samples are listed in table 5-1 and Fig. 5-4). Dielectric measurements were done by placing the samples directly on the sensor.**



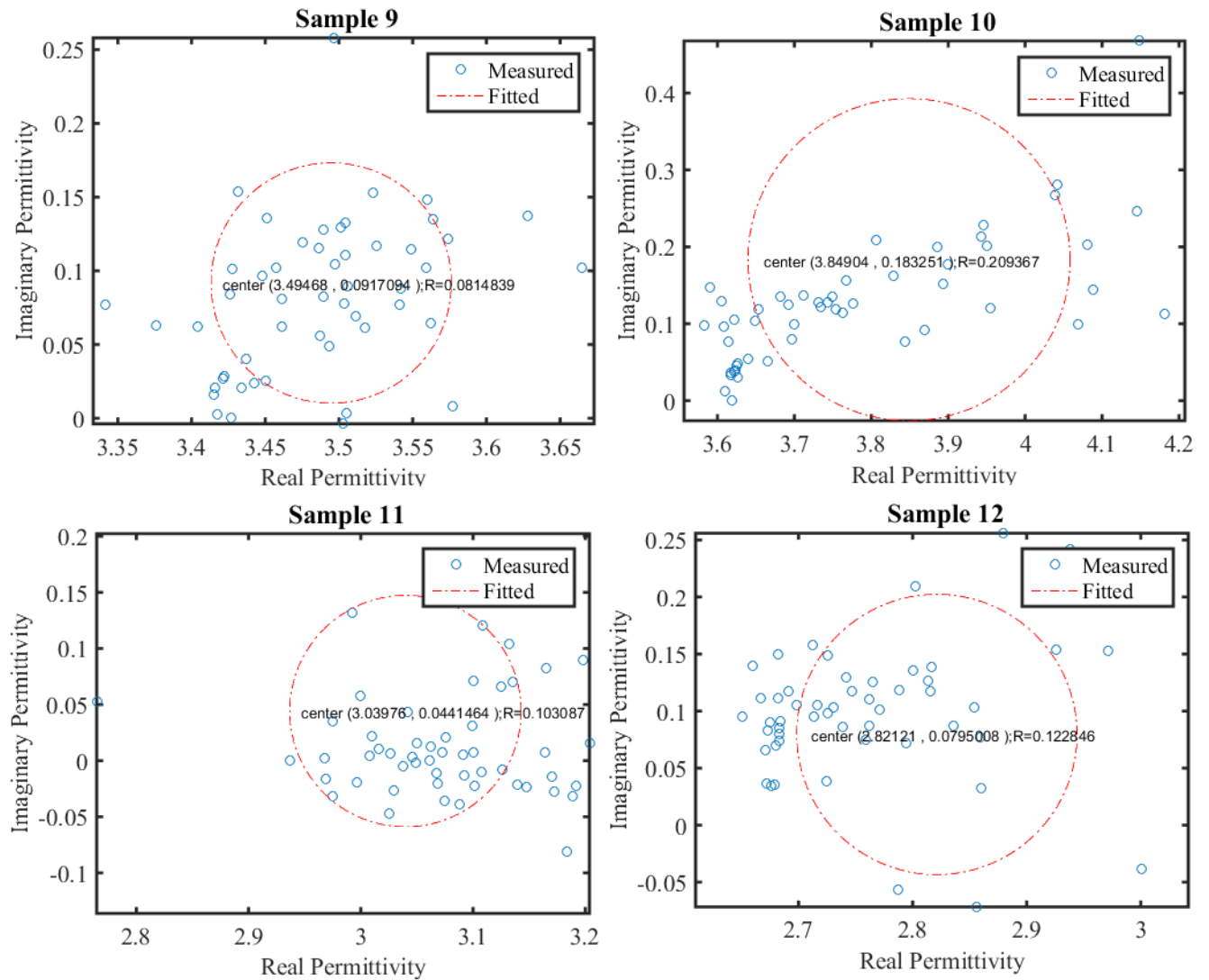


**Figure A-5 Cole-Cole plots for four of the fourteen raw potash samples (samples are listed in table 5-1 and Fig. 5-4). Dielectric measurements were done by placing the samples directly on the sensor.**

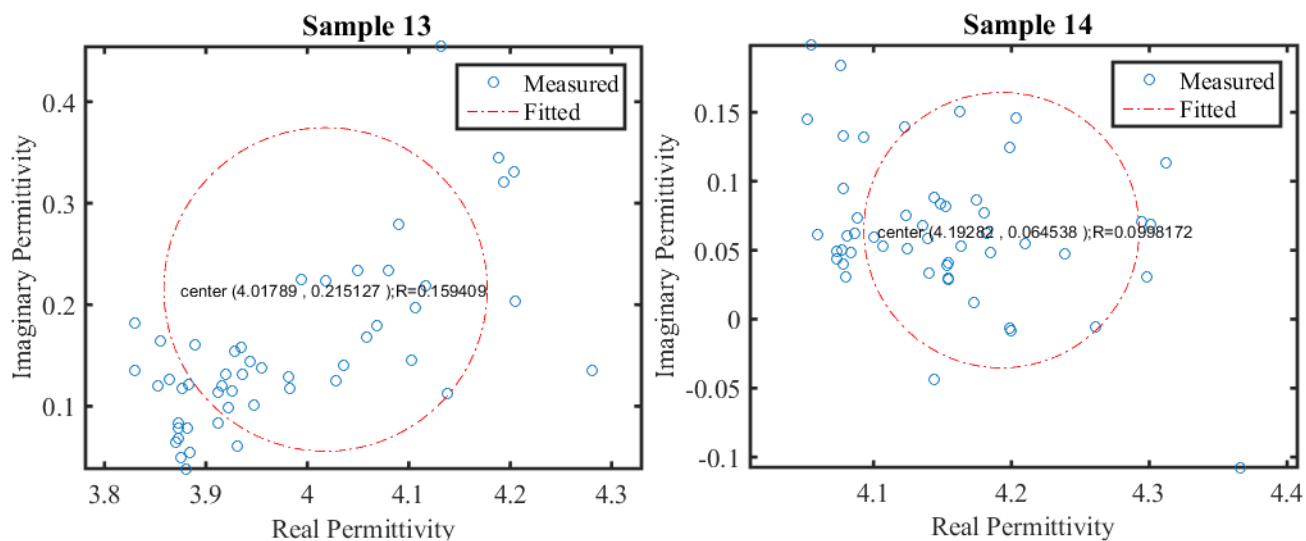


**Figure A-6 Cole-Cole plots for two of the fourteen raw potash samples (samples are listed in table 5-1 and Fig. 5-4). Dielectric measurements were done by placing the samples directly on the sensor.**

### **A3: Cole-Cole plot for the fourteen cold compressed core samples**

Fig. (A-7, A-8, A-9, A-10) are the Cole-Cole plots of the fourteen cold compressed potash core samples. All the samples were prepared using cold compressed technique. A list of the samples, and dielectric permittivity values could be found in table 5-1 and Fig. 5-5. From the Cole-Cole plots it is found that none of those samples matched with the circle which turns out that our measurement results could not be explained by Cole-Cole assumption.

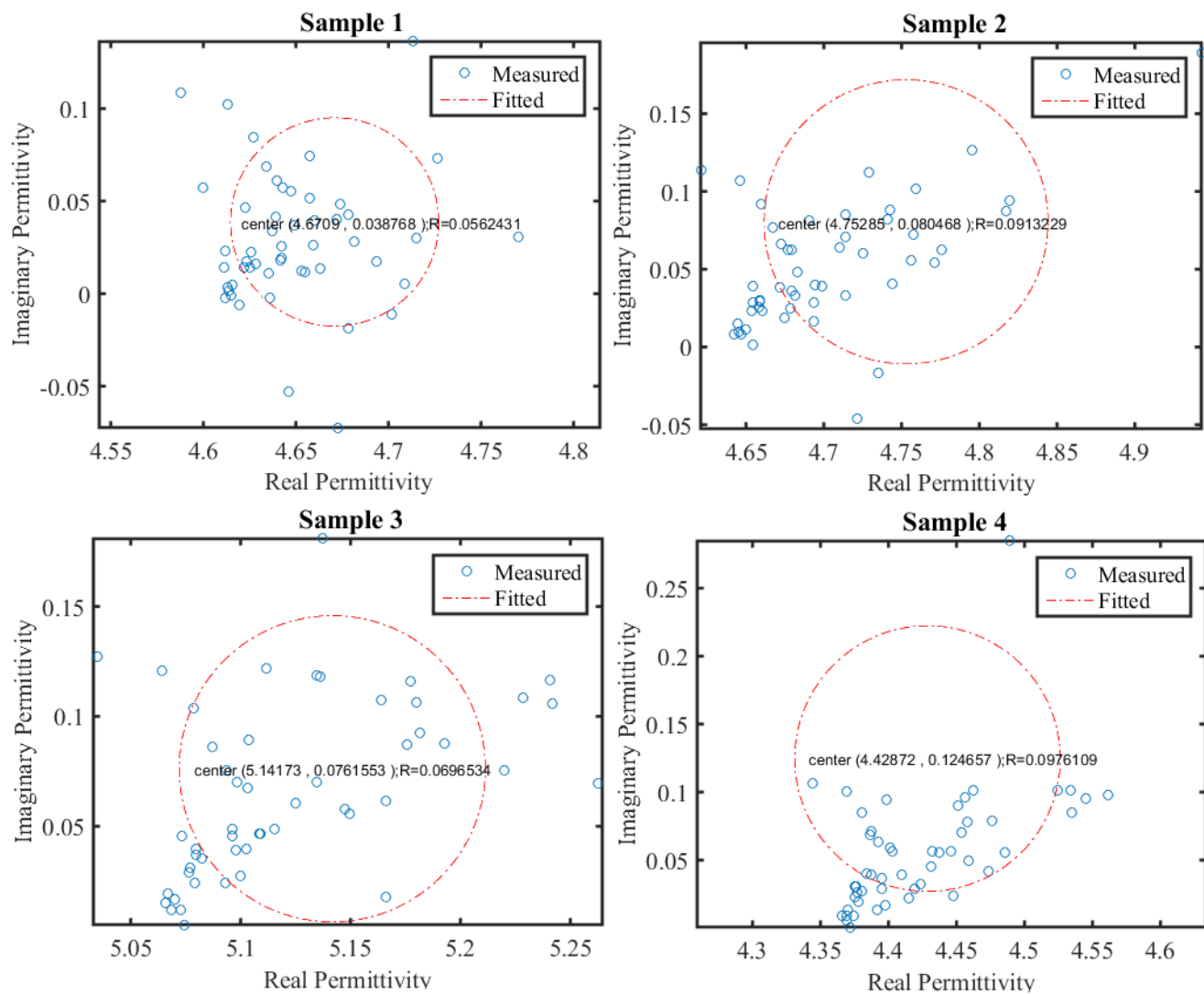


**Figure A-7 Cole-Cole plots for four of the fourteen cold compressed potash samples (samples are listed in table 5-1 and Fig. 5-5).**

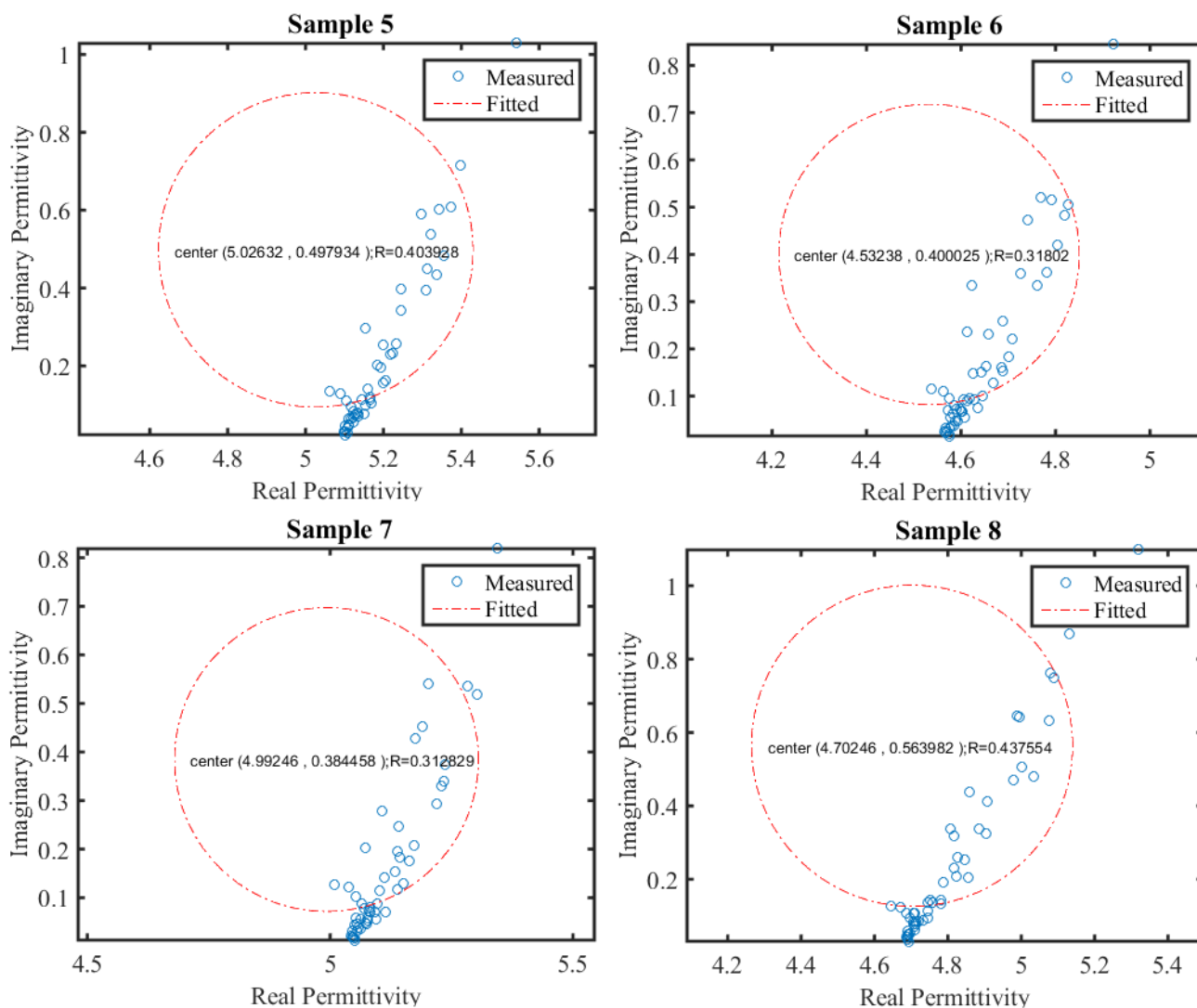


**Figure A-8 Cole-Cole plots for four of the fourteen cold compressed potash samples (samples are listed in table 5-1 and Fig. 5-5).**

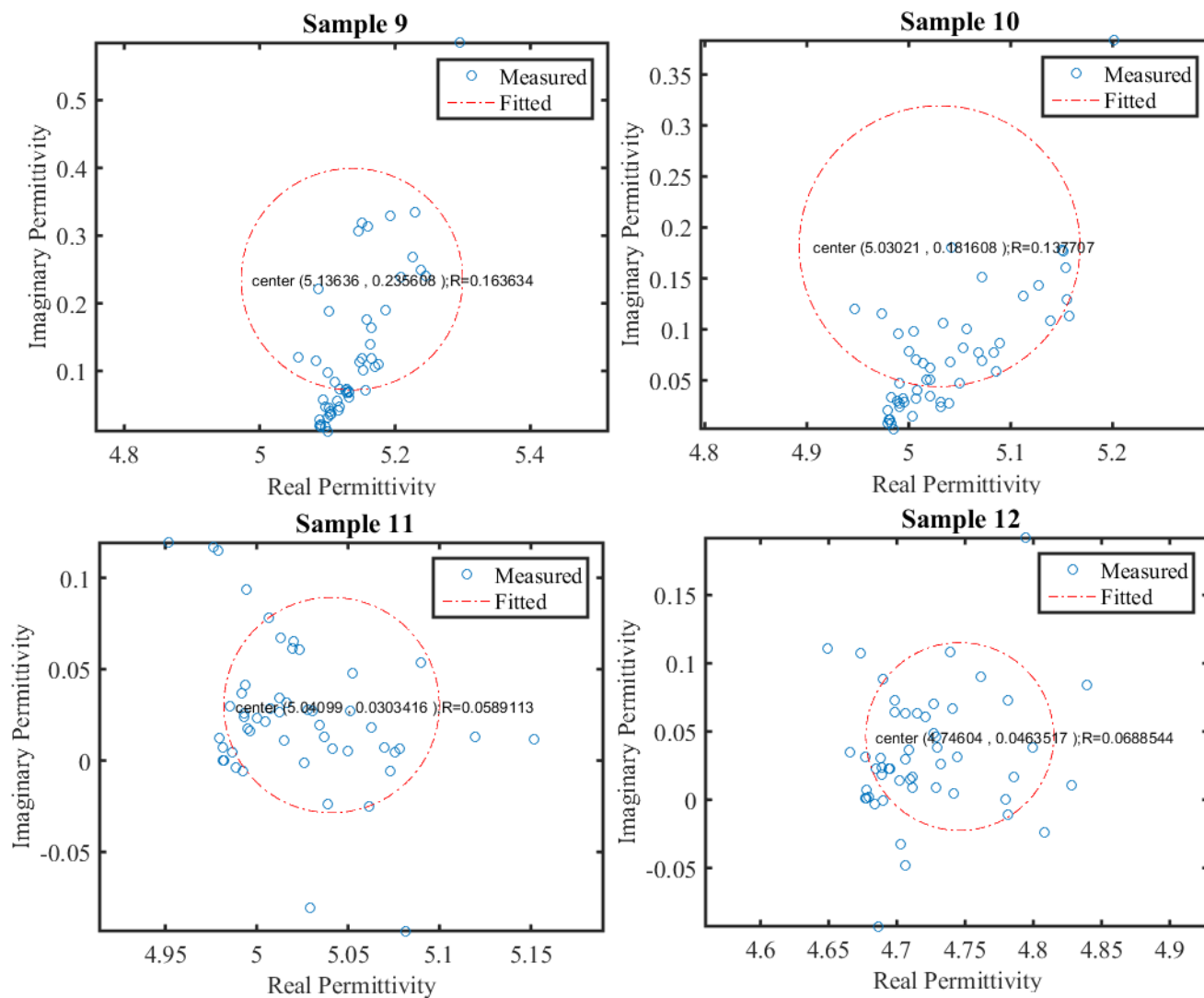


**Figure A-9 Cole-Cole plots for four of the fourteen cold compressed potash samples (samples are listed in table 5-1 and Fig. 5-5).**

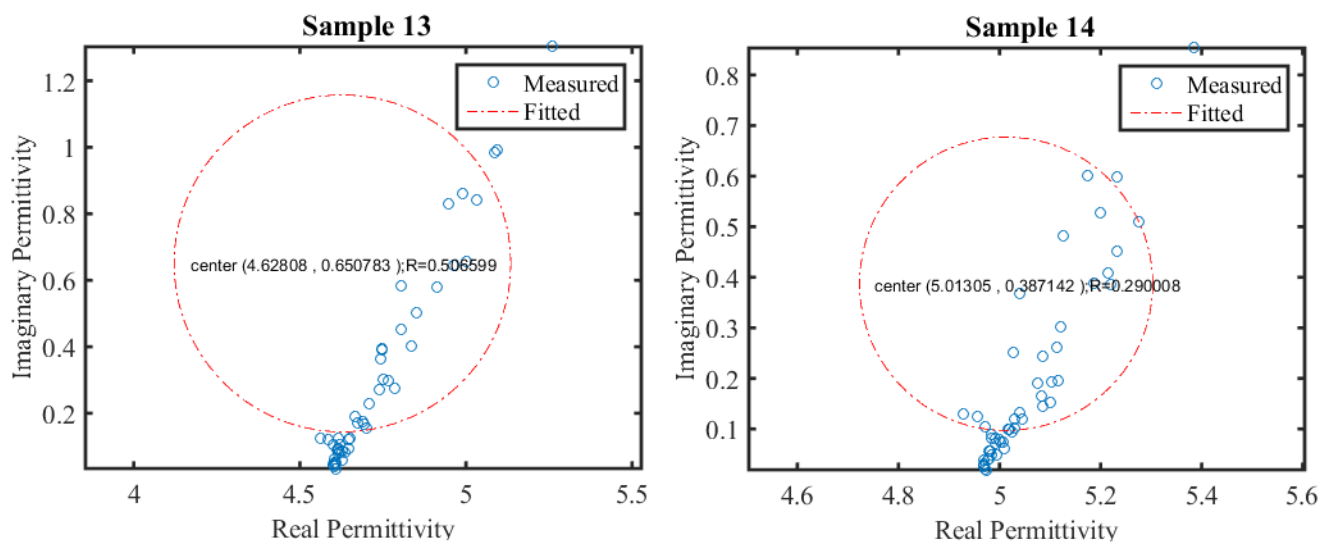


**Figure A-10 Cole-Cole plots for two of the fourteen cold compressed potash samples (samples are listed in Table 5-1 and Fig. 5-5).**

#### A4: Cole-Cole plot for the Halite and sylvite crystals

Fig. A-11 represents the Cole-Cole plots for halite and sylvite single crystals. The dielectric real and imaginary permittivity values of these single crystals could be found from Fig. 3-5. From the Cole-Cole plot it is found that none of the single crystals matched with the circle.

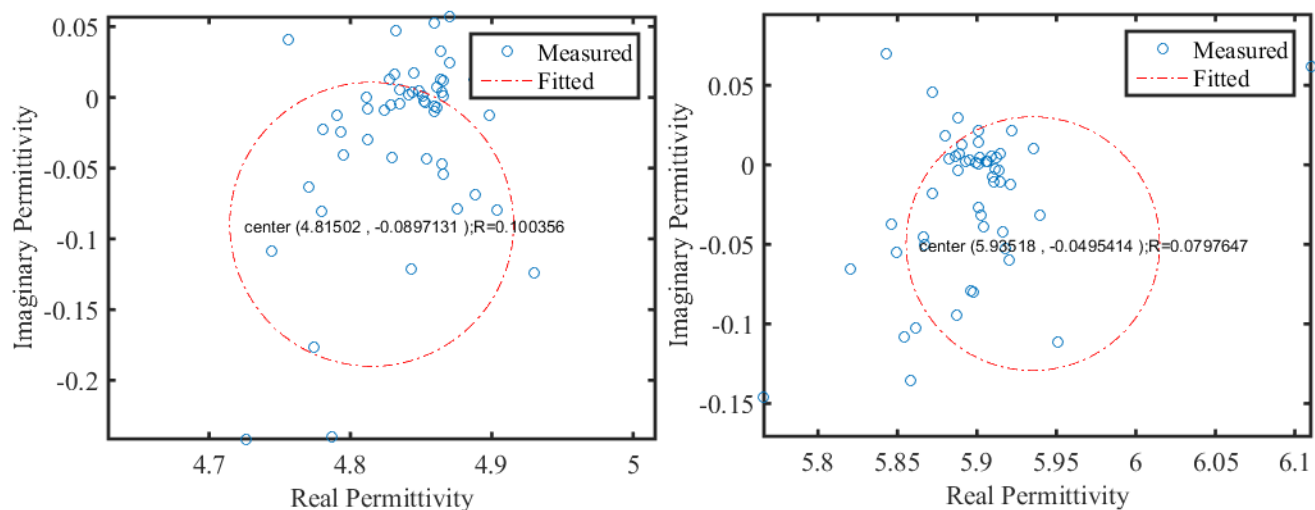


**Figure A-11 Cole-Cole plots for NaCl and KCl single crystals. Dielectric permittivity values could be found from Fig. 3-5.**



## Appendix B

### MATLAB code for mixing theories

```
% For porous KCl with experimental values
clear all;
%close all
e1 = 1; e2 = 4.85;
% e1=5.96; e2=80;
% e1=4.85; e2=5.96;
phi1 = 0:0.01:1;
phi2 = 1 - phi1;

Wiener1 = e1*phi1 + e2*phi2;
Wiener2 = [phi1/e1 + phi2/e2].^(-1);

HS1 = e1 + phi2./(1/(e2-e1)+phi1/(3*e1));
HS2 = e2 + phi1./(1/(e1-e2)+phi2/(3*e2));

up = 2*(1-phi2)*e1+(1+2*phi2)*e2;
down = (2+phi2)*e1+(1-phi2)*e2;
MaxGar = e1*(up./down);

beta = (3*phi1-1)*e1 + (3*phi2-1)*e2; %(see page 13 of Choy - Effective
medium book
Bruggeman = 0.25*(beta + (beta.^2 + 8*e1*e2).^(0.5));

LLL = (phi2*e2^(1/3)+phi1*e1^(1/3)).^3;
CRIM = (phi2*e2^(1/2)+phi1*e1^(1/2)).^2;

Lichtenecker = exp(phi1*log(e1)+phi2*log(e2));

for i = 1:length(phi1)
    f = @(x)((e1-x)/(e1-e2))*(e2^0.333333)*((1./x).^(0.333333333))-phi2(i)
    Sen(i) = fzero(f,[e2+0.001 e1-0.001]);

    f = @(x)((x-e2)./(x+2*e2))-phi1(i)*(e1-e2)/(e1+2*e2)
    CMLL(i) = fzero(f,[e2 e1]);
end
%set(gca,'LineWidth',1.5,'FontSize',16,'FontName','TimesNewRoman');grid on;
set(0,'defaultAxesFontName','Times New Roman');
```

```

set(0,'defaultTextFontName','Times New Roman');
set(gca,'FontName','Times New Roman','FontSize',16,'LineWidth',2);

figure(1);
plot(phil,Wiener1,'-b',phil,Wiener2,'-r',phil,HS1,'-g',phil,HS2,'-.k',...
    phil,MaxGar,'-m',phil,Bruggeman,'-.r',phil,Lichtenecker,'-
c',phil,CRIM,...
    '-k',phil,LLL,'-k',phil,Sen,'--r',phil,CMLL,'-y','LineWidth',2)
% legend('Wiener High','Wiener Low','HS1','HS2','Maxwell-
Garnett','Bruggemann','Lichtenecker','CRIM','LLL','Sen','CMLL')
grid on
junk = axis;
junk(3) = 0; junk(4) = max([e1 e2])*1.05; junk(2) = 0.1; axis(junk)
xlabel('Fractional Pore Volume','FontName','Times New
Roman','FontSize',16),...
    ylabel('Effective Relative Permittivity','FontName','Times New
Roman','FontSize',16)
ylim([3.5,5])
% experimental results
%por = [3.06; 4.02; 3.56; 5.12; 5.35; 6.8; 1.78; 8.04]/100; % porosity
porM = [0.0307;0.0404;0.0358;0.0511;0.0526;0.0679;0.0031;0.0808];
porSD = [0.0010;0.0009;0.0010;0.0019;0.0016;0.0014;0.0049;0.0027;];
permtM = [4.530;4.483;4.585;4.515;4.536;4.211;4.782;3.989;];
permtSD = [0.024;0.053;0.053;0.043;0.041;0.069;0.056;0.053];
% permt = [4.53; 4.48; 4.5; 4.51; 4.53; 4.21; 4.78; 4]; % permittivity
hold on;
errorbarxy(porM,permtM,porSD,permtSD,{'ko','b','r'});
set(gca,'LineWidth',2);
x = porM; y = permtM;

hold on;
coeffs = polyfit(x, y, 1);
% Get fitted values
fittedX = linspace(min(x), max(x), 200);
fittedY = polyval(coeffs, fittedX);
% Plot the fitted line
hold on;
plot(fittedX, fittedY, '--g', 'LineWidth', 1.5);
%plot(por,permt,'*');
legend('Wiener^+','Wiener^-','HS^+','HS^-','Maxwell-
Garnett','Bruggemann','Lichtenecker','CRIM','LLL','Sen','CMLL','Experiment','
Linear Fit')
title('KCl','FontName','Times New Roman','FontSize',16);
set(gca,'FontName','Times New Roman','FontSize',16,'LineWidth',2)

%% For porous NaCl with experimetnal values
clear all;
e1 = 1; e2 = 5.96;
% e1=5.96; e2=80;
% e1=4.85; e2=5.96;
phil = 0:0.01:1;
phi2 = 1 - phil;

Wiener1 = e1*phil + e2*phi2;
Wiener2 = [phil/e1 + phi2/e2].^(-1);

```

```

HS1 = e1 + phi2./(1/(e2-e1)+phi1/(3*e1));
HS2 = e2 + phi1./(1/(e1-e2)+phi2/(3*e2));

up = 2*(1-phi2)*e1+(1+2*phi2)*e2;
down = (2+phi2)*e1+(1-phi2)*e2;
MaxGar = e1*(up./down);

beta = (3*phi1-1)*e1 + (3*phi2-1)*e2; %(see page 13 of Choy - Effective
medium book
Bruggeman = 0.25*(beta + (beta.^2 + 8*e1*e2).^(0.5));

LLL = (phi2*e2^(1/3)+phi1*e1^(1/3)).^3;
CRIM = (phi2*e2^(1/2)+phi1*e1^(1/2)).^2;

Lichtenecker = exp(phi1*log(e1)+phi2*log(e2));

for i = 1:length(phi1)
    f = @(x)((e1-x)/(e1-e2))*(e2^0.333333)*((1./x).^(0.333333333))-phi2(i)
    Sen(i) = fzero(f,[e2+0.001 e1-0.001]);

    f = @(x)((x-e2)./(x+2*e2))-phi1(i)*(e1-e2)/(e1+2*e2)
    CMLL(i) = fzero(f,[e2 e1]);
end
%set(gca,'LineWidth',1.5,'FontSize',16,'FontName','TimesNewRoman');grid on;

figure(2);
set(0,'defaultAxesFontName','Times New Roman');
set(0,'defaultTextFontName','Times New Roman');
set(gca,'FontName','Times New Roman','FontSize',16,'LineWidth',2);
plot(phi1,Wiener1,'-b',phi1,Wiener2,'-r',phi1,HS1,'-g',phi1,HS2,'-.k',...
    phi1,MaxGar,'-m',phi1,Bruggeman,'-.r',phi1,Lichtenecker,'-
c',phi1,CRIM,...
    '-k',phi1,LLL,'-k',phi1,Sen,'--r',phi1,CMLL,'-y','LineWidth',2)
% legend('Wiener High','Wiener Low','HS1','HS2','Maxwell-
Garnett','Bruggemann','Lichtenecker','CRIM','LLL','Sen','CMLL')
grid on
junk = axis;
junk(3) = 0; junk(4) = max([e1 e2])*1.05; junk(2) = 0.1; axis(junk)
xlabel('Fractional Pore Volume','FontName','Times New
Roman','FontSize',16),...
    ylabel('Effective Relative Permittivity','FontName','Times New
Roman','FontSize',16)
ylim([3.5,6])
% experimental results
%por = [3.06; 4.02; 3.56; 5.12; 5.35; 6.8; 1.78; 8.04]/100; % porosity
porM = [0.0299;0.0751;0.0167;0.0511;0.0345;0.0208;0.0415;0.0762;];
porSD = [0.0008;0.0009;0.0019;0.0009;0.0011;0.0006;0.0014;0.0011];
permtM = [5.388;5.234;5.855;5.411;5.638;5.707;5.310;5.515;];
permtSD = [0.122;0.036;0.062;0.026;0.043;0.088;0.042;0.086;];
% permt = [4.53; 4.48; 4.5; 4.51; 4.53; 4.21; 4.78; 4]; % permittivity
x = porM; y = permtM;
hold on
%plot(por,permt,'*');
errorbarxy(porM,permtM,porSD,permtSD,{'ko','b','r'});

```

```

set(gca,'LineWidth',2);
hold on;
coeffs = polyfit(x, y, 1);
% Get fitted values
fittedX = linspace(min(x), max(x), 200);
fittedY = polyval(coeffs, fittedX);
% Plot the fitted line
hold on;
plot(fittedX, fittedY, '--g', 'LineWidth', 1.5);
%plot(por,permt,'*');
legend('Wiener^+', 'Wiener^-', 'HS^+', 'HS^-', 'Maxwell-
Garnett', 'Bruggemann', 'Lichtenecker', 'CRIM', 'LLL', 'Sen', 'CMLL', 'Experiment', '
Linear Fit')
title('NaCl', 'FontName', 'Times New Roman', 'FontSize', 16);
set(gca, 'FontName', 'Times New Roman', 'FontSize', 16, 'LineWidth', 2)

```

## MATLAB code for Cole-Cole plots

```

function [xc,yc,R] = circfit(x,y)
%
% [xc yx R] = circfit(x,y)
%
% fits a circle in x,y plane in a more accurate
% (less prone to ill condition )
% procedure than circfit2 but using more memory
% x,y are column vector where (x(i),y(i)) is a measured point
%
% result is center point (yc,xc) and radius R
% an optional output is the vector of coefficient a
% describing the circle's equation
%
%  $x^2+y^2+a(1)*x+a(2)*y+a(3)=0$ 
%
% By: Izhak bucher 25/oct /1991,
% Modified for Geoph 332 by Doug Schmitt, February 8, 2009
x=x(:); y=y(:);
a=[x y ones(size(x))]\[-(x.^2+y.^2)];
xc = -.5*a(1);
yc = -.5*a(2);
R = sqrt((a(1)^2+a(2)^2)/4-a(3));
%
th = linspace(0,2*pi,360)';
xe = R*cos(th)+xc; ye = R*sin(th)+yc;
plot(x,y,'o',[xe;xe(1)],[ye;ye(1)],'-.r'),
title(' measured and fitted circles')
legend('measured','fitted')
text(xc-R*0.9,yc,sprintf('center (%g , %g );R=%g',xc,yc,R))
xlabel x, ylabel y
axis equal
grid on

```

## MATLAB code for reflection modeling

```
clear all;
close all;
Ref=[0.0332 0.0153 0.0115 0.0117 0.0094 0.0060 0.0140];% reflection
coefficients from data
t = [9.68 19.06 38.05 75.98 151.99 304.06 608.23]; %%% Microsecond
f = 25e06; % frequency in Hz
dt=1/f;
[w, tw]=ricker(f,0.4e-7); % ricker wavelet generated by function 'ricker'
obtained from http://www-geo.phys.ualberta.ca/saig/SeismicLab % Author:
M.D.Sacchi
figure();
set(gca,'FontName','Times New Roman','FontSize',16,'LineWidth',2)
plot (tw*1e6, w);
title('Ricker wavelet')
xlabel('Time (microsec)','FontName','Times New Roman','FontSize',16);
ylabel('Amplitude','FontName','Times New Roman','FontSize',16);

R=zeros(1,length(1:1:ceil(1.01*max(t)*f*1E-06)));
ind=round(t*f*1E-06);
R(ind) = Ref;
S=conv(R,w);
figure();
set(gca,'FontName','Times New Roman','FontSize',16,'LineWidth',2)
x = [1:1:length(S)]./(f*1E-06);
plot(x,S(1:end));
xlabel('Time (microsec)','FontName','Times New Roman','FontSize',16);
ylabel('Amplitude','FontName','Times New Roman','FontSize',16);
figure();
set(gca,'FontName','Times New Roman','FontSize',16,'LineWidth',2)
imagesc(S);
xlabel('Time (microsec)','FontName','Times New Roman','FontSize',16);
ylabel('Amplitude','FontName','Times New Roman','FontSize',16);

figure();
set(gca,'FontName','Times New Roman','FontSize',16,'LineWidth',2)
plot(R);
xlabel('Time (microsec)','FontName','Times New Roman','FontSize',16);
ylabel('Amplitude','FontName','Times New Roman','FontSize',16);

function [w,tw] = ricker(f,dt)
%RICKER: Ricker wavelet of central frequency f.
%
% [w,tw] = ricker(f,dt);
%
% IN f : central freq. in Hz (f <<1/(2dt) )
% dt: sampling interval in sec
%
% OUT w: the Ricker wavelet
% tw: axis
%
% Example
%
% [w,tw] = ricker(10,0.004);
```

```

%      plot(tw,w);
%
nw=2.2/f/dt;
nw=2*floor(nw/2)+1;
nc=floor(nw/2);
w = zeros(nw,1);

k=[1:1:nw]';

alpha = (nc-k+1).*f*dt*pi;
beta=alpha.^2;
w = (1.-beta.*2).*exp(-beta);

if nargout>1;
    tw = -(nc+1-[1:1:nw])*dt;
end

```

Marc Mayer  
Director of Intellectual Property

Keysight Technologies, Inc.  
Legal Department, MS Legal  
900 South Taft Avenue  
Loveland, CO 80537

970-679-2046 T  
www.keysight.com



July 2, 2015

Via E-Mail: [sohely@ualberta.ca](mailto:sohely@ualberta.ca)

Sohely Pervin

Re: Permission to Copy and Republish Figures

Dear Sohely,

This is in response to your email request of June 25, 2015 seeking consent to copy and republish figures in which Keysight owns the copyright. I have attached for clarity a copy of the email that sets out your request. I am pleased to advise that you have Keysight's permission to include the images in your thesis. Permission is granted to use this information as requested.

This consent is conditioned upon:

1. There being included with these extracts an appropriate acknowledgement and an appropriate copyright notice in a form similar to the following:

© Keysight Technologies, Inc.

Reproduced with Permission, Courtesy of Keysight Technologies

2. To the extent you revised any of the Keysight copyrighted figures, thereby creating derivative works, you grant Keysight Technologies, Inc. and its subsidiaries a royalty-free, perpetual, license to reproduce, distribute, publically display, and create derivative works from such derivative works.

By reproducing these materials, you and your publisher acknowledge and agree: (1) that the Keysight work(s) and the information contained therein are accepted "AS IS"; (2) that Keysight does not make any representations or warranties of any kind with respect to the materials and disclaims any responsibility for them as reproduced by you; (3) that Keysight reserves the right to review any use or display of these materials and to terminate this consent and require their immediate removal if altered, modified, or portrayed in any way that, in Keysight's opinion, is in poor taste or diminishes the reputation of Keysight or its products; (4) that Keysight will not be liable for any damages, whether special, incidental, consequential, direct, indirect or punitive, resulting from or in connection with the use, copying or disclosure of the above referenced documentation, and (5) to indemnify Keysight for all claims, actions, damages, and expenses (including attorneys' fees) incurred by Keysight as a result the Keysight work(s) being reproduced, modified, or distributed pursuant to this consent.

Marc Mayer  
Director of Intellectual Property

Keysight Technologies, Inc.  
Legal Department, MS Legal  
900 South Taft Avenue  
Loveland, CO 80537

970-679-2046 T  
www.keysight.com



Thank you for your interest in Keysight Technologies and its products and services.

Sincerely,

A handwritten signature in blue ink that reads "Marc Mayer".

Marc Mayer  
Director of Intellectual Property  
[marc\\_mayer@keysight.com](mailto:marc_mayer@keysight.com)

Enclosures

Keysight owned works from which figures are extracted:

1. <http://literature.cdn.keysight.com/litweb/pdf/5989-2589EN.pdf>
2. <http://literature.cdn.keysight.com/litweb/pdf/5988-0728EN.pdf>

Schedule of Figures

1. *RF IV.tif*
2. *vector volt rel.tif*
3. *Figure 2\_7\_debye.png*
4. *Figure 2\_8\_colecloe.png*
5. *Fig 2\_5.png*
6. *Fig electronic polarization.png*
7. *Fig atomic polarization.png*
8. *Fig relaxation.png*
9. *Fig capacitor dc.png*
10. *Fig capacitor ac.png*
11. *Figure 2.png*





Sohely Pervin &lt;sohely@ualberta.ca&gt;

---

**Seeking permission to use a map in my M.Sc. thesis**

5 messages

---

**Sohely Pervin** <sohely@ualberta.ca>  
To: info@northrim.ca

Wed, Aug 19, 2015 at 12:41 PM

Hi there,  
I am an MSc student in geophysics at the University of Alberta, Canada and doing research under the supervision of Professor Douglas R. Schmitt.

I want to use a map (Slide\_7 link below) from your website and seeking permission to use it.

<http://www.northrim.ca/sitelab/upload/downloads/understanding-sasks-potash-industry-from-geology-to-the-press-release-may-2011.pdf>

My defense date is on 3 September, so I need permission letter soon.

I am looking forward to hearing from you soon.

Thanking you

Sincerely  
Sohely

—  
Sohely Pervin  
Graduate Student  
Department of Physics  
University of Alberta, Canada

---

**Tabetha Stirrett, P.Geo.** <tstirrett@northrim.ca>  
To: Sohely Pervin <sohely@ualberta.ca>

Wed, Aug 19, 2015 at 1:37 PM

Hello Sohely,

Yes you can have permission. How about I send you a version of the map on its own and I can put our logo and a permission statement on the map itself. What size would you like to see? 8.5x11?

Tabetha Stirrett  
North Rim  
Sent from my iPhone  
[Quoted text hidden]

---

**Sohely Pervin** <sohely@ualberta.ca>  
To: "Tabetha Stirrett, P.Geo." <tstirrett@northrim.ca>

Wed, Aug 19, 2015 at 1:54 PM

Hi Tabetha,  
Thank you very much for your reply.  
It would be great to get the permission statement on the map with your company logo. The size you mentioned is OK.

Sincerely  
Sohely  
[Quoted text hidden]

**Tabetha Stirrett, P. Geo.** <tstirrett@northrim.ca>  
To: Sohely Pervin <sohely@ualberta.ca>

Wed, Aug 19, 2015 at 3:42 PM

Hello Sohely,

I have given you a slightly updated version of the map. We have included a legend for you.

May I ask what you are doing your thesis on? I suspect it may have to do with Potash in Alberta?

Regards,

**Tabetha Stirrett, P. Geo., CPG**

*Business Development Manager*

*North Rim*

**\*\*\*Please note we have moved\*\*\***

290a-2600 8<sup>th</sup> Street East, Saskatoon, SK S7H 0V7

**Direct:** (306) 649-1465 **Mobile:** (306) 716-4204

**From:** Sohely Pervin [mailto:sohely@ualberta.ca]  
**Sent:** Wednesday, August 19, 2015 1:54 PM  
**To:** Tabetha Stirrett, P. Geo.  
**Subject:** Re: Seeking permission to use a map in my M.Sc. thesis


[Quoted text hidden]

---

## 2 attachments



**Elk Point Basin.jpg**  
2310K

 **Elk Point Basin.pdf**  
562K